

Sheffield Hallam University

Dual modality tomography for the monitoring of constituent volumes in multi-component flows.

DANIELS, A. R.

Available from the Sheffield Hallam University Research Archive (SHURA) at:

<http://shura.shu.ac.uk/19533/>

A Sheffield Hallam University thesis

This thesis is protected by copyright which belongs to the author.

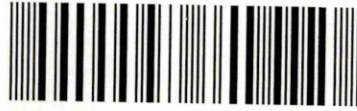
The content must not be changed in any way or sold commercially in any format or medium without the formal permission of the author.

When referring to this work, full bibliographic details including the author, title, awarding institution and date of the thesis must be given.

Please visit <http://shura.shu.ac.uk/19533/> and <http://shura.shu.ac.uk/information.html> for further details about copyright and re-use permissions.

SHEFFIELD HALLAM UNIVERSITY LIBRARY
CITY CAMPUS POND STREET
SHEFFIELD S1 1WB

101 522 927 1



Bm 367341

Sheffield Hallam University
REFERENCE ONLY

ProQuest Number: 10694414

All rights reserved

INFORMATION TO ALL USERS

The quality of this reproduction is dependent upon the quality of the copy submitted.

In the unlikely event that the author did not send a complete manuscript and there are missing pages, these will be noted. Also, if material had to be removed, a note will indicate the deletion.



ProQuest 10694414

Published by ProQuest LLC (2017). Copyright of the Dissertation is held by the Author.

All rights reserved.

This work is protected against unauthorized copying under Title 17, United States Code
Microform Edition © ProQuest LLC.

ProQuest LLC.
789 East Eisenhower Parkway
P.O. Box 1346
Ann Arbor, MI 48106 – 1346

**DUAL MODALITY TOMOGRAPHY FOR THE
MONITORING OF CONSTITUENT VOLUMES IN
MULTI-COMPONENT FLOWS**

A R DANIELS (B(Eng.) AMIEE)

*Thesis submitted to satisfy the
requirements of Sheffield Hallam University for the degree
of Doctor of Philosophy (PhD)*

School of Engineering Information Technology
Sheffield Hallam University
Pond Street
Sheffield
S1 1WB
February 1996

ACKNOWLEDGEMENTS

The concept for this project came from my supervisor Professor R G Green without whose immense knowledge, gentle encouragement and eternal patience little progress would have been possible. Many thanks also to my second supervisor Dr I Basarab for his support and patient reading of draft papers/thesis and to Dr F Dicken and his process tomography team at UMIST for their advice and help, especially in the construction of phantoms etc. I would also like to thank all the technicians in the department of EIT at Sheffield Hallam University for their assistance in constructing circuits and hardware etc.

I am also grateful to the other researchers with whom I had the pleasure of working: Neil, Marshall, Joe, Jas, Fu'ad, Ruzairi and Jan, whose support and friendship was invaluable throughout my three and a half years.

My biggest debt is to Valerie, my wife, for her patience and understanding during my time as a researcher and when writing my thesis.

ABSTRACT

This thesis describes an investigation into the use of dual modality tomography to monitor multi-component flows. The concept of combining two modalities for this purpose evolved from a desire by the Water Research Council to determine volume flow rates of the major components of sewage. No single sensing method is capable of detecting all suspended solids in sewage flows therefore a decision was taken to combine the technologies of electrical resistance and optical tomography to produce a single measurement system. Sensors for both were positioned around the periphery of a static, circular phantom to allow comparisons between dual and single modalities.

Modelling was carried out to determine the behaviour of the electrical impedance and optical tomography technologies in a three dimensional situation, where a variety of flow components exist. This provided a greater understanding of the problems involved in combining these technologies and an appreciation of the potential benefits.

The remainder of the work can be divided into three areas. Firstly, hardware was constructed to make voltage measurements for both modalities. Secondly, software was written to perform data acquisition, data manipulation and image reconstruction using a simple back projection algorithm developed for this purpose. Finally, an integration of the individual hardware and software components was performed to produce a dual modality system on which tests were carried out to determine the resulting benefits over single modality alternatives.

TABLE OF CONTENTS

CHAPTER 1

INTRODUCTION

1.1 SEWAGE FLOWS.....	1
1.1.1 The Changing Boundary	2
1.1.2 Safety as a Consideration.	3
1.1.3 The Environment Within a Sewer.....	4
1.1.4 Physical Properties of the Conveying Liquid.....	4
1.2 EXISTING FLOW MEASUREMENT APPROACHES	5
1.2.1 Commercial Flow Measurement Techniques	5
1.2.1.1 <i>VARIABLE AREA FLOW METER.....</i>	5
1.2.1.2 <i>TURBINE FLOW METER.....</i>	6
1.2.1.3 <i>DIFFERENTIAL PRESSURE FLOW METERS</i>	6
1.2.1.4 <i>VORTEX SHEDDING FLOW METER.....</i>	6
1.2.1.5 <i>ELECTROMAGNETIC FLOW METER</i>	7
1.2.1.6 <i>ULTRASONIC FLOW METER.....</i>	7
1.2.1.6 <i>CORIOLIS FORCE FLOW METER.....</i>	7
1.2.2 Tomographic Techniques Under Development	8
1.2.2.1 <i>ELECTRICAL IMPEDANCE TOMOGRAPHY</i>	8
1.2.2.2 <i>ELECTRICAL CAPACITANCE TOMOGRAPHY.....</i>	9
1.2.2.3 <i>ELECTRICAL CHARGE TOMOGRAPHY.....</i>	10
1.2.2.4 <i>ELECTROMAGNETIC TOMOGRAPHY.....</i>	10
1.2.2.5 <i>OPTICAL TOMOGRAPHY.....</i>	11
1.2.2.6 <i>ULTRASONIC ACOUSTIC TOMOGRAPHY.....</i>	11
1.2.2.7 <i>OTHER TOMOGRAPHIC METHODS.....</i>	12
1.3 THE DUAL MODALITY MEASUREMENT SYSTEM	12
1.4 AIMS OF THE PROJECT	14
1.5 ORGANISATION OF THE THESIS.....	15

CHAPTER 2

IMAGE RECONSTRUCTION AND SYSTEM SOFTWARE

2.1 FIVE ERT RECONSTRUCTION METHODOLOGIES	17
2.1.1 Back Projection Along Equipotential Lines	17
2.1.2 Iterative Back Projection Along Equipotential Lines	18
2.1.3 The Sensitivity Method	19
2.1.4 The Newton Raphson Algorithm.....	19

2.1.5 The Double Constraint Method	19
2.2 BACK PROJECTION OF ERT DATA	20
2.3 'BACK PROJECTION' OF OPTICAL DATA.....	25
2.4 DUAL MODALITY TOMOGRAPHY IMAGE RECONSTRUCTION.....	27
2.5 SOFTWARE.....	29
2.5.1 Electrical Resistance Tomography Software	29
2.5.2 Optical Tomography Software	32
2.5.3 Dual Modality Tomography Software	34

CHAPTER 3

ELECTRICAL RESISTANCE TOMOGRAPHY

3.1 METHODS OF MODELLING COMPLEX IMPEDANCE	35
3.1.1 Two Dimensional Modelling Using 'Teledeltos' Paper	36
3.1.2 Results of Teledeltos Modelling	38
3.1.3 Two Dimensional Modelling Using 'HSPICE'	41
3.1.4 Results of Two Dimensional HSPICE Modelling.....	43
3.1.5 Three Dimensional Modelling Using 'HSPICE'	45
3.1.6 Results of Three Dimensional HSPICE Modelling	46
3.1.7 Modelling Conclusions.....	47
3.2 HARDWARE	49
3.2.1 Electrode Construction	50
3.2.2 Oscillator	52
3.2.3 Constant Current Source.....	52
3.2.4 Multiplexer.....	54
3.2.5 High Impedance Buffer	56
3.2.6 Instrumentation Amplifier.....	57
3.2.7 R.M.S. To D.C. Converter.....	58
3.2.8 Analogue To Digital Converter.....	60
3.2.9 Computer Interface	62
3.3 RESULTS	62
3.3.1 Varying Background Conductivity.....	63
3.3.2 Three Dimensional Analysis.....	64
3.3.3 Image Reconstructions for Five Samples.....	66
3.3.4 Image Reconstructions for Multiple Substances	67
3.3.5 Conclusions from Measured Results.....	68
3.3.6 Discussion of Data Acquisition Speed.	70

CHAPTER 4**OPTICAL TOMOGRAPHY**

4.1 MODELLING OF OPTICAL DISCONTINUITIES	72
4.1.1 Attenuation of Light.....	73
4.1.2 Refraction and Reflection At a 'Bubble' Interface	74
4.1.3 Divergence Due To 'Bubble' Interfaces	77
4.1.4 Refraction Due To a Variable Liquid Depth.....	78
4.1.5 Modelling Conclusions.....	79
4.2 HARDWARE	80
4.2.1 Optical Transducers	81
4.2.2 Logic Decoding / Data Latches	85
4.2.3 LED Drivers	87
4.2.4 Analogue Switches	89
4.2.5 Signal Conditioning.....	91
4.2.6 Data Capture.....	92
4.2.7 Computer Interface	94
4.3 RESULTS	94
4.3.1 Determination of ' α ' for Air and Water	95
4.3.2 Air Bubbles in Water.....	97
4.3.3 Variable Depth Liquids in Pipes.....	99
4.3.4 Image Reconstructions for Five Samples.....	101
4.3.5 Image Reconstructions for Multiple Substances	102
4.3.6 Conclusions from Measured Results.....	103

CHAPTER 5**DUAL MODALITY TOMOGRAPHY**

5.1 DUAL MODALITY CONFIGURATION	106
5.2 DUAL MODALITY RESULTS	107
5.2.1 Dual Modality Image Combination Techniques	107
5.2.1.1 AVERAGING FUNCTIONS	108
5.2.1.2 CRITERIA BASED DECISION FUNCTION.....	109
5.2.1.3 LOGICAL COMBINATION FUNCTION.....	110
5.2.2 Image Reconstructions for Five Samples.....	111
5.2.3 Image Reconstructions of Multiple Substances	113
5.3 CONCLUSIONS.....	114

CHAPTER 6

CONCLUSIONS AND FUTURE WORK

6.1 CONCLUSIONS.....	116
6.1.1 Models for the Optical and Electrical Modalities (Aim '1').....	116
6.1.2 Hardware for the Optical and Electrical Resistance Modalities (Aim '2').....	117
6.1.3 Combination of Sensors for Both Modalities on the Same Section of Pipe (Aim '3')..	117
6.1.4 Windows Based Software for Image Reconstruction and Data Acquisition (Aim '4')..	117
6.1.5 The Comparison of Measured and Modelled Data (aim '5').....	117
6.1.5.1 <i>ELECTRICAL RESISTANCE TOMOGRAPHY</i>	118
6.1.5.2 <i>OPTICAL TOMOGRAPHY</i>	118
6.1.6 Image Combination Techniques to Produce Dual Modality Images (Aim '6').....	119
6.1.7 Determining the Advantages of a Dual Modality Approach (Aim '7').....	119
6.1.7.1 <i>ELECTRICAL RESISTANCE TOMOGRAPHY RESULTS</i>	119
6.1.7.2 <i>OPTICAL TOMOGRAPHY RESULTS</i>	120
6.1.7.3 <i>DUAL MODALITY RESULTS</i>	120
6.2 FUTURE WORK.....	121
6.2.1 Faster Data Acquisition.....	121
6.2.1.1 <i>IMPROVED DATA ACQUISITION TECHNOLOGY</i>	122
6.2.1.2 <i>DIRECT WAVE SAMPLING (ERT)</i>	122
6.2.1.3 <i>SWITCHED D.C. OPERATION (ERT)</i>	123
6.2.2 Electrical Resistance Tomography Sensors.....	125
6.2.2.1 <i>ELECTRODE LENGTH</i>	125
6.2.2.2 <i>COMPOUND ELECTRODES</i>	126
6.2.2.3 <i>MULTI-LAYER ELECTRODE CONFIGURATIONS</i>	126
6.2.2.4 <i>ALTERNATIVE ELECTRODE NUMBERS</i>	127
6.2.3 Optical Tomography Sensors.....	128
6.2.3.1 <i>INCREASED VIEWS AND PROJECTIONS</i>	128
6.2.3.2 <i>OTHER LIGHT SOURCES</i>	130
6.2.3.3 <i>ALTERNATIVE LIGHT FREQUENCIES</i>	131
6.2.4 Further Mathematical Modelling.....	131
6.2.4.1 <i>AN IMPROVED HSPICE MODEL</i>	131
6.2.4.2 <i>OPTICAL MODELLING SOFTWARE DEVELOPMENT</i>	132
6.2.5 Other Possibilities for Future Work.....	133
6.2.5.1 <i>TIMING BETWEEN MODALITIES</i>	133
6.2.5.2 <i>IMPROVED IMAGE RECONSTRUCTION AND ALTERNATIVES</i>	133
6.2.5.4 <i>FLOW MODELLING AND ENVIRONMENTAL MONITORING</i>	134
REFERENCES.....	136

CHAPTER 1

INTRODUCTION

This chapter introduces work carried out to investigate the use of tomographic imaging to monitor volume flows of individual sewage components. Current monitoring technology is introduced and the options chosen for final investigation are also presented. Finally, the aims of the project are described followed by a description of how the thesis is organised.

1.1 SEWAGE FLOWS

The problems associated with monitoring sewage flows are similar to those that arise when developing technology for other multi-component processes [44].

There are several reasons for monitoring sewage flows:

- (1) To obtain daily on-line quantitative measurements from sewers which can be used to verify mathematical modelling of this type of flow [45].
- (2) Mechanical screens are used to remove solids from sewage flows but present designs vary in efficiency (% of solid removed) from about 15% to 50% [47]. Because the development process for these processes is empirical, two tomographic systems, one upstream and the other downstream of a screen would provide a convenient method of monitoring effectiveness and as a result help optimise designs.
- (3) During periods of heavy rainfall many sewers are unable to handle the volume of sewage flowing. Weirs inside the sewers permit any excess to overflow and be diverted through storm drains into rivers or special settling tanks [2]. Quantifying these flows would be useful for environmental

monitoring of the rivers at storm outlets and help enforce new European pollution legislation.

The main components of sewage are: cellulose material (paper, sanitary towels, rags etc.); rubber/plastic (condoms, plastic associated with sanitary towels etc.); solids (faeces) and the conveying liquid (mainly water based). Each have different physical properties making detection difficult using a single measurement technique. There have been various investigations in the field of two component flows including Dugdale [16] who applied optical methods to the problem of liquid/air interactions and attempted to identify the types of flow that occur. Govier [22] introduces theory to explain the interaction between different phases for flows in pipes and Geraets [20] uses capacitance sensors to identify flow patterns for two phase flows. This type of approach attempts initially to explain the modes of flow caused by varying combinations of both phases and then design hardware capable of identifying these. The work presented here takes an alternative approach and investigates the feasibility of designing a system capable of identifying the presence of each major component of sewage and their volumes, rather than the physical behaviour of the flow. Much of the work presented in this thesis concentrates on the type of problems unique to the sewage application, although the technology developed could successfully be applied to any situation where multi-component flows exist. Typical problems associated with sewage flows are described in the following sections.

1.1.1 THE CHANGING BOUNDARY

A problem particular to horizontal flows of the type found in sewers is the changing boundary which results from the variation in flow depth, Fig.1.1. At

times of low flow levels Fig.1.1 (C) several sensors may not make contact with the conveying liquid. Consequently any measurement system must be capable of adapting to this, otherwise a significant amount of data will be lost. This is especially important for a design using impedance tomography (Section 1.2.2) where electrodes should be in contact with the conveying liquid.

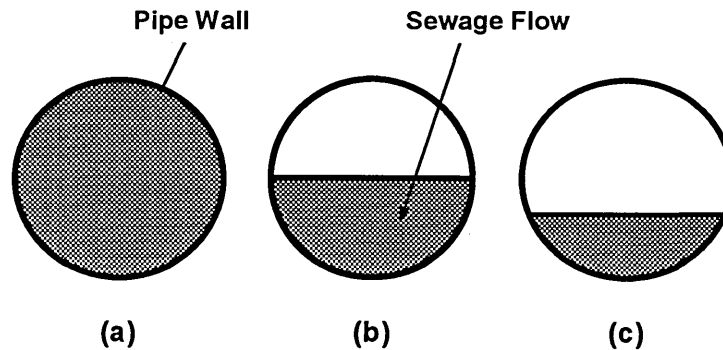


Fig.1.1 The Changing Boundary.

1.1.2 SAFETY AS A CONSIDERATION.

Equipment designed to work in a sewer must be intrinsically safe due to the presence of flammable gases, such as methane, in explosive concentrations. For many forms of tomographic imaging this is not a problem as it is possible to electrically isolate sensors. Careful consideration is required for designs using electrical impedance or resistance tomography (Section 1.2.2) in order to prevent the possibility of gaseous ignition resulting from the application of electric currents across the flow regime. Brant et. al. [12] discuss the issue of intrinsic safety with particular reference to explosive hazards in the oil and gas industry and describe methods of optimising circuit design. Intrinsic safety is an issue more correctly dealt with when a particular application has been decided and it will be left for future work to address this aspect more fully.

1.1.3 THE ENVIRONMENT WITHIN A SEWER

Another important consideration for designers of hardware that operates within a sewer is the internal environment. Sewers are extremely unclean areas resulting in the requirement that all sensors be non-intrusive to reduce the soiling of surfaces and degradation of measurement accuracy over time. Sensors that require regular cleaning will result in a system that is inefficient and costly to maintain. This is an issue that should be fully addressed during the production process, although it should be apparent at the design stage that a problem is not inherent when choosing a technique to monitor sewage flows.

1.1.4 PHYSICAL PROPERTIES OF THE CONVEYING LIQUID

The depth of the conveying liquid will affect the boundary conditions of a measurement system, although the physical properties of the liquid may alter due to a variety of reasons:

- a) **Mineral Seepage** - to or from surrounding strata may affect the electrical, optical and chemical properties as well as the relative density of the conveying liquid.
- b) **Temperature Variations** - occur due to seasonal changes in the discharge temperature of fluids entering the sewage affecting the electrical properties of the conveying liquid.
- c) **Influxes of Suspended Soil Material** - during heavy rain will affect the electrical, optical and chemical properties of the liquid.
- d) **Wide Variations in Discharge** - from industrial and domestic outflows will affect the depth, temperature, electrical, optical, and chemical characteristics of the liquid.

1.2 EXISTING FLOW MEASUREMENT APPROACHES

Many measurement techniques are available to monitor liquid flows and some for liquid/solid flows, but none exists that has been designed specifically for multi-phase applications where components have vastly different physical properties. 'Flow' measurement is a general term that can be defined as having three distinct definitions:

- (1) **Volumetric Flow** is the total volume that passes a measurement cross-section per unit of time.
- (2) **Mass Flow** is the total mass passing a measurement cross-section per unit time.
- (3) **Velocity of Flow** is the linear velocity past a measurement cross-section.

It is useful to define an additional category, that of **Constituent Flow**, as this is more appropriate for multi-component processes and measures either the Volumetric, Mass or Velocity flow of each distinct constituent within the flow. An overview of existing commercial flow measurement technologies and tomographic techniques currently under development is discussed below.

1.2.1 COMMERCIAL FLOW MEASUREMENT TECHNIQUES

Beck et. al. [6] define the concept of true mass flow measurement of a single phase and explain the difficulties of relating liquid mass flow-rate to a single direct on-line measurement. Single phase methods [37], [18] and [35] usually relate to liquid or gas flows and include the following technologies [37]:

1.2.1.1 Variable Area Flow Meter

One type of variable area meter introduces a restriction into a section of pipe which increases in diameter along the length of the pipe. An increase in fluid

velocity produces an increasing force on the restriction, causing it to move in the direction of the flow. The area around the restriction increases as it moves, due to the pipe's taper, reducing the pressure drop across it. As a result the restriction settles in a position where the opposite force applied to it (e.g. by a spring) exactly matches the force produced by the differential pressure. A typical design [3] inserts a magnet in the restriction and a Hall effect sensing device connected to a micro-controller interface is used to determine flow-rates.

1.2.1.2 Turbine Flow Meter

The turbine flow-meter utilises a 'propeller' situated in the flow and measures the flow rate by counting the number of revolutions induced per second, as the angular velocity is proportional to the rate of flow. Rotations are detected 'electronically' using a proximity detector within the pipe wall close to the propeller.

1.2.1.3 Differential Pressure Flow Meters

Known more commonly as 'orifice plate' or 'venturi' meters these introduce a restriction or gradual narrowing of the pipe into the flow causing a pressure drop. Pressure is measured either side of the restriction and the difference calculated. Flow rate is proportional to the square root of the measured differential pressure, but at low flows inaccuracy increases as low differential pressure values are difficult to measure.

1.2.1.4 Vortex Shedding Flow Meter

If a 'bluff' body is placed in a slow moving liquid it passes smoothly around the outside. As the fluid velocity increases the liquid separates alternately from the sides of the bluff body and swirls to form 'vortices'. Pressure sensors, such as

Piezo electric cells, can be used to measure these oscillations which are then used to determine the flow rate.

1.2.1.5 Electromagnetic Flow Meter

This type of flow-meter applies an electromagnetic field across the flow. When a conducting liquid passes through this field a small electric current is induced which can be detected by measuring the induced voltage between two electrodes. Flow rate is proportional to the measured voltage for a conveying liquid with **constant** electrical properties, which is an important consideration because if the electrical properties are subject to change this technology will not produce accurate results.

1.2.1.6 Ultrasonic Flow Meter

The ultrasonic flow meter has two standard categories, the 'Doppler effect' and the 'time of flight' meters. The Doppler effect flow-meter transmits ultrasonic pulses into the flow and measures levels of 'reflected' energy, which are then related to flow rate. Time of flight meters measure the time taken for an ultrasonic pulse to travel a set distance and then convert this a to flow rate. A major problem with the Doppler effect meter is that it relies on the presence of acoustic discontinuities within the flow otherwise little change in reflected energy levels occurs. The time of flight approach is more accurate but because only small changes in transit time occur these tend to be difficult to measure accurately.

1.2.1.6 Coriolis Force Flow Meter

The Coriolis meter utilises the forces exerted by liquids as they flow around bends in a vibrating pipe (Blickley [10]). As liquid approaches such a bend it

experiences an acceleration producing a force F_1 and as it leaves it experiences a deceleration resulting in an equal and opposite force F_2 . Because F_1 and F_2 occur at different positions the result is a twisting of the pipe, which can be measured and converted to a mass flow rate. This technique is accurate (1-2%) and can be implemented on dual phase flows such as liquid/solid and liquid/liquid (i.e. oil and water). In general it is expensive and only available for pipe diameters up to 100mm.

1.2.2 TOMOGRAPHIC TECHNIQUES UNDER DEVELOPMENT

There is currently a wide variety of tomographic techniques under development that are capable of measuring flow rates when used in conjunction with cross-correlation algorithms. Some techniques can also distinguish individual materials in multi-component flows by using mathematical image reconstruction algorithms. The main drawback of any tomographic technique is the cost of associated hardware and software.

1.2.2.1 Electrical Impedance Tomography

Electrical impedance tomography (EIT) produces a cross-sectional image of the impedance profile of a process. The origins of this technique can be traced to medical computed tomography, [28] and [4] where a lower cost and less harmful alternative to existing computed methods based on radiation was required. If a potential difference is induced between two electrodes on the external boundary of a conductive medium an electric field is produced within. Other electrodes positioned around the boundary measure the intensity of this field which is a function of the impedance profile of the enclosed medium. Sheffield University EIT hardware [4] uses 16 electrodes located around the outside of a patient's

body. A constant current is injected between two electrodes and the voltage potential induced is measured between all remaining adjacent electrode pairs. These measurements are repeated for a series of current injection positions and the resulting data are used to produce an impedance cross-section of the patient's body. This is achieved using a reconstruction algorithm to solve Laplace's field equations in two dimensions. This method has also been used to monitor industrial processes such as the concentration profile measurements made by Grootveld et. al. [24]. A distinction should be made between electrical impedance tomography (EIT) and electrical resistance tomography (ERT), EIT [42] uses both magnitude and phase components of the measured electrode waveforms, while ERT [46] uses only the magnitudes.

1.2.2.2 Electrical Capacitance Tomography

Electrical capacitance tomography (ECT) is based on the principle that as a substance moves through a measurement plane its specific permittivity alters the overall capacitance of the plane. Most capacitance systems use up to twelve measurement electrodes positioned around the outside of the measurement volume. Yang et. al. [53] present circuitry to measure low levels of capacitance with high accuracy (1%) requiring resolutions of 0.1 fF. A series of capacitance values can be determined by measuring between combinations of two electrodes. The resulting data are used by a reconstruction algorithm such as that used by Huang et. al. [26] to image two component process flows. Consequently, ECT is a viable technology but the resolution is limited due to the length of electrodes necessary to produce measurable capacitances. This produces the 'smearing' and 'averaging' effect associated with this technology.

1.2.2.3 Electrical Charge Tomography

Most of the work to date in this area of process monitoring has been carried out by Shackleton and Bidin et. al. [8, 9] using insulated electrodes fitted into the wall of a steel pipe. Dry particulates, passing these electrodes induce charge into them which is detected by either converting it to a voltage (charging a capacitor) or passing it to a charge amplifier. Currently, neural networks are used to identify the flow regime and velocity information is obtained by using two arrays of sensors at different positions along the pipe. This technique has the potential to monitor processes containing dry particulate flows and non-conducting liquids. However, it is not applicable to conducting liquids such as those found in sewage flows.

1.2.2.4 Electromagnetic Tomography

Electromagnetic tomography (EMT) is a new area of investigation instigated after a feasibility study carried out by Yu et. al. [56] with an experimental system using 21 sensors. The basis of this approach is to energise a measurement section using a sinusoidal magnetic field created using copper coils. The conductivity and permeability of a material within the measurement section produces a unique magnetic field, which is detected by separate measurement coils. Current work conducted by Yu et. al. [56] concerns the detection of electrically conductive and ferromagnetic material and it is not possible at this stage to determine the potential for detecting other substances. One consideration is the high cost of hardware required to generate high intensity magnetic fields capable of penetrating large objects.

1.2.2.5 Optical Tomography

Optical tomography is an established imaging technique used by Saeed et. al. [40] and Dugdale [16] for the identification of two component flows. As light travels through space it suffers attenuation for a variety of reasons, including scattering and absorption. Different materials cause varying levels of attenuation and it is this fact that forms the basis of optical tomography. If an optical emitter and detector pair, termed a 'view', are positioned either side of the measurement volume, information about its optical characteristics can be obtained. If the light is 'collimated' into thin 'pencils' and several views are grouped together to form a 'projection' then a larger area can be interrogated. If several different projections are used then it is possible to reconstruct an image of the materials optical attenuation cross-section.

1.2.2.6 Ultrasonic Acoustic Tomography

Ultrasonic tomography is an established medical imaging technique which has achieved a reputation as a useful method for the measurement of velocities in process flows. Xu et. al. [52] used ultrasonic tomography to measure bubble velocities in two phase flows. Transducers are excited using extremely short duration voltage pulses causing ultrasonic energy to propagate through the flow medium. This energy is attenuated by an amount dependent on the flow's physical composition. The detected signal is a train of amplitude modulated pulses which can be buffered, signal processed and low-pass filtered to produce an analogue voltage waveform. If two sets of detector/emitter pairs are used, at separate positions along the flow pipe, then cross-correlation [52] of the resulting data allows velocity information to be derived. The major drawback with this technique is that ultrasonic waves are difficult to collimate

and problems occur due to reflections within enclosed spaces, such as metal pipes etc. A Water Research Council report [48] concluded that the use of ultrasonic methods to detect solids within sewage flows was impractical due to the lack of contrast between the conveying liquid and some of the solid material, such as paper and rubber.

1.2.2.7 Other Tomographic Methods

A variety of other measurement techniques exists such as microwave tomography which utilises the varying attenuation characteristics of different materials at high frequencies. The main problem with microwave tomography is that of sensor design [11], as components have only recently emerged that allow spatial resolutions of less than 1cm at the detector. Microwave technology requires complex control circuitry but is capable of producing good discrimination between materials. Nuclear Magnetic Resonance (NMR) tomography is currently used as a medical imaging tool. NMR has been used by King et. al. [29] to monitor the flow of pneumatically conveyed coal but the major drawback for process applications is the development cost of the high power, high speed magnetic coils required to induce a uniform magnetic field through the whole of a measurement section.

1.3 THE DUAL MODALITY MEASUREMENT SYSTEM

After reviewing the various options it was decided that a dual modality system would provide the best approach for the detection of all the major components within sewage. Xie et. al. [51] used the dual modalities of electrodynamic and capacitance tomography to make mass flow calculations of gravity fed solids. Cross-correlation techniques were used in conjunction with one modality to

obtain velocity information while the second modality determined volume profiles. For the purposes of this work a cost effective approach was necessary and consequently the modalities of optical and electrical resistance tomography were chosen for investigation. Sensors for both are low cost and the design of associated circuitry can be made intrinsically safe. The electrical and optical characteristics of the major components of sewage are:

- a) **Cellulose Materials** tend to be absorbent and consequently assume the same electrical properties as the conveying liquid. They are usually optically opaque.
- b) **Rubber/Plastic** materials have a high electrical resistance and vary between opaque and clear in their optical properties.
- c) **Solids** generally have a resistivity higher than the conveying liquid and are opaque.
- d) The **Conveying liquid** can vary in respect of both optical and electrical properties but is mostly water in content.

Many fluids are opaque to visible light, but optical wavelengths are used to prove that the technique is viable. Wavelengths can then be modified to suite particular applications. An outline of the dual modality measurement system is shown in Fig.1.2 which illustrates sensors for both optical and ERT tomography mounted on a section of pipe. In reality both sets of transducers will have to be positioned close together to reduce the possibility of an image offset when the data sets are combined. All measurements were made using an 8cm (internal diameter) pipe, designed to fit directly into a flow rig. Optical hardware was designed using two 'projections' of 8 transducer pairs (views) allowing image

reconstruction to be applied to the acquired data. The ERT hardware was designed using 16 electrodes positioned equidistantly around the periphery of the pipe wall.

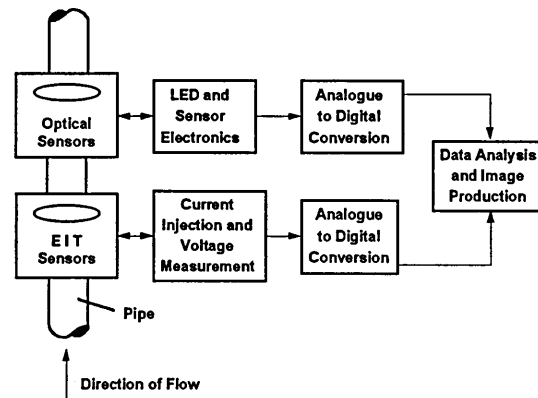


Fig.1.2 The proposed measurement system.

1.4 AIMS OF THE PROJECT

The main project aim was to design and investigate the benefits of a dual modality (optical and electrical resistance) tomography system for the measurement of constituent volumetric flows (Section 1.2) in sewers. The overall dual modality design was analysed and any possible improvements recorded, in terms of image 'quality' and the range of materials detected. Other research in this field tends to show that multi-component processes incorporating solids, liquids and possibly gases are unlikely to be imaged using a single modality due to the limited capabilities of any one process [16, 24, 26]. The original project objectives were:

1. Devise models for both the electrical resistance and optical tomography methodologies and where appropriate, investigate in two and three dimensions their potential performance in multi-component flows.

2. Design and build sixteen electrode, electrical resistance and two projection, eight view optical tomography hardware. Both systems must be compatible with the same computer input/output hardware to allow simple data combination.
3. Combine the sensor hardware for both modalities on a single section of pipe to allow dual modality data to be acquired.
4. Write 'Windows' based software to implement back projection algorithms for both the electrical resistance and optical tomography designs and use this to implement a dual modality imaging system.
5. Compare measured and modelled data for both modalities.
6. Make measurements and reconstruct images for a wide range of materials within a liquid conveyor, including bubbles, and draw conclusions about the benefits of dual modality tomography.

1.5 ORGANISATION OF THE THESIS

An outline of the contents of each thesis chapter is given below:

Chapter 1: A general introduction to the topic of tomography and its application to the monitoring of process flows is presented.

Chapter 2: Image reconstruction theory and methodology are presented and an algorithm capable of producing images for optical, electrical resistance and dual modality tomography is described. Also, Windows software designed to control the system hardware, carry out image reconstruction and produce a graphical display is described.

Chapter 3: A detailed description of the hardware designed, built and tested to implement electrical impedance tomography is given. Modelling carried out in two and three dimensions and test results carried out on a static phantom are also presented.

Chapter 4: Similar in content to chapter three but with reference to the optical hardware. Modelling carried out to determine the behaviour of certain aspects of optical theory is also presented.

Chapter 5: Describes how the hardware outlined in chapters three and four is combined to produce a dual modality system. Results are also presented for various image reconstructions.

Chapter 6: This chapter presents conclusions relating to previous chapters and makes suggestions for future work.

CHAPTER 2

IMAGE RECONSTRUCTION AND SYSTEM SOFTWARE

This chapter presents theory relating to the reconstruction of tomographic images and the system software written to achieve this. It can be divided into five sections: firstly, five major electrical resistance reconstruction algorithms are introduced; secondly, implementation of the back projection method used in this thesis is described; thirdly a method for the reconstruction of optical tomography data is presented; next, there is a description of how both techniques can be combined to produce dual modality tomograms and finally Windows software written to implement image reconstruction and hardware control is discussed.

2.1 FIVE ERT RECONSTRUCTION METHODOLOGIES

The purpose of an electrical resistance tomography reconstruction algorithm is to produce a graphical representation of the resistance cross-section bounded by the measurement electrodes. A major difficulty when designing algorithms for electrical resistance tomography lies in the behaviour of electric currents, which follow a path of least resistance. Consequently, the equipotentials within a measurement volume tend to form complex three dimensional shapes that are a function of the internal resistivity profile. This is in contrast to optical tomography where light beams, when fully collimated, follow an extremely predictable path unless absorbed or deflected by some object.

2.1.1 BACK PROJECTION ALONG EQUIPOTENTIAL LINES

This was proposed by Barber *et al* [4] and uses the principle that if lines of equipotential are traced between electrodes then any change in resistivity

within the measurement cross-section produces a corresponding voltage change at the originating electrodes. This is due to the Ohmic relationship between the measured voltages and the internal resistivity profile of the measurement section. Back Projection Along Equipotential Lines is limited by the assumption that the back projected equipotential lines remain a constant shape, when modelling in chapter 3 demonstrates that this is not the case. The result is that for large objects (relative to the measurement section) and for objects of high resistance (relative to the surrounding medium) image distortions occur. Barber and Browne [5] describe a fast, one step implementation of this method and a variation of this is used for image reconstructions throughout this thesis.

2.1.2 ITERATIVE BACK PROJECTION ALONG EQUIPOTENTIAL LINES

One step back projection reconstruction algorithms often produce large errors, due to the reasons outlined above, and because of this an iterative variation was developed. The 'forward' problem (that of finding boundary voltages due to resistivity changes within the measurement section) is solved using a two dimensional finite element approach. The 'backward' or inverse problem (that of re-calculating the resistivity profile of the measurement section) is then solved by a back projection which combines error values from the previous solution to the forward problem and the actual measured boundary voltages. After several iterations an improved image is produced, assuming that convergence occurs which may require a relatively accurate first 'guess' of the resistance profile.

2.1.3 THE SENSITIVITY METHOD

Geselowitz [21] proposed the sensitivity theorem used by Gadd *et al* [19] to reconstruct ERT images resulting from the adjacent electrode drive strategy. For every projection, using adjacent current injection, sensitivity coefficients for each pixel location are established which are then grouped together into sensitivity regions. Back projection of measurement data is performed using these coefficients as the basis for the image reconstruction, with the less sensitive measurement pairs being ignored. Therefore, this approach is a variation of the original Barber and Brown technique in that the sensitivity regions are similar in shape to those produced by back projection.

2.1.4 THE NEWTON RAPHSON ALGORITHM

This algorithm uses a regularised linear 'approximation' to improve the estimate of conductivity for the 'backward' solution iteratively. In contrast to one step methods this approach requires that the large matrix of potentials, and its inverse, be calculated repeatedly producing an inflated computational overhead. Computational speed can be improved by using parallel processors [13] and dedicated matrix algebra co-processors. Yorkey *et al* [54] stated that this method is guaranteed to converge to the optimal solution, although variations of the algorithm often require a relatively accurate initial 'guess' of the average resistivity.

2.1.5 THE DOUBLE CONSTRAINT METHOD

This was proposed by Wexler *et al* [50] in which the finite element mesh is constrained with known current source values and the current density is then

calculated for the computer model elements. The finite element mesh is then constrained with the measured voltages and current source value allowing the voltage gradient in each element to be calculated. Finally, the resistivity in each element can be determined. Wexler demonstrated an improved accuracy for the double constraint method over conventional iterative approaches but this has to be weighed against the added computation required.

2.2 BACK PROJECTION OF ERT DATA

Back projection along equipotential lines using a single step was implemented to produce the image reconstructions presented in this thesis. This approach was chosen because of its speed and ease of implementation, although Yorkey [55] showed it to be the least accurate of the five methods outlined above.

Absolute accuracy was less important than speed and simplicity of design for the purposes of this thesis because the reconstructed images are used as a method of comparing sets of results. Although the algorithm presented here is classified as 'back projection along equipotential lines' it also shares many similarities with other reconstruction techniques such as the sensitivity algorithm and may be more accurately described as a combination of the two. As an introduction, the theory underlying this type of approach is outlined below.

To produce accurate image reconstruction of an electrical resistance measurement section involves the solution of a three dimensional problem. To simplify the computational complexity that this entails most algorithms approximate to two dimensions. Using Maxwell's equations {1-4} as a starting

point, formulae may be derived [49] that provide quantitative information about the 'real' and 'imaginary' components of an electrical signal injected into a circular phantom (radius 'r') containing a homogeneous liquid.

$$\nabla \cdot D = \rho \quad \{1\}$$

$$\nabla \cdot B = 0 \quad \{2\}$$

$$\nabla \times H = J + \frac{\partial D}{\partial t} \quad \{3\}$$

$$\nabla \times E = -\frac{\partial B}{\partial t} \quad \{4\}$$

Where ρ = volume charge density; D = electric flux density; B = magnetic flux density; H = magnetic field density; E = electric field density; J = current density and t = time. Given that $J = \sigma E$ {3} can be re-written as:

$$\nabla \times H = (\sigma + j\xi\omega)E \quad \{5\}$$

Where σ = conductivity, ξ = permittivity and $\omega=2\pi f$ (f = frequency). If the values of σ and ξ for water are substituted in {5}, for a frequency of 8kHz (the operating frequency of the experimental system) then:

$$\nabla \cdot H = (1 + (j8.854 \times 10^{-12} \times 16\pi \times 10^3))E$$

$$\nabla \cdot H = (1 + j0.445 \times 10^{-6})E \quad \{6\}$$

The imaginary component of the electric field induced in an isotropic water based phantom {6} is approximately 2200000 times smaller than the real part of the signal at this frequency. If these measurements were resolved into voltages by a phase sensitive detector then it would be difficult to make measurements of the imaginary (phase) component due to background noise

levels. Therefore, it was decided to concentrate on the real (magnitude) component to produce electrical resistance (ERT) rather than electrical impedance (EIT) tomograms.

The region within a phantom of any size bounded by the measurement electrodes can be represented by Laplaces' equation {7}, which can be written using cylindrical polar co-ordinates {8} to describe a circular phantom in 3 dimensions.

$$\frac{\partial^2 V}{\partial x^2} + \frac{\partial^2 V}{\partial y^2} + \frac{\partial^2 V}{\partial z^2} = -K(X, Y, Z) = \nabla^2 V = 0 \quad \{7\}$$

$$\nabla^2 V = f(p, \theta, z) = \frac{1}{p} \frac{\delta}{\delta p} (p \delta V) + \frac{1}{p^2} \frac{(\delta^2 V)}{\delta \theta^2} + \frac{\delta^2 V}{\delta z^2} \quad \{8\}$$

Where p is the radial axis, z the axis of symmetry to the pipe and θ the angular component. Approximating to two dimensions by making z a constant simplifies {8} to {9}, where K is a constant. Similarly, if the problem is one that uses boundary potentials then p is also a constant, for a circular phantom, as all the electrodes are positioned at a constant radius.

$$\nabla^2 V = f(\theta) = K \frac{(\delta^2 V)}{\delta \theta^2} = 0 \quad (0 \leq \theta \leq 2\pi) \quad \{9\}$$

The solution to {9} will produce boundary potentials for a circular phantom which can be approximated by a finite set of data readings made at equidistant electrode locations around the periphery of the phantom. Consequently, for any two adjacent electrodes having potentials V_i and V_j the boundary voltage can be described as {10}.

$$V_i - V_j = K \frac{(\delta V_{ij})}{\delta \theta} \quad \{10\}$$

Gauss' equation for an enclosed region {11} states that the change in surface potential integrates to zero over a conservative path 's'.

$$\int_s E \cdot \delta S = 0 \quad \{11\}$$

For a finite set of adjacent electrode potentials V_i and V_j this equates to:

$$\sum_{i=0}^n (V_i - V_{(i-1)}) = 0 \quad \{12\}$$

Where n is the number of electrodes. Fig.2.1 shows a phantom having 8 electrodes and therefore 8 possible adjacent potentials, which when summed will equal zero (according to equation {12}).

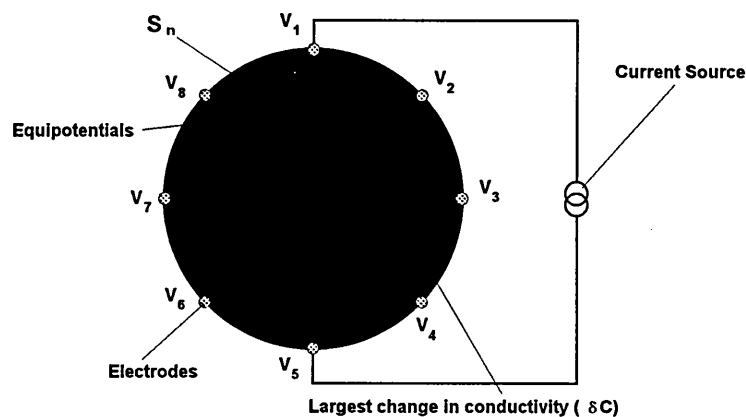


Fig.2.1 Sensitivity region map for an 8 electrode phantom

Fig.2.1 also shows the sensitivity regions (S_n) produced by the equipotentials originating from the measurement electrodes. Changes in the magnitude of the measured gradients ($V_n = V_i - V_j$) between these electrodes can be related to the corresponding sensitivity region. This is because an increase in the measured gradient V_n is assumed to be due (by a process of back projection)

to an increase in the conductivity within S_n . A calculation of relative conductivity within one sensitivity region (S_n) for a particular current injection position can be obtained by taking **two** voltage gradient measurements at the location associated with S_n , as described by equation {13}.

$$\delta C = \frac{V_b - V_a}{V_b + V_a} \quad \{13\}$$

Where V_a is for a homogenous phantom and V_b is for a phantom containing a resistive discontinuity. Fig.2.1 shows that the greatest conductivity change (δC) produces the largest voltage gradient change at location $V_4 - V_3$. Because Gauss' equation {11} equates to zero it is possible to superimpose the resulting 'summed' voltage gradients (from all the possible current injection positions) as the net effect will be zero. This action will also superimpose the sensitivity region maps to provide a 'picture' of the total relative conductivity change and accordingly the total relative **resistivity** change.

A practical application of this algorithm, for a 16 electrode phantom, produces 16 voltage gradients and therefore 16 sensitivity regions. If a 32x32 array is used to map these sensitivity regions (Fig.2.2) the voltage gradient values for each region can be stored in the corresponding array locations. For example, the value $V_4 - V_3$ is stored in the locations marked with an 'X' in Fig.2.2. Using this approach, a unique 32x32 array can be formed for each current injection position. If this is carried out for a homogenous and then a non-homogeneous phantom, equation {13} can be applied to produce a 'picture' of the relative conductivity change (δC) for each current injection position.

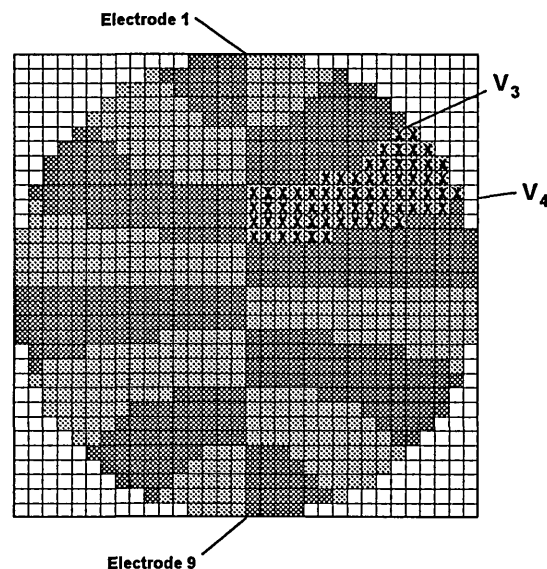


Fig.2.2 ERT sensitivity regions mapped onto a 32x32 array

These can then be superimposed to form a final 32 x 32 array representing a reconstruction of the change in conductivity over the measurement cross-section with a 32x32 pixel resolution. The disadvantage of this approach is that the final image is relative to the initial homogenous data set and therefore not an 'absolute' conductivity map. However, the algorithm is extremely fast and acceptable as a tool to compare data sets.

2.3 'BACK PROJECTION' OF OPTICAL DATA

If it assumed that pencils of 'collimated' light travel in straight lines and that the effect of reflection and refraction is ignored, then the major effect on a light beam is the optical attenuation as it passes through a medium:

$$I = I_0 \times e^{-\alpha_s d_s} \quad \{14\}$$

Where I is the light intensity after a distance d_s , I_0 is the initial light intensity and α_s is the attenuation constant of the medium through which the light is travelling. Therefore, for a constant distance across a circular phantom and a

constant light source intensity the received light intensity is a function of the average attenuation coefficient over the path. If a similar approach is used for light as is used for ERT back projection, then it is possible to say that for a particular optical emitter/sensor pair there exists a sensitivity region (S_n), Fig.2.3. It can also be stated that any change in the received light intensity is due to a change in the optical attenuation constant within the associated sensitivity region.

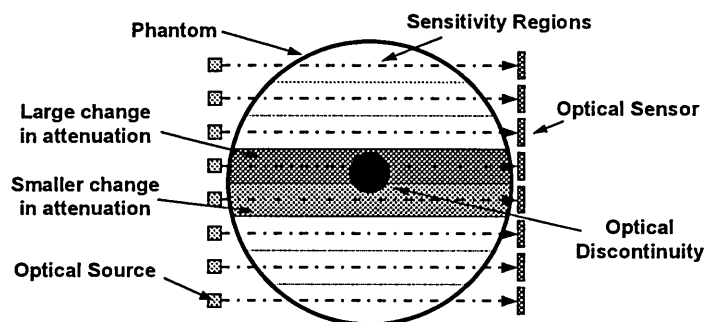


Fig.2.3 Sensitivity regions for an 8 view optical system

If two projections are used then it is possible to superimpose both sensitivity maps to form a 'picture' of the relative **change** in optical attenuation constant over the phantom cross-section (Fig.2.4). The major problem with using only 2 projections is the lack of information, producing aliasing and a resultant lack of image resolution.

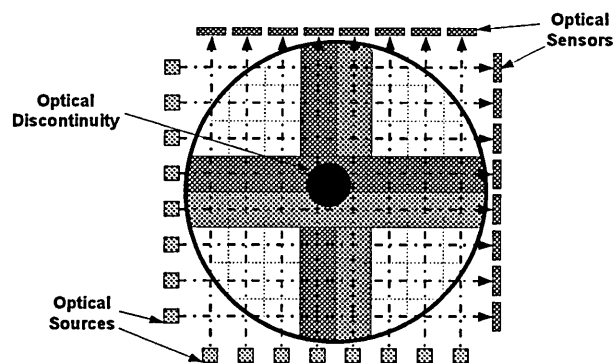


Fig.2.4 Two sensitivity maps overlaid

Consequently, if the change in optical intensity is measured for each view in a single projection the values can be stored in the appropriate positions within a 32x32 array (Fig.2.5). For example, the change in attenuation constant measured between emitter 'A' and sensor 'A' is stored in each of the locations marked with a cross in Fig.2.5. For two projections two 32x32 arrays are produced which can be superimposed to produce a final 32x32 array representing the change in optical attenuation constant across the measurement cross-section.

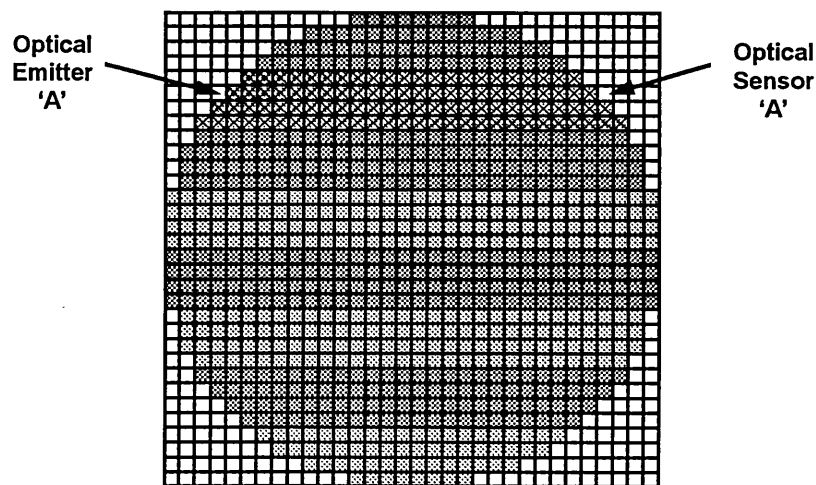


Fig.2.5 Optical Sensitivity regions mapped onto a 32x32 array

In reality, a resolution of 32x32 pixels is not required as only 8x8 emitter/detector pairs are used, but this approach was taken to allow compatibility with the ERT reconstruction.

2.4 DUAL MODALITY TOMOGRAPHY IMAGE RECONSTRUCTION

Image reconstruction of both ERT and optical data in this thesis is based on the back projection of measured data using sensitivity maps. Both techniques produce a 32 x 32 location image array with values representing changes in resistivity and optical attenuation constant. To produce a dual modality image

the data within these two arrays are converted to percentage values. 100% represents the largest resistivity change (for ERT) or the largest change in optical attenuation constant (for optical tomography), while 0% represents no change. The resulting percentage values for each modality can then be combined using an algorithm (section 1.2).

The requirement for, and idea behind a dual modality approach is illustrated in Fig.2.6 where simulated image reconstructions for three substances: opaque rubber; saturated paper and an air bubble are presented for the optical; electrical resistance and dual modality techniques. The electrical resistance tomogram (i_e) only shows rubber and air bubbles; the optical tomogram (i_o) shows rubber and saturated paper while the dual modality tomogram, by a process of 'data fusion' ($f\{i_o, i_e\}$), produces an image that identifies the position of all three materials.

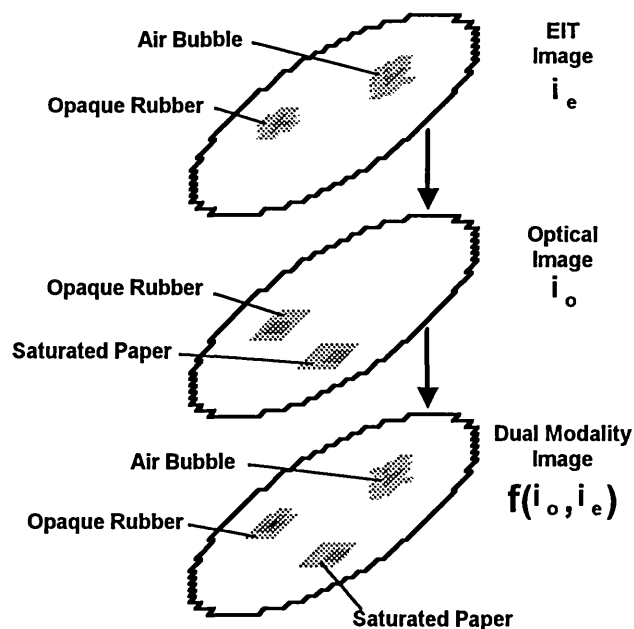


Fig.2.6 Production of the dual modality image

2.5 SOFTWARE

Sections 2.1 to 2.4 detail the theory behind the process of image reconstruction for both optical and electrical resistance tomography data. Image reconstruction is used in this thesis to compare data from these modalities with that of a dual modality system. Consequently, reconstruction software was written for both technologies separately and this code was combined to produce dual modality images. Three major pieces of software resulted for 'optical', 'electrical resistance' and 'dual modality' tomography, written using 'Windows' development tools within Visual C++. This section outlines the structure behind this software and explains how to interpret image reconstructions.

2.5.1 ELECTRICAL RESISTANCE TOMOGRAPHY SOFTWARE

Software developed for electrical resistance tomography performs basic tasks which includes: multiplexer control, application of a constant current to selected electrodes; control of the MAX180 data acquisition IC and image reconstruction. Fig.2.7 presents a flow diagram of the software which acquires a full set of data, as outlined earlier in this chapter, and also performs the following tasks:

1. Reconstruction of an image of the resistance contour bounded by the system electrodes.
2. Saving of the reconstructed image to disk in the form of a 32 x 32 array.
3. Printing of image reconstructions.
4. Copying of image reconstructions to the 'Windows' Clipboard, allowing pasting to other software packages.

5. Saving the acquired data to disk in the form of a 16x16 voltage array.

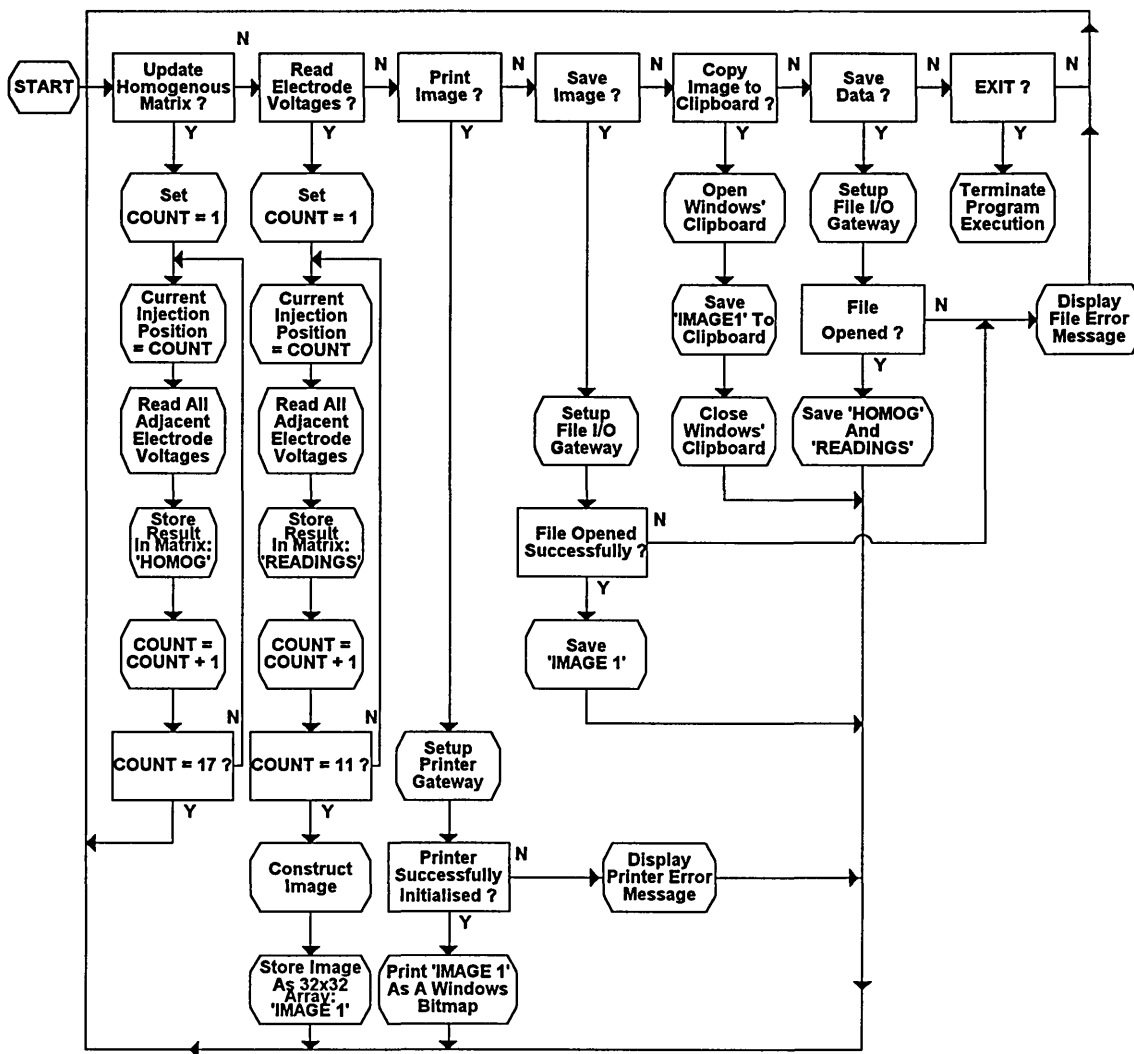


Fig.2.7 Flow diagram of ERT software

Descriptions of the 'Windows' operating system and programming terminology are found in the 'Windows user guide' [31] and 'Microsoft Visual C' programming manual [33]. The software developed provides a large amount of versatility, as it allows both data and reconstructed images to be saved to disk, in a format that can be imported directly into spreadsheets such as Microsoft Excel [32] and also the matrix manipulation software 'Mathcad'. Initially, data sets for a homogenous phantom are acquired and stored in a reference matrix

which may be updated at any time. Non-homogenous data sets are then acquired and subtracted from these homogenous readings before being processed by the image reconstruction software.

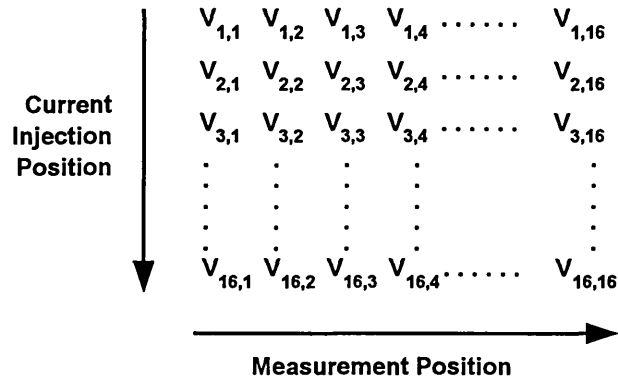


Fig.2.8 Format of 16 x 16 ERT array of measured potentials

Reconstructed images are stored in the form of 32x32 arrays, the principle of which is outlined in section 2.4. A 16 x 16 array is used to store acquired electrode voltages as shown in Fig.2.8. Consequently, $V_{2,4}$ represents the potential at measurement position 4 produced when current injection position 2 is used. Fig.2.9 shows this numbering convention which can be used to describe both adjacent current injection (Fig.2.9 (a)) and adjacent voltage measurement positions (Fig.2.9 (b)).

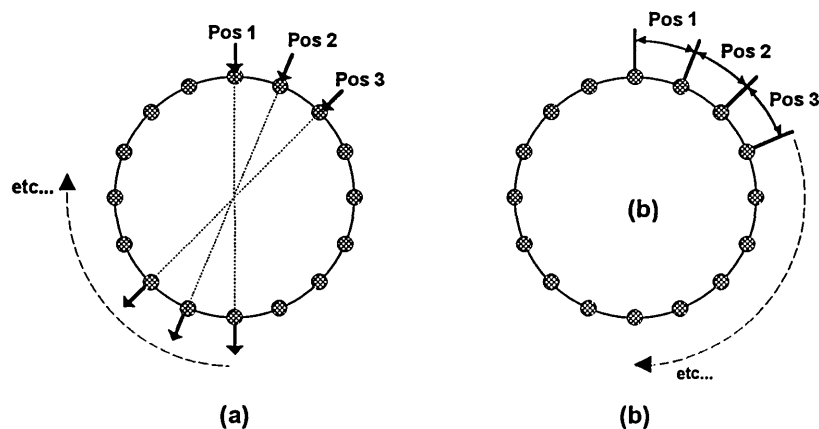


Fig.2.9 Opposite numbering convention (a) and adjacent numbering convention (b)

2.5.2 OPTICAL TOMOGRAPHY SOFTWARE

The core of the optical tomography software is identical to that presented in the previous section, for electrical resistance tomography. Fig.2.11 presents a flow diagram of the software illustrating this similarity. Consequently, a discussion of the differences between the two programs is presented here. The image reconstruction process discussed earlier in this chapter produces a 32 x 32 array in exactly the same way as the resistance tomography software except that the stored data sets represent changes in optical attenuation.

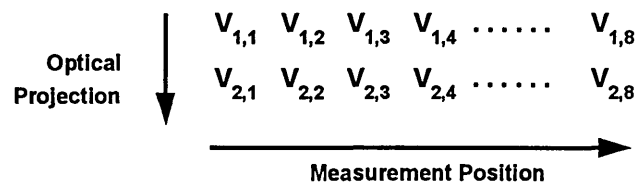


Fig.2.10 The 8 x 2 array used to store optical sensor voltages

The voltages produced by the 16 sensors (2 projections of 8 views) are stored in an 8 x 2 array prior to image reconstruction and the format of this is illustrated in Fig.2.10. There are 8 sensor voltages for both projections and therefore $V_{2,3}$ of Fig.2.10 represents the voltage obtained for view '3' of projection '2'.

Fig.2.12 illustrates the numbering convention, used by the optical software, for each of the projections/views. This can be superimposed over Fig.2.9 (b) to illustrate how both sets of readings relate to each other. Remaining details concerning the optical software (such as image/data saving, pasting and printing) are identical to the resistance software.

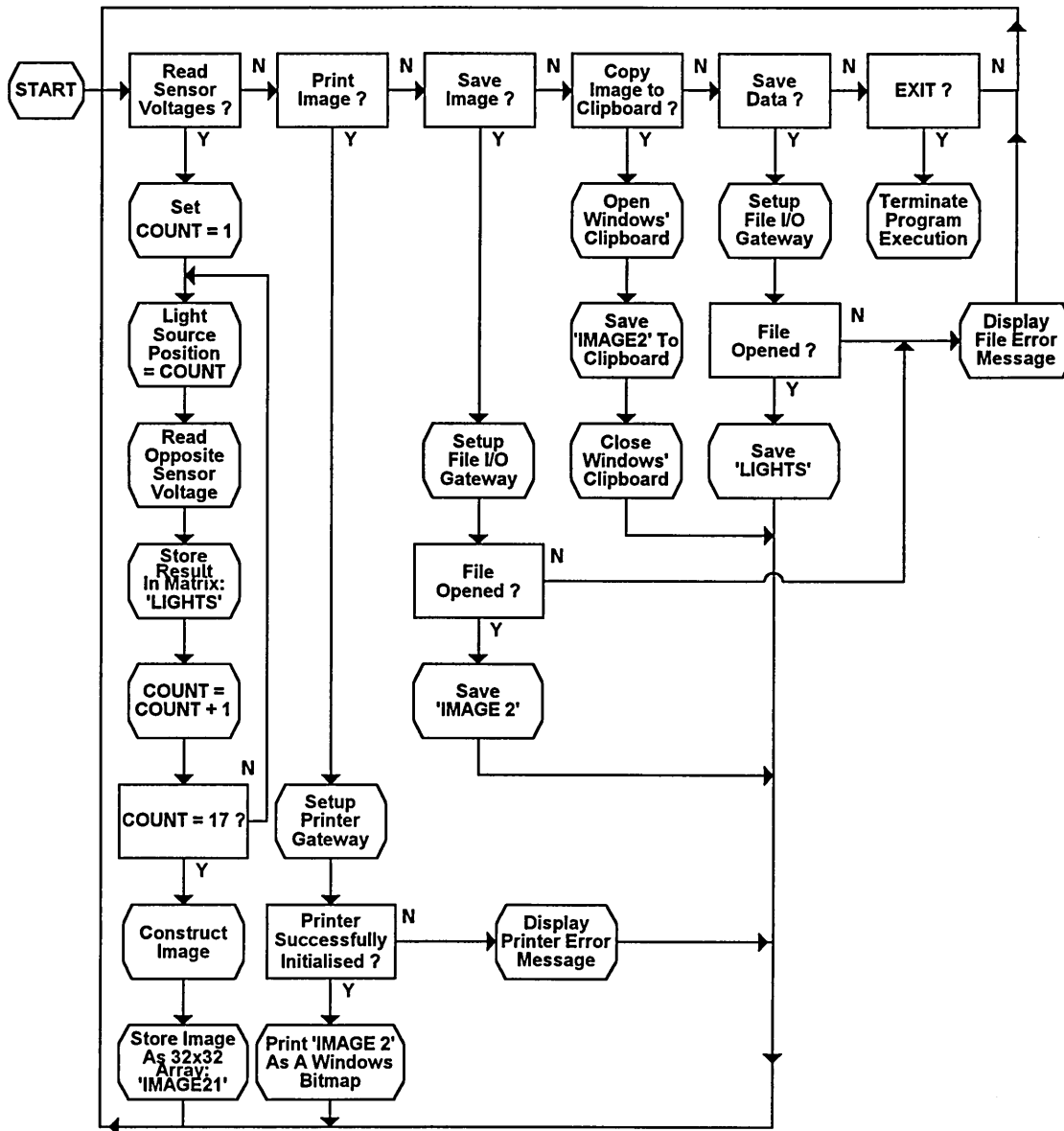


Fig.2.11 Flow diagram for the optical software

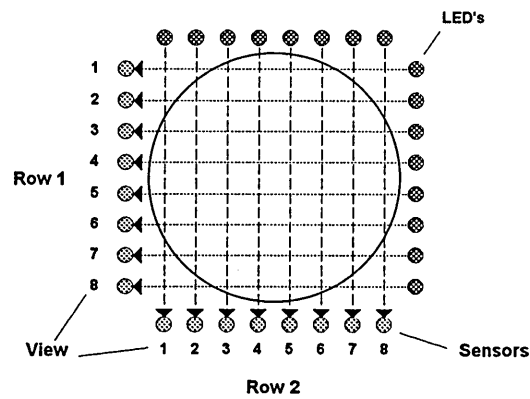


Fig.2.12 The sensor numbering convention used

2.5.3 DUAL MODALITY TOMOGRAPHY SOFTWARE

A third software package, which is a synthesis of code developed for both optical and resistance tomography, was developed for dual modality applications. Separate image reconstructions are performed for each individual modality, using the code described in sections 2.5.1 and 2.5.2. Fig.2.13 illustrates how the sensors for both modalities, and consequently their image reconstructions, overlap when viewed from above. This software package performs either of the image merging techniques described in section 2.4.

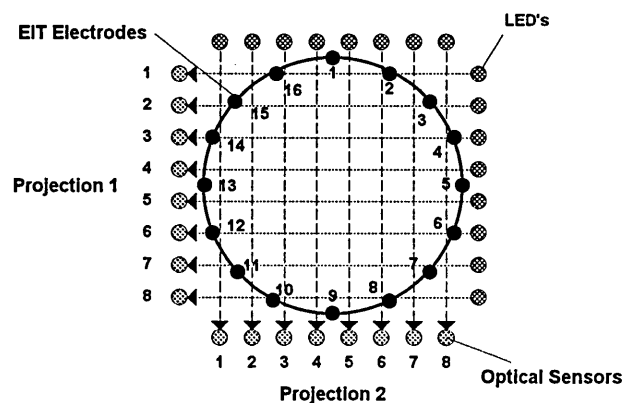


Fig.2.13 Mapping of the Sensors for Both Modalities in Space.

A detailed description of the data output, file and image formats can be found in sections 2.5.1 and 2.5.2. A full listing of the dual modality software (Fig.2.14) is included in Appendix 4 and a summary of its operation follows:

1. The user can update the homogenous matrix or acquire a full set of optical and resistance tomography readings.
2. A dual modality reconstruction is then produced by combining the individual resistance and optical image reconstructions (Chapter 2).
3. The reconstructed image data can be saved to disk as an array, in a format that can be imported into spreadsheets such as 'EXCEL'.
4. The reconstructed image data can also be printed within Windows.

- Both sets of acquired data, resistance and optical, can be saved to disk in a format that can be imported into 'EXCEL'.
- Previous data sets can be loaded from file and an image reconstructed.
- Graphs of the acquired optical and resistance data can be viewed separately.

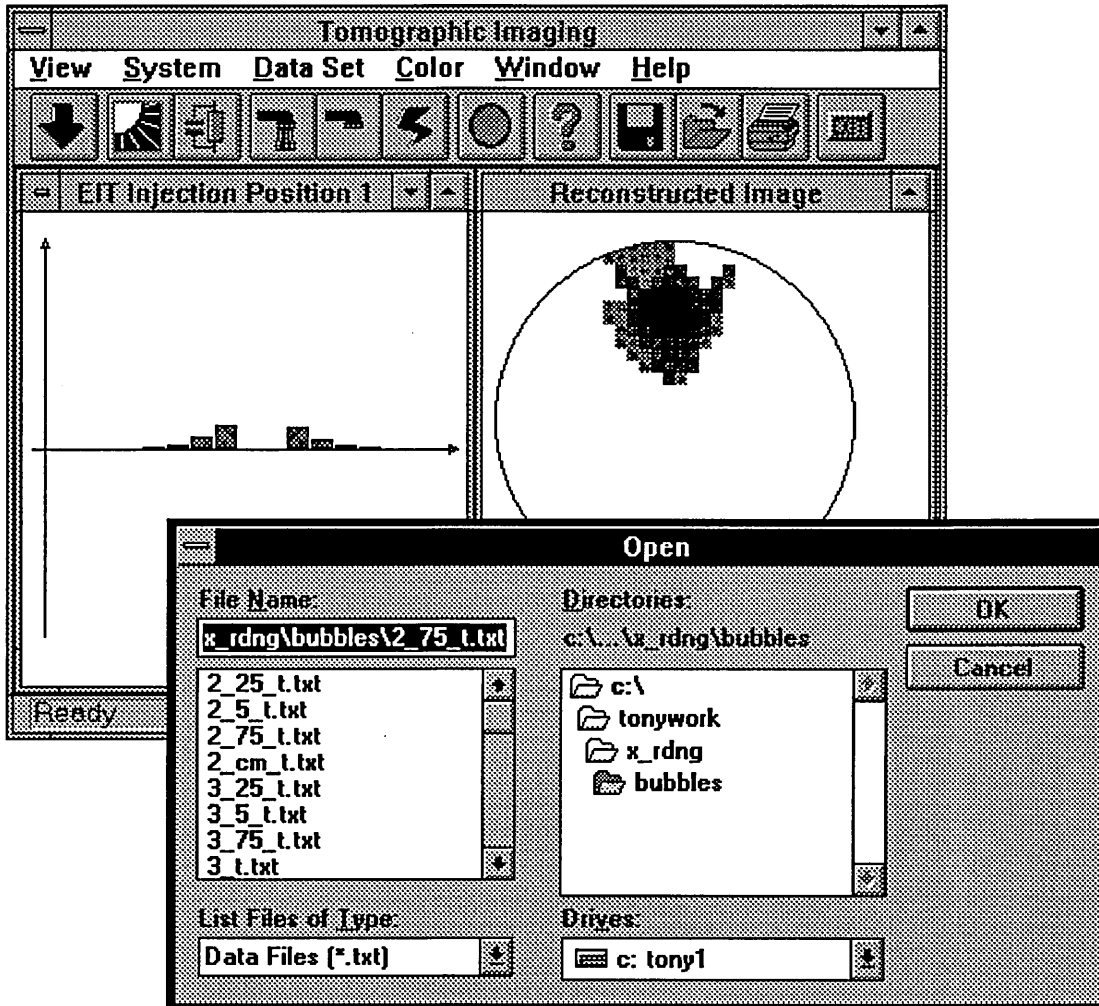


Fig.2.14 A typical screen shot of the dual modality software

CHAPTER 3

ELECTRICAL RESISTANCE TOMOGRAPHY

This chapter consists of four parts. Firstly, modelling carried out prior to evaluation of the hardware is described along with results for specific cases; secondly, the electrode and circuit designs are presented; thirdly, experimental results are presented that were designed to test the validity of the modelling carried out and finally there is an analysis and discussion of the results.

3.1 METHODS OF MODELLING COMPLEX IMPEDANCE

In this section three methods are presented that are used to model boundary voltage changes due to complex internal impedance variations in a 16 electrode phantom. Initially, resistive 'Teledeltos' paper was used to model a cross-section of the phantom but this has limitations because impedance changes can only be simulated by removing segments of the paper at appropriate locations. A second approach used created a two dimensional model using the circuit simulation package 'HSPICE', which was then developed to produce a three dimensional model.

3.1.1 TWO DIMENSIONAL MODELLING USING 'TELEDELTO'S' PAPER

Teledeltos paper can be used to physically 'plot' the equipotentials within any two dimensional shape. The concept of 'the flow of flux' assumes three dimensions and in the absence of sources or sinks of flux between the boundary surfaces it can be described by Laplaces' equation, {3.1}.

$$\frac{\partial^2 V}{\partial x^2} + \frac{\partial^2 V}{\partial y^2} + \frac{\partial^2 V}{\partial z^2} = 0 \quad \{3.1\}$$

Where V is the function of potential with X , Y , and Z : the conventional co-ordinate directions. When sources of flux are involved Poisson's equation can be used which, when combined with {3.1} produces equation {3.2}.

$$\frac{\partial^2 V}{\partial x^2} + \frac{\partial^2 V}{\partial y^2} + \frac{\partial^2 V}{\partial z^2} = -K(X, Y, Z) = \nabla^2 V \quad \{3.2\}$$

Where K is a function of X , Y , and Z in the sense that numerical values can be assigned to K at known points in the field. Under certain conditions there is no change in the field strength in one direction, e.g. the field within a long straight coaxial cable. Consequently, if the field in this direction is denoted by F_z then {3.3} applies allowing equation {3.1} to be reduced to {3.4}.

$$F_z = \frac{-\partial V}{\partial z} = C \text{ (a constant)} \quad \{3.3\}$$

$$\frac{\partial^2 V}{\partial z^2} = 0 \quad \text{and..}$$

$$\frac{\partial^2 V}{\partial x^2} + \frac{\partial^2 V}{\partial y^2} = 0 \quad \{3.4\}$$

The solution of equation {3.4} depends upon boundary conditions and is obtainable mathematically only in relatively simple cases e.g. the measured potential at the periphery of a homogeneous static phantom.

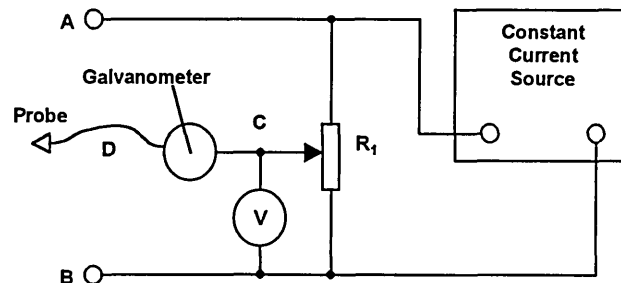


Fig.3.1 Circuitry used for field plotting

When the geometry of a problem becomes complex (an impedance discontinuity within a circular phantom) a mathematical solution is not easily resolved, making 'Teledeltos' paper a useful tool. Fig.3.1 illustrates the apparatus used for field plotting where A and B are attached to electrode locations on the 'Teledeltos' paper, between which a constant current is induced. The variable resistor R_1 controls the potential at one side of the Galvanometer (C) which reads zero when potential 'D' is equal to Potential 'C'. In this way it is possible to trace lines of electrical potential equal to that selected by R_1 , allowing the equipotential field pattern for any shape and electrode configuration to be drawn. This technique was used to simulate a three dimensional phantom by combining a series of two dimensional cross-sections in an attempt to reduce the overall modelling complexity.

3.1.2 RESULTS OF TELEDELTOSS MODELLING

It was decided to investigate field patterns for a two dimensional section through a circular electrode plane and consequently the conducting paper was cut to the correct shape and electrodes attached to simulate the adjacent method of current injection, Fig.3.2.

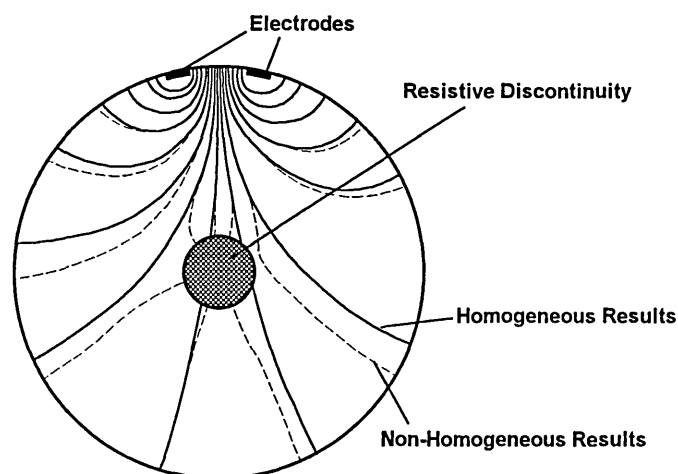


Fig.3.2 A Teledeltos simulation of the 'adjacent' method of current injection

Fig.3.2 illustrates two sets of results, one for a uniform homogeneous circle of Teledeltos paper and another produced after a circular hole was cut in the paper (non-homogeneous). A problem with this technique, other than the two dimensional limitation, is that it is difficult to alter the resistivity of the circular discontinuity. A hole cut into the Teledeltos paper represents an object with an infinite resistance, which in practice is unlikely to occur. However, this technique is of use when mapping equipotential lines for various electrode and current injection positions. The solid lines of Fig.3.2 represent equipotentials produced when a constant current source is connected to both electrodes for a homogenous phantom. The plot is repeated for the non-homogenous simulation and the results are also marked (by dotted lines in Fig.3.2). In a practical ERT design the changes in position of equipotentials illustrated in Fig.3.2 would be recorded as variations in measured electrode potentials.

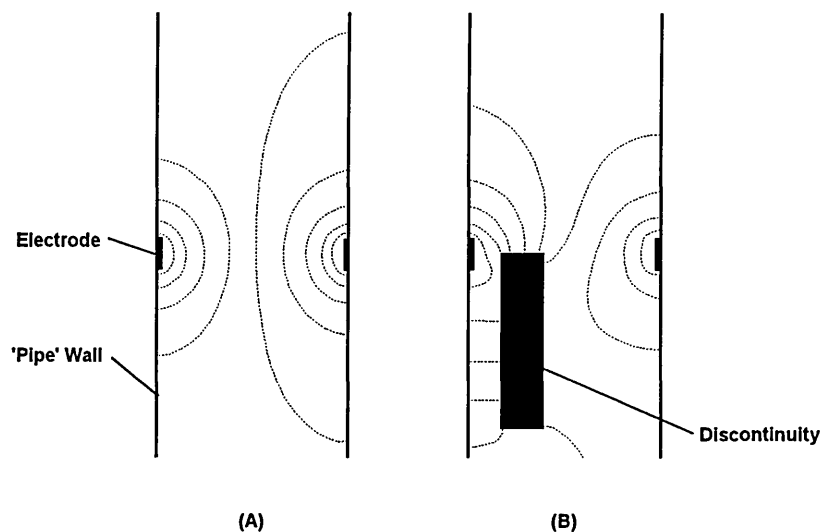


Fig.3.3 A Teledeltos simulation of the 'three dimensional' effect

Fig.3.3 (a) illustrates a vertical section through a homogenous phantom simulated using Teledeltos paper, where each of the dotted lines represent a 10% change in the measured potential. Fig.3.3 (b) repeats this approach for a

non-homogenous phantom using a rectangular hole to produce a resistive discontinuity. It can be noted from Fig.3.3 (a) and (b) that the equipotentials are affected significantly by the applied resistive discontinuity. By utilising this technique for several varying two dimensional views it is possible to approximate three dimensions and the next step is to compare results for an object moving through the phantom.

Fig.3.4 (a) represents a homogenous section and (b) - (e) represent the results obtained for a circular discontinuity moving a distance of 0.9cm per image towards the electrode plane. Fig.3.4 shows the point of contact between the phantom wall and the 10%, 20%, 30% and 40% equipotentials.

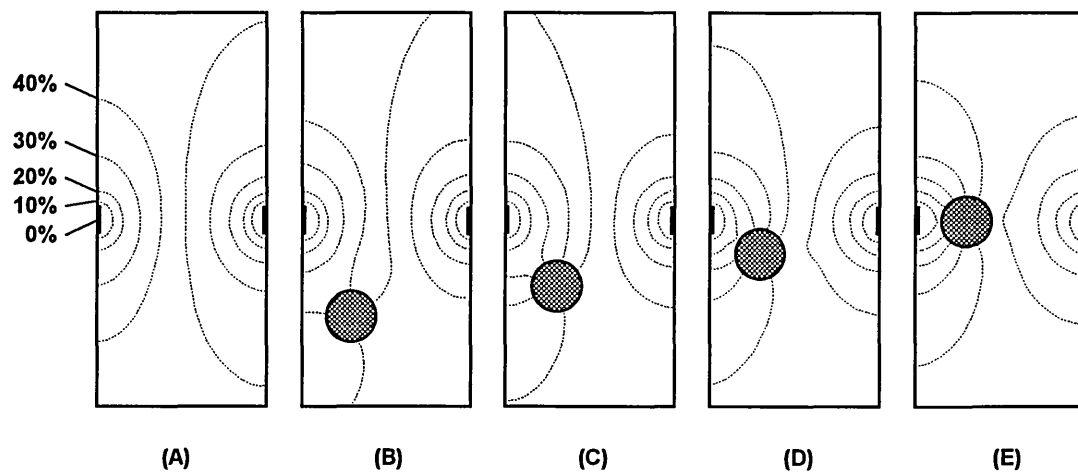


Fig.3.4 Teledeltos simulation of a moving object

The distances moved by these points of contact are measured for (a) - (e) and the results plotted in Fig.3.5. This graph illustrates large non-linear changes for the 30% and 40% equipotentials that are not linear. Significant alterations in the points of contact occur for resistance discontinuities outside of the electrode plane, Fig.3.4 (b) and (c). The Teledeltos plan and side elevations (Fig.3.2 and Fig.3.4) when viewed together suggest that objects outside the

measurement section do affect the measured electrode potentials. However, this approach confines the electric current to two dimensions making it more sensitive to smaller objects than a three dimensional evaluation.

Consequently, a three dimensional model was developed to investigate this further.

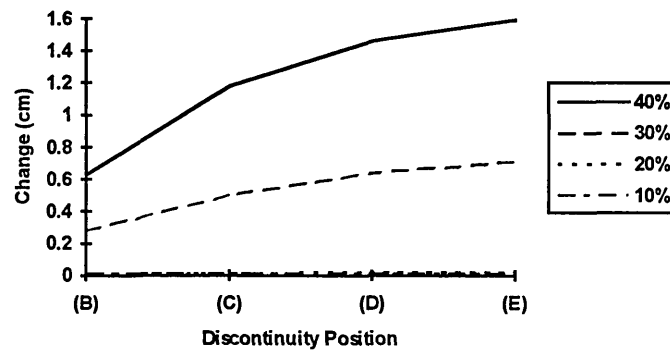


Fig.3.5 Change in equipotential positions with discontinuity movement.

3.1.3 TWO DIMENSIONAL MODELLING USING 'HSPICE'

Griffiths [23] introduced a method of constructing phantoms for electrical impedance tomography using a mesh of resistors soldered to pins on a matrix board. To simulate changing conductivities, resistors in the mesh are shunted at selected locations using other resistors and capacitors.

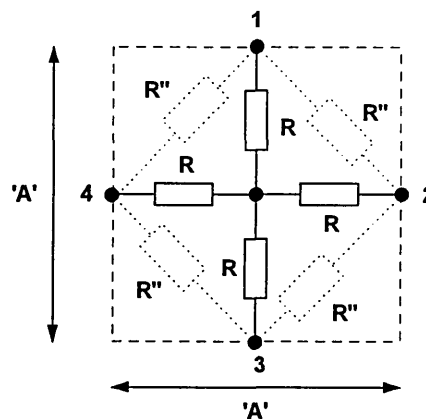


Fig.3.6 The resistive building block

Dines et. al. [15] also uses the resistor analogy to model cross-sections of core samples in an attempt to analyse the possible benefits of electrical resistance tomography for the incorporation into a dual modality imaging system.

Fig.3.6 illustrates a basic 'building block' that is used to implement Griffiths' technique (the actual resistance values R and R'' are determined by the physical distance they cover). The phantom used for this thesis is 8cm in diameter and therefore if 20 x 20 'building blocks' are used in the model (Fig.3.7) one block will be equivalent to a distance of 0.4cm ('A' marked on Fig.3.6). Consequently the resistor R will equate to a distance of 0.2cm and R'' to a distance of 0.282cm, allowing any resistivity (Ωcm) to be selected.

Griffiths [23] physically constructed the phantom to gain the electrode voltage readings while Dines et. al. [15] derived sets of network equations to achieve this. Other research groups including Curtis et. al. [14] have presented equations to calculate either the internal resistance given specific electrode voltages or electrode voltages given specific resistance values.

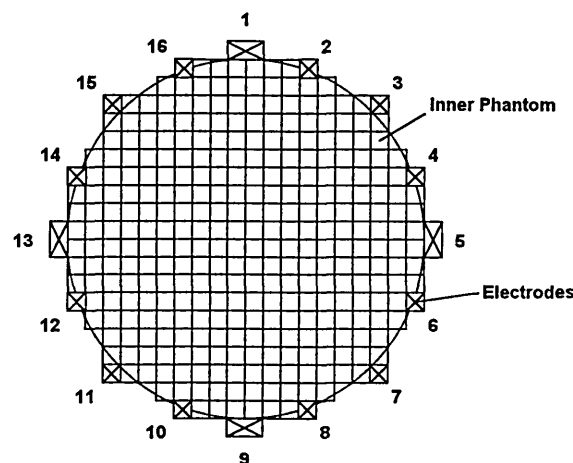


Fig.3.7 A circular cross-section using 'basic' building blocks

The circuit simulation package 'HSPICE' is an alternative to these approaches

which are based on the calculation of voltages at nodes which connect various types of linear components. Appendix 2 presents the HSPICE listing used to implement the configuration illustrated in Fig.3.7. Separate constant current sources, controlled by the HSPICE 'pulse' function, are used for each current injection position to produce 5mA output pulses at different points in time. In this way each current injection position is pulsed sequentially, during which time a full set of adjacent electrode voltages is calculated (Fig.3.8).

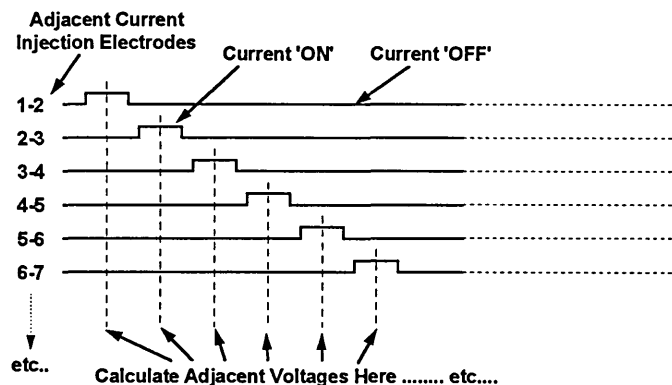


Fig.3.8 Timing diagram for HSPICE constant current sources

This technique is able to construct complex models of two dimensional resistivity profiles and has the potential to be a useful tool when testing image reconstruction algorithms.

3.1.4 RESULTS OF TWO DIMENSIONAL HSPICE MODELLING

The two dimensional HSPICE model uses copies of a single building block of resistors (Fig.3.6) duplicated 370 times and connected together to simulate a circular phantom (Fig.3.7). Results presented in this section are designed to test the performance of the model for various resistive discontinuity values.

The background resistance was set to 50 Ω cm and simulations carried out for

building block resistances of $500 \Omega\text{cm}$, $5000 \Omega\text{cm}$ and $50,000 \Omega\text{cm}$ in the position marked in Fig.3.9.

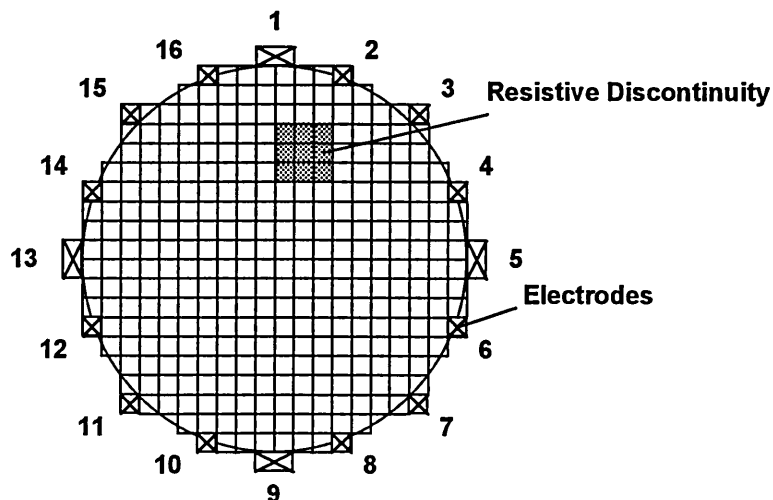


Fig.3.9 Position of resistive discontinuity (2D test)

Image reconstructions were generated from these simulated voltages using a simplified back-projection algorithm (Chapter 2). These are illustrated in Fig.3.10 and show a noticeable change in shape of the image reconstruction between 500 and $5000 \Omega\text{cm}$ but this is less obvious between 5000 and $50000 \Omega\text{cm}$.

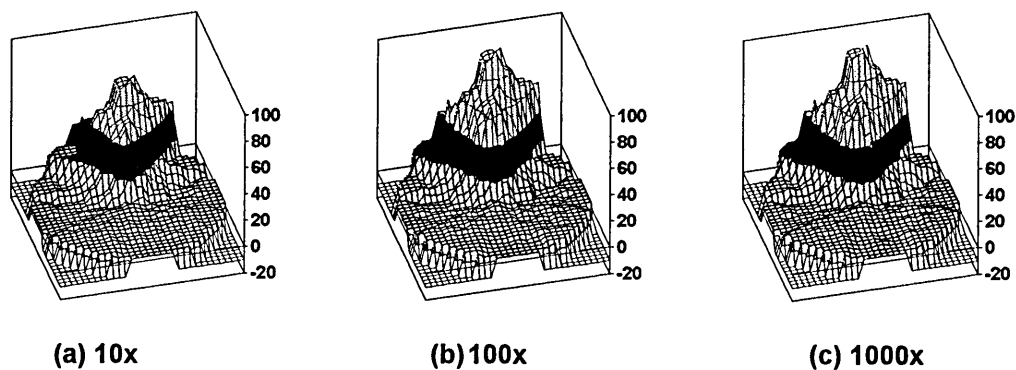


Fig.3.10 Increasing discontinuity resistivity

3.1.5 THREE DIMENSIONAL MODELLING USING 'HSPICE'

The three dimensional HSPICE model is an extension of the two dimensional model and allows complex impedance profiles to be simulated. The model is defined textually rather than using a graphical interface, which simplifies the construction of a large three dimensional resistor mesh. The three dimensional model is actually an interconnection of several two dimensional 'planes' separated by vertical connecting resistors whose values are a function of the distance between each plane. Initial experiments on large volumes required a large amount of processing time due to the excessive number of nodes required. Consequently the number of nodes in each plane was reduced to less than 100 from the original two dimensional design (Fig.3.11).

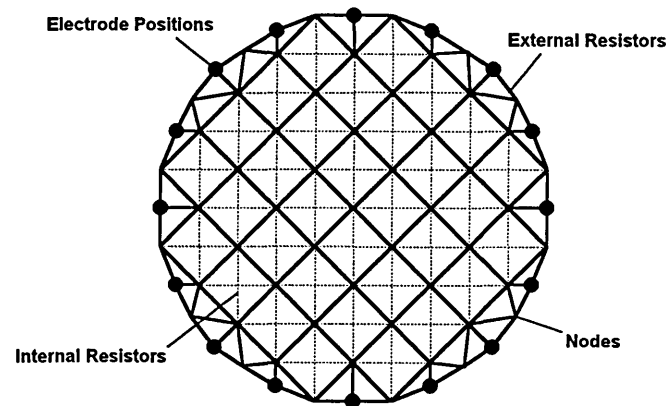


Fig.3.11 The resistor net used in 3 dimensional HSPICE modelling

Appendix 3 presents the HSPICE listing for a simulation using four layers (Fig.3.12). The constant current source and resistive building block descriptions are identical to those used in the two dimensional model. By a suitable choice of resistors in a localised area, it is possible to model three dimensional objects within the conducting liquid for a static phantom, and if multiple sets of results are combined it is possible to simulate flows.

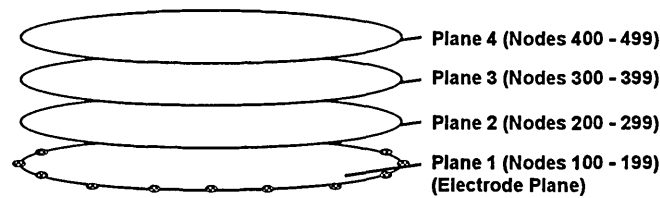


Fig.3.12 Node/Plane numbering convention

3.1.6 RESULTS OF THREE DIMENSIONAL HSPICE MODELLING

This section presents results for the three dimensional model when used to simulate objects moving through the electrode plane. Initially, plane 4 (Fig.3.12) with discontinuity '1' (Fig.3.13) is simulated with planes 3, 2 and 1 having a uniform distribution. Discontinuity '1' is then moved through planes 3 to 1 to gain information about how objects transported by a flow will affect the image reconstruction when they move towards the electrode plane.

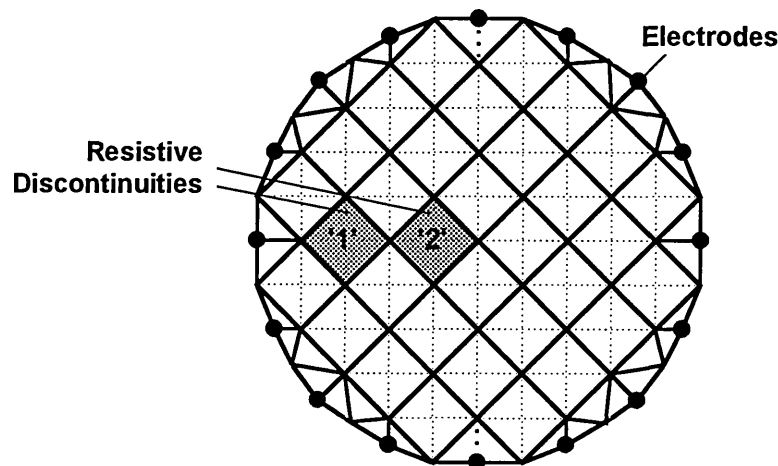


Fig.3.13 Position of resistive discontinuity (2D test)

Results are presented for discontinuities in position '1' (Fig.3.14) and position '2' (Fig.3.15) for each of the four planes, using a $50\Omega/\text{cm}$ background resistivity, a simulated phantom diameter of 8cm and a distance between planes of 1cm. For a phantom of this size the discontinuities equate to cylindrical shapes of 2cm diameter and 1cm in height.

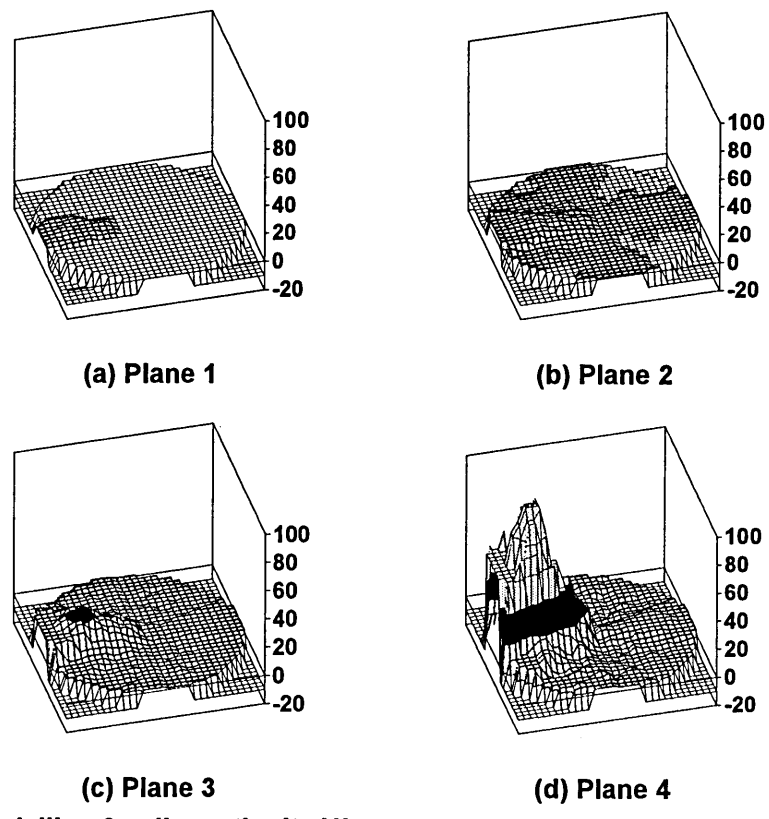


Fig.3.14 3D modelling for discontinuity '1'

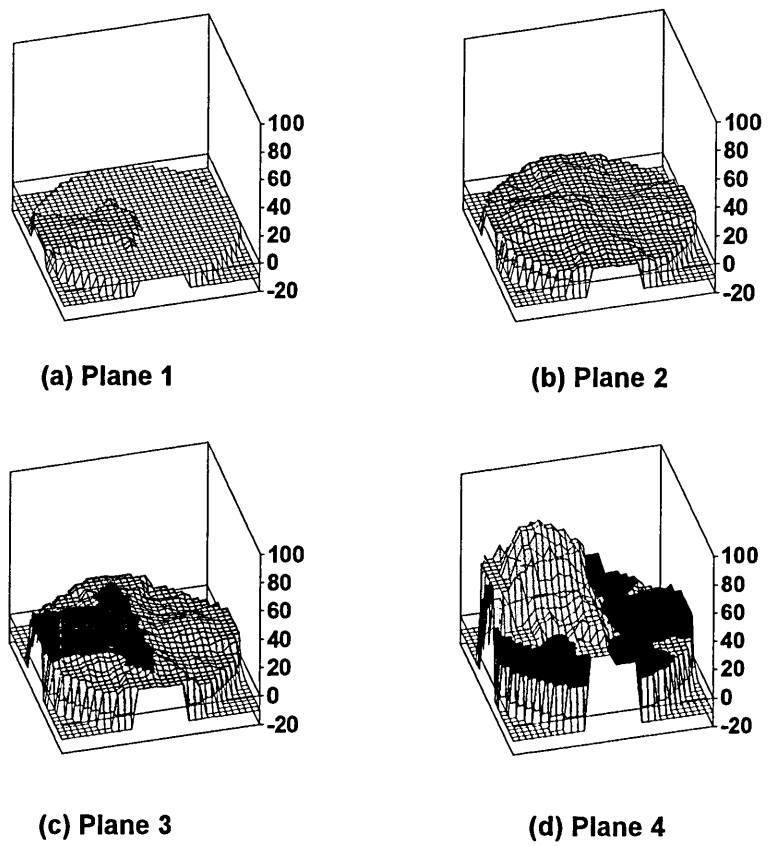


Fig.3.15 3D modelling for discontinuity '2'

Both sets of results (Fig.3.14 and Fig.3.15) show that discontinuities within the electrode plane (Plane '1') produce the greatest resistivity changes, but those within planes 2 and 3 are also significant.

3.1.7 MODELLING CONCLUSIONS

Results have been presented for electrical impedance tomography modelling in two and three dimensions using 'Teledeltos' and HSPICE techniques. Fig.3.4 illustrates how 'Teledeltos' paper was used to 'simulate' three dimensions using a combination of two dimensional cross-sections. From these results and the corresponding graphical tabulation in Fig.3.5 it can be seen that measurable distortions occur in the voltage profile around the phantom wall as an object moves towards the electrode plane. However, a more versatile modelling technique is required to quantify this in three dimensions and for this an HSPICE model was developed.

Fig.3.10 illustrates a set of image reconstructions gained from the two dimensional HSPICE model for a discontinuity of increasing resistivity. From this it may be seen that as the resistivity of the discontinuity increases there is a corresponding increase in image contrast. This is due mainly to the associated increase in potential gradient between adjacent electrodes and the resulting increase in signal to noise ratio. Fig.3.14 and Fig.3.15 illustrate image reconstructions using the three dimensional HSPICE model configured to simulate an object 'flowing' toward the electrode plane at two different radial positions. These results show that the object's radial position with respect to the phantoms' centre influences the data set and hence the image

reconstruction. This is due to the three dimensional flow of current flux in this type of environment. The closer the object is to the phantom wall, the more closely packed the current flux is around each electrode (i.e. the greater the current density). This hypothesis is tested in section 3.3, which introduces measured results.

3.2 HARDWARE

For test purposes, an 8cm diameter vertical section of pipe (the phantom), sealed at the bottom and having 16 stainless steel electrodes positioned around the periphery is used. Fig.3.16 illustrates the Electrical Resistance Tomography hardware constructed to inject an alternating current (of constant frequency and peak to peak amplitude) into the phantom via two selected electrodes and measure the voltage at each remaining adjacent pair.

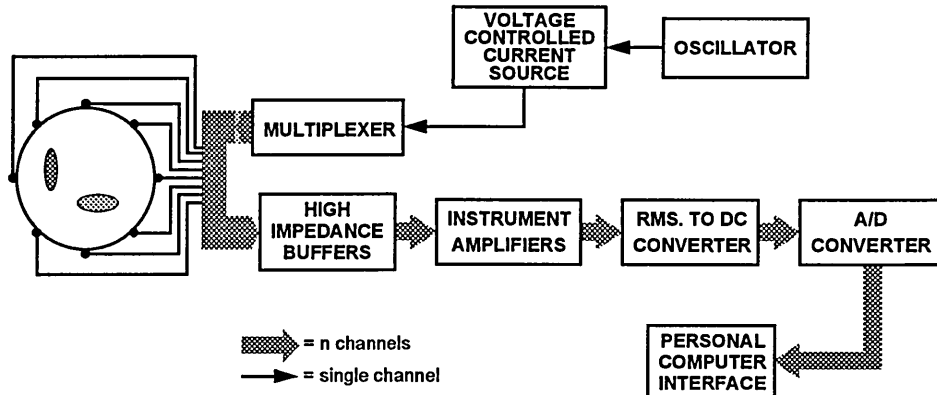


Fig.3.16 Schematic diagram of an Electrical Resistance Tomography system.

The magnitude of injected current is a function of the oscillator amplitude and an internal reference resistor. The oscillator provides a sine-wave of pre-set amplitude and frequency to the constant current source where any d.c. offset is removed to prevent electrolysis occurring. Selection of electrodes, between

which current is injected, is implemented by an analogue multiplexer arrangement under software control. The resultant voltages induced at the remaining electrodes are transferred to unity gain, high impedance buffers which subsequently connect to instrumentation amplifiers. The output of the instrumentation amplifiers is a difference wave-form which is converted to a d.c. signal by an r.m.s. to d.c. converter and finally passed to a personal computer interface by a 12 bit analogue to digital converter. Inputs to individual instrumentation amplifiers are from adjacent electrode sources and therefore the high impedance buffers prior to this must be able to cope with the large voltages that occur at current injection electrodes.

3.2.1 ELECTRODE CONSTRUCTION

The design chosen for this thesis uses 16 electrodes positioned halfway along the vertical height and equidistantly around the inside of a circular phantom (Fig.3.17). These provide electrical contact between the constant current source and the conveying liquid. All measurements presented in this thesis use a phantom filled with saline solution (of controlled conductivity) and consequently stainless steel was used as the electrode material to prevent corrosion. The phantom is of plastic tubing with an internal diameter of 8cm, a 5mm wall thickness and rectangular electrodes of size 16mm high x 8mm wide. Gold plated SMB connectors link the electrodes to coaxial cable which then joins to the current injection circuit board. Current injection electrodes are not used for voltage measurement [49], because a two electrode system is affected by the impedance between electrode and medium, and the impedance across

the electrodes (Fig.3.18). A four electrode configuration eliminates this problem.

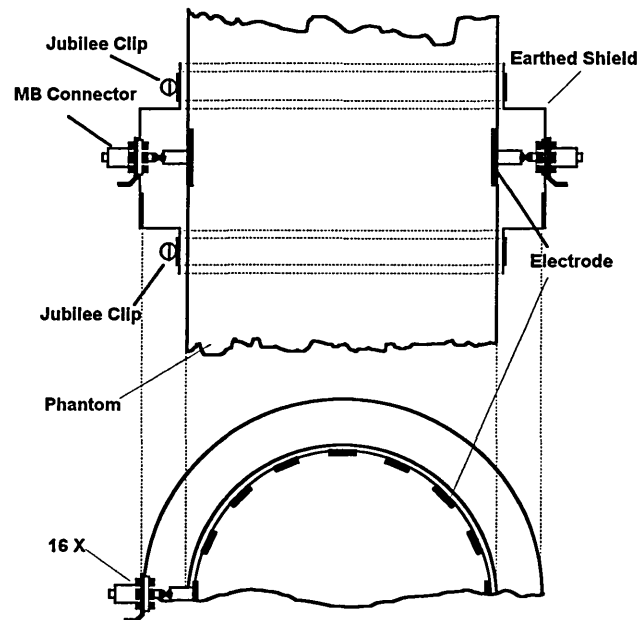


Fig.3.17 Electrode positioning within the 'phantom'

The major limitation of four electrode designs is that the total number of readings is reduced because any adjacent measurement pair containing a current injection electrode must be discounted. For the polar current injection approach this produces a loss of 4 data points per injection position and 64 for a full set of readings.

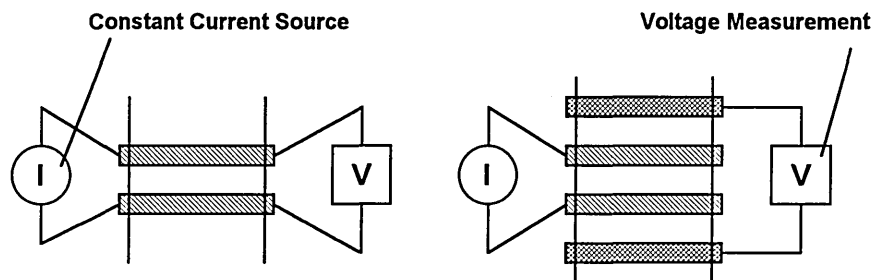


Fig.3.18 The two and four electrode methods

Hau et. al. [25] overcome this problem of a reduction in data points by using compound electrodes (Fig.3.19) which permit voltage to be measured and

current to be injected at the same electrode position, while retaining a four electrode configuration. This is achieved using a separate, smaller voltage measurement electrode which is bounded by the current injection electrode.

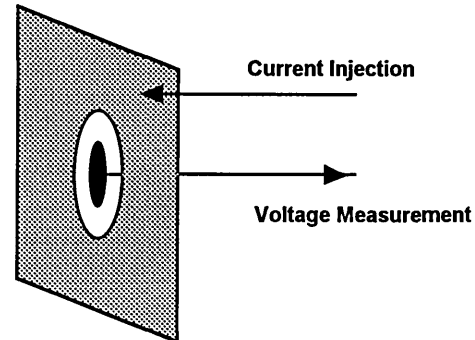


Fig.3.19 Compound electrodes

Using compound electrodes allows more voltage readings to be made in total, for the same number of electrodes, but also increases circuit complexity. For this reason compound electrodes are not used in the final design.

3.2.2 OSCILLATOR

In order to provide a low noise wave-form it was decided to use a HAMEG HM8030 function generator as this removed the necessity of designing and building such a complex device. The oscillator wave-form must be stable as its amplitude controls the magnitude of the injected current. The HAMEG HM8030 varies in amplitude by less than 0.05% at a frequency of 8kHz and a voltage setting of 5V (r.m.s.), allowing it to be used in 12 bit resolution systems.

3.2.3 CONSTANT CURRENT SOURCE

A design based on Nowicki [36] was chosen due to its reliable design and integrated capacitive compensation for the coaxial cable used to connect the phantom to the system hardware (Fig.3.20).

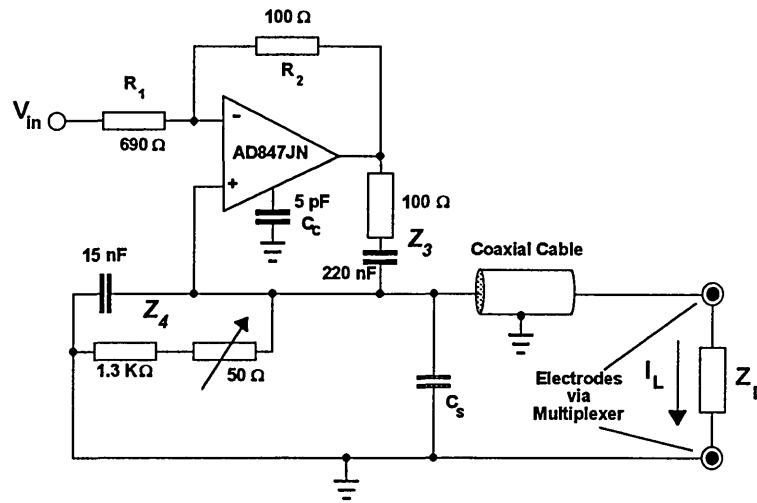


Fig.3.20 A single operational amplifier current source.

This design incorporates a d.c. blocking capacitor within Z_3 and is designed to provide 12 bit resolution for a load of between 39Ω and 1000Ω , with a maximum 10% reactive component. Capacitor C_s is the equivalent cable capacitance when its shield is grounded to earth and Z_4 eliminates effects of load voltage on the output current. Adjustment of the component values contained in this reactive combination reduces any phase or gain errors produced by the operational amplifier. Under ideal conditions the load current supplied by the circuit is given by the equation:

$$I_L = \frac{-V_{in} R_2 Z_4}{R_1 Z_3 Z_4 + Z_L (R_1 Z_3 - R_2 Z_4)}$$

When the condition $R_1 Z_3 = R_2 Z_4$ is met this simplifies to equation 3.5.

$$I_L = \frac{-V_{in}}{Z_4} \quad \{3.5\}$$

Z_4 can be simplified (Fig.3.21) when the equivalent capacitance of the coaxial cable (C_s) is also taken into account. Equation {3.6} gives the overall maximum

and minimum impedances of Z_4 due to changes in the value of R_V . For the selected oscillator frequency of 8kHz and with C_S assumed to be 100pF (a 1m length of cable), the resultant minimum and maximum values for Z_4 are shown in equations {3.6a} and {3.6b}. An 8kHz oscillator frequency was chosen due to bandwidth limitations of the r.m.s./d.c. converter design (Section 3.2.6). To produce a constant current of 5mA an input voltage of 6V (r.m.s.) is required.

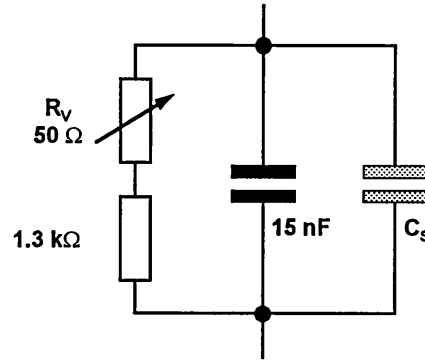


Fig.3.21 Equivalent circuit diagram for Z_4 .

$$\frac{1}{Z_4} = j\omega(15.1nF) + \frac{1}{1300\Omega} \quad (\text{Minimum}) \quad \{3.6a\}$$

$$\frac{1}{Z_4} = j\omega(15.1nF) + \frac{1}{1350\Omega} \quad (\text{Maximum}) \quad \{3.6b\}$$

3.2.4 MULTIPLEXER

Voltage measurement utilises a parallel approach with circuitry repeated for each of the 16 electrode positions to facilitate faster data acquisition by reducing the amount of time required for the signal conditioning circuitry to settle. However, this approach is not applied to the current injection circuitry as this would only remove the multiplexer switching delays, which are less than 1 μ s per operation. The hardware designed allows only two electrodes to be

selected for current injection via a single, multiplexed voltage controlled current source and two DG526, 16 way analogue switches (Fig.3.22).

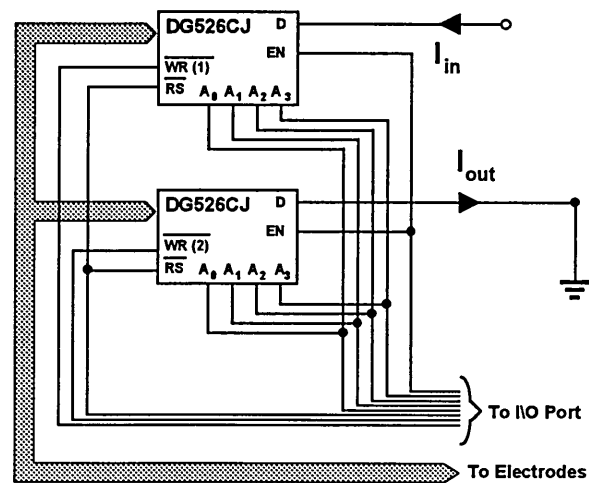


Fig.3.22 Multiplexing of the constant current source.

One analogue switch input is connected to the constant current source and the other to zero volts. Both devices are address decoded using two separate TTL control lines of the 40 way digital I/O port (Section 3.2.8), with all other connections identical.

A ₃	A ₂	A ₁	A ₀	Channel
0	0	0	0	1
0	0	0	1	2
0	0	1	0	3
0	0	1	1	4
0	1	0	0	5
0	1	0	1	6
0	1	1	0	7
0	1	1	1	8
1	0	0	0	9
1	0	0	1	10
1	0	1	0	11
1	0	1	1	12
1	1	0	0	13
1	1	0	1	14
1	1	1	0	15
1	1	1	1	16

Table.1 Address decoding for the DG526

To connect an electrode to the current source both EN and \overline{RS} are set to logic HIGH, and $\overline{WR}(1)$ is set to LOW. Then, the correct digital value (Table.1) is applied to the four address lines ($A_0 - A_3$) and after \overline{WR} is pulsed HIGH, the correct electrode is connected. The same principle is applied to the electrode connected to earth, but this time $\overline{WR}(2)$ is used. Both multiplexers can be reset to provide a high impedance connection to all 16 electrodes by pulsing \overline{RS} LOW.

3.2.5 HIGH IMPEDANCE BUFFER

The design of the buffer (Fig.3.23) provides a high input impedance, over a wide range of frequencies and incorporates d.c. blocking to prevent saturation of the high gain instrumentation amplifier that follows. Included in the design is a unity gain amplifier to drive the coaxial-cable shield at the same potential as V_{out} , thus reducing the capacitive loading that would occur if the shield were connected directly to earth [34].

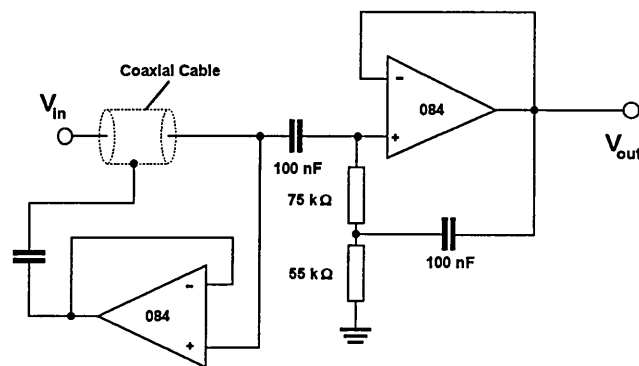


Fig.3.23 High input impedance voltage buffer.

A minimal design for the high impedance buffer is desirable to reduce the amount of noise that would be induced by the use of excessive component numbers. The input impedance, when tested over the range 1Hz-100kHz, has

a peak between 1kHz and 10kHz (Fig.3.24) making it suitable for use at the selected oscillator frequency of 8kHz. A high impedance buffer is desirable at this point in order to reduce the loading effect on each of the measurement electrodes and sixteen are required, one connected to each electrode.

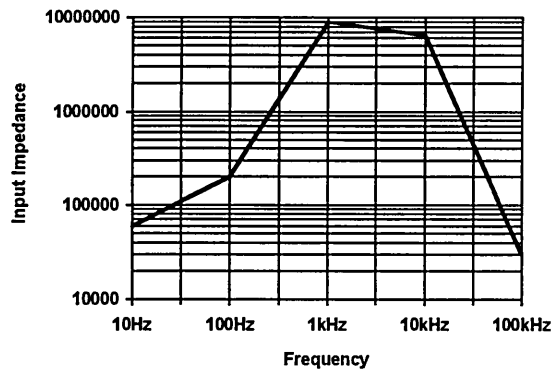


Fig.3.24 Input Impedance versus frequency for the voltage buffer.

3.2.6 INSTRUMENTATION AMPLIFIER

The buffered voltages from each electrode (1 - 16) are connected in adjacent pairs (1-2, 2-3, 3-4, ...) to the dual inputs of stable, high accuracy instrumentation amplifiers (Fig.3.25).

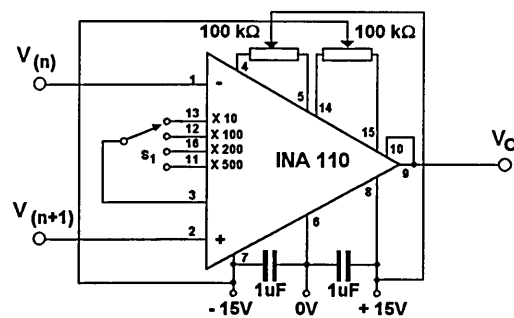


Fig.3.25 Connection details of the INA110 instrumentation amplifier

An output equal to the differential voltage between each electrode pair is provided by the circuit in Fig.3.25, which is the format required by the image reconstruction algorithm used (Chapter 2). The INA110 instrumentation

amplifier is a monolithic FET input device having a settling time of $4\mu\text{s}$ (to an accuracy of 0.01%) and several gain options (1, 10, 100, 200, 500) which are set by internal laser trimmed resistors. For an 8cm diameter phantom, an injection current of 5mA and a 20mS saline solution the maximum electrode difference voltage produced is 10mV. If a gain of 500 is selected for each instrumentation amplifier a maximum output voltage of 5V results, for measurement positions other than those used for current injection.

3.2.7 R.M.S. TO D.C. CONVERTER

The amplified a.c. difference signal is converted to an equivalent r.m.s. voltage via an AD736 r.m.s. to d.c. converter device. This is a low cost, true r.m.s. device which can be connected in an averaging mode to provide fast operation, as illustrated in Fig.3.26. In true r.m.s. mode an averaging capacitor is connected between C_{AV} and the negative supply rail, producing conversion times that are a function of the input voltage magnitude.

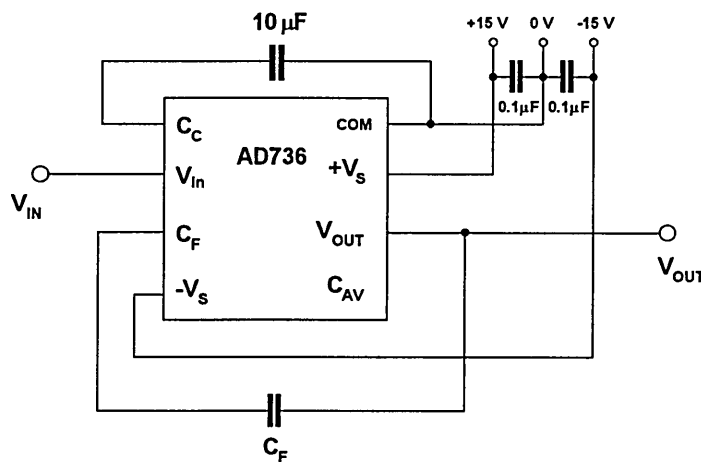


Fig.3.26 Connection details of the AD736 r.m.s. to d.c. converter (Averaging mode)

The faster averaging mode results in settling times that are determined solely by the RC time constant of C_F and an internal $8k\Omega$ resistor. Fig.3.27 illustrates

this dependency on C_F , which also provides low-pass filtering of the output voltage. Consequently, to achieve a settling time of approximately 3ms a value for C_F of $0.2\mu\text{F}$ is used, which yields a total time of 48ms when summed over all 16 current injection positions .

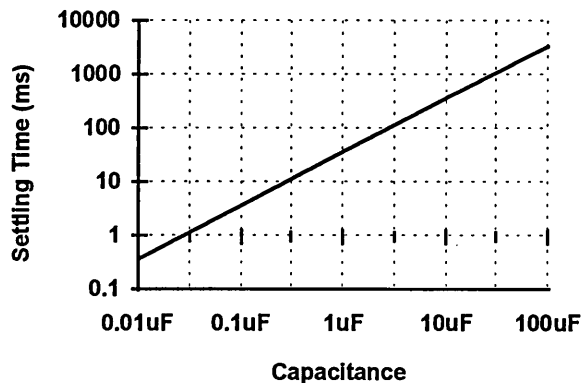


Fig.3.27 Settling time versus C_F for the averaging mode

Another important design aspect is the frequency response of the AD736, as this will affect design considerations for the other system components. Fig.3.28 shows the measured frequency response when the averaging mode is used and clearly identifies the reduction in gain at frequencies above 10kHz, which is compatible with a sinusoidal oscillator frequency of 8kHz.

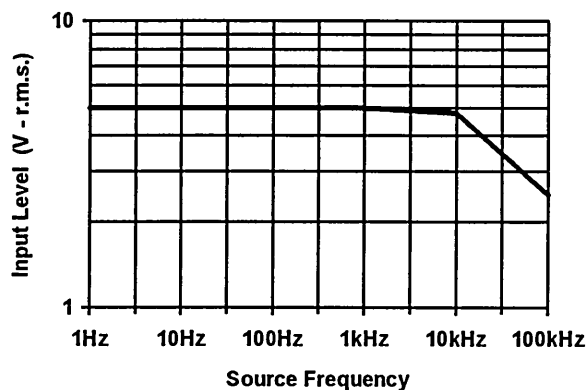


Fig.3.28 Frequency response of the AD736 r.m.s./d.c. converter

Output voltages from each AD736 contain both a.c. and d.c. error components which although relatively small may affect the reconstruction algorithm.

Compensation for both of these error components can be provided by including a correction factor in the system software, although for the purposes of this thesis they are ignored.

3.2.8 ANALOGUE TO DIGITAL CONVERTER

The d.c. signal produced by the AD736 is converted into a digital format allowing it to be transferred, via an interface, to the system software running on a computer. This interface is a MAX180 [30] 12-bit, 8 channel data acquisition device is used that incorporates internal track and hold circuitry, a low drift zener reference and flexible microprocessor interfacing (Fig.3.29). The time required by the internal track and hold circuitry to acquire an input signal is a function of the input capacitance and can be calculated using equation {3.7}.

$$t_{ACQ} = 10 \times (R_S + R_{IN}) \times 20 pF \quad \{3.7\}$$

Where R_{IN} is the output resistance of the previous stage and R_S is $1k\Omega$.

Therefore the acquisition time is a function of the output resistance of the previous r.m.s./d.c. converter stage, which in this case is 0.2Ω producing a theoretical acquisition time of $0.2\mu s$. However, the internal characteristics of the MAX180 allow the minimum conversion time to be $t_{conv}=1.875\mu s$, preceded by a delay of three clock cycles (Fig.3.30). Individual conversion times for all 8 channels are summed to produce an overall A/D conversion time. As the MAX180 is a 12 bit device a facility exists to read an initial 8 bits of the digital conversion and then the remaining 4 bits as separate operations.

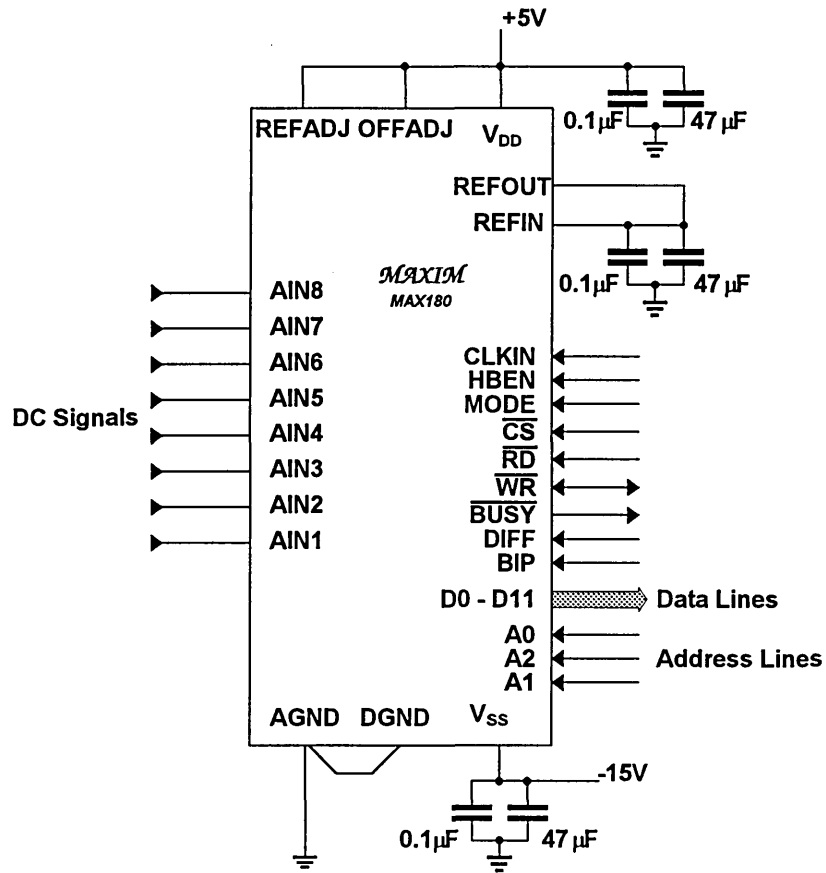


Fig.3.29 The MAX180 data acquisition device

The option used for the design presented here reads all 12 data bits in a single step to reduce data transfer and hence acquisition times.

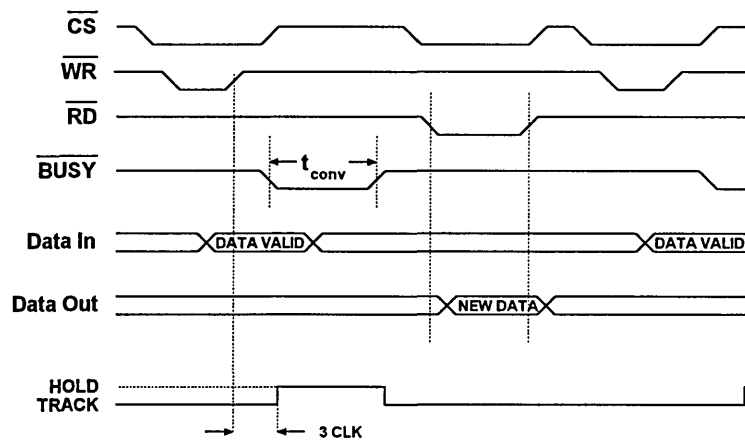


Fig.3.30 Timing diagram for the MAX180 data acquisition device

3.2.9 COMPUTER INTERFACE

All digital control signals required/supplied by the electrical resistance tomography hardware are provided by personal computer software via an Arcom PCIB40, 40 channel digital I/O board.

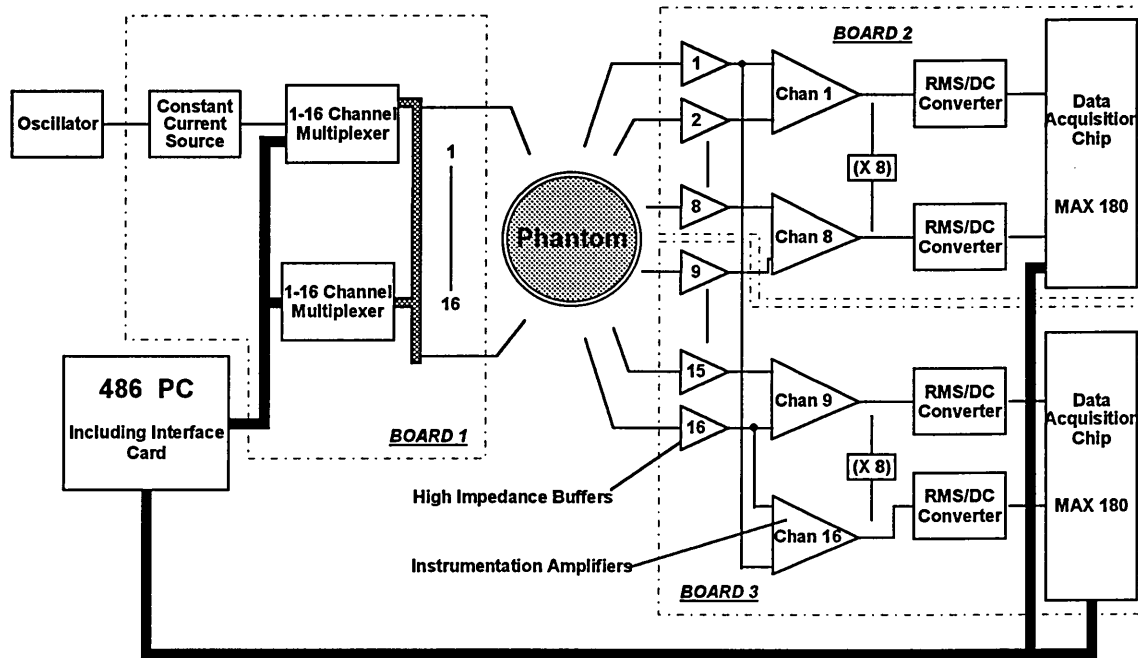


Fig.3.31 Component positioning and interconnection over 3 printed circuit boards

The PCIB40 provides 40 TTL lines which can be configured as input or output and is positioned in a spare expansion slot of a personal computer. Full details of the I/O board including software design considerations and memory addresses are presented in Appendix 1. All the electronic hardware constructed for this project is located on three printed circuit boards as illustrated in Fig.3.31. One circuit board is used for the current injection and driven shield components and the other two provide the 16 channels of data acquisition hardware. All connections between these three boards and

peripheral components is via a 64 way Eurocard 'backplane' as described in Appendix 1.

3.3 RESULTS

Results for three areas of investigation are presented in this chapter. Firstly, the 'background resistivity' is varied to test the resulting effect on image quality for a particular resistive discontinuity position. Secondly, measured data are presented for three dimensional experimentation including sets for liquid/solid flows. Finally, image reconstructions are presented (using the algorithm outlined in chapter 2) for single and multiple substance combinations. All experiments were carried out using an 8cm diameter phantom having 16 equidistantly spaced radial electrodes. An oscillator frequency of 8kHz coupled to a 5mA (r.m.s.) constant current source was used and the background conductivity was set to 11.5mS. The main purpose of these results are to verify the validity of earlier modelling and to investigate the ability of electrical impedance tomography to detect five substances: paper; plastic; gas bubbles; perspex and rubber singularly and in multiple combinations. Fig.3.32 illustrates a plan view of the labelling convention used for the different material positions.

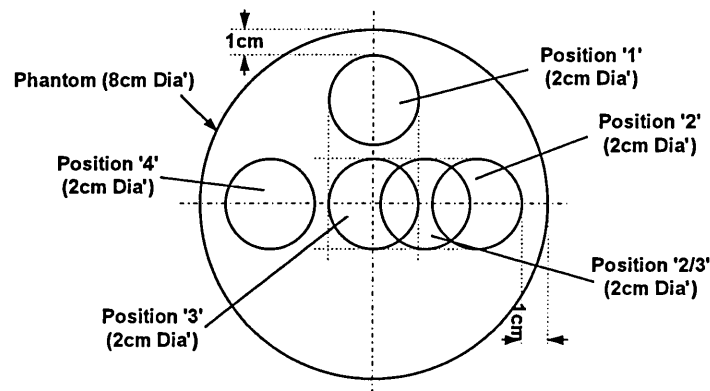


Fig.3.32 Positioning of substances

3.3.1 VARYING BACKGROUND CONDUCTIVITY

A link between background resistivity and image quality was investigated producing the results presented in Fig.3.33. A tubular rubber discontinuity of 2cm diameter was placed in position '3' (Fig.3.32), i.e. directly in the centre of the phantoms. Six simulations were carried out, each using different background conductivity values: (a) $217\mu\text{S}$ (b) 4.5mS (c) 7.9mS (d) 11.5mS (e) 14.4mS and (f) 17.45mS .

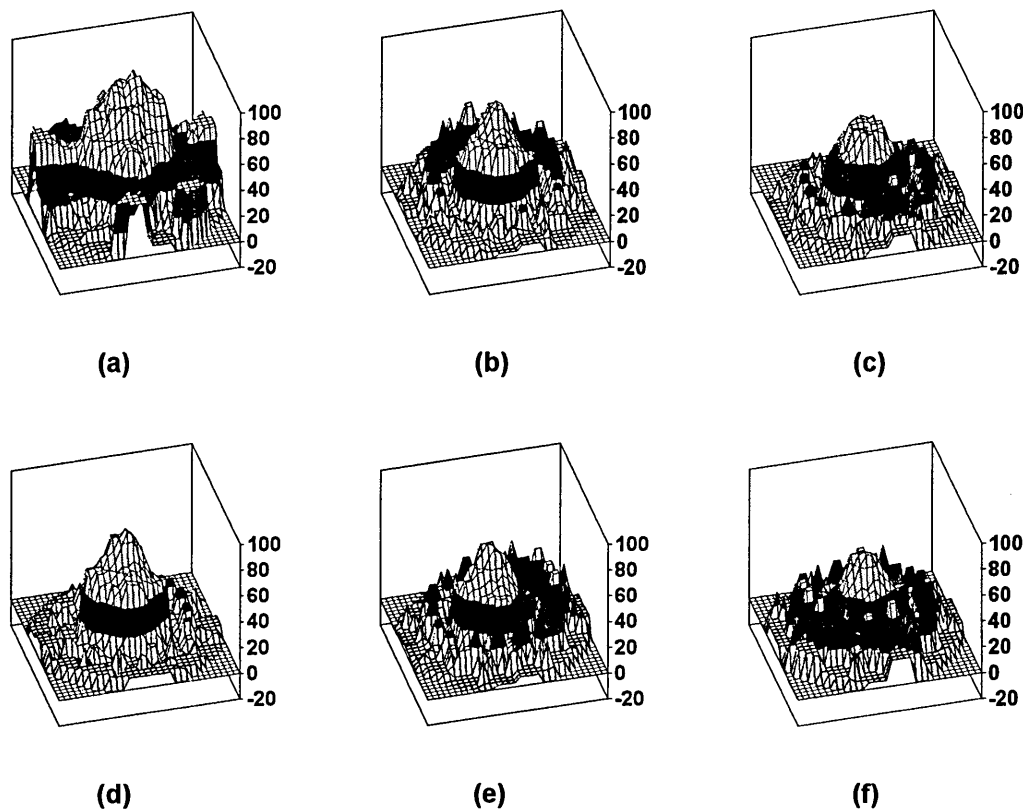


Fig.3.33 Various background conductivities: (a) $217\mu\text{S}$ (b) 4.5mS (c) 7.9mS
(d) 11.5mS (e) 14.4mS (f) 17.45mS

The system software reconstructs a resistivity profile, in the form of a 32×32 pixel array, using the reconstruction algorithm and software outlined in Chapter 2, and analyses the data to select the set having the highest individual resistivity value (R_{MAX}). This value is then used to convert all other values (R_N) from each set into percentages ($R_{\%}$):

$$R_{\%} = \frac{R_N}{R_{MAX}} \times 100 \quad \{3.8\}$$

These percentage values are displayed in Fig.3.33 for each data set. Although Fig.3.33 (d) does not contain the largest reconstructed resistivity value (R_{MAX}) it is the image with least noise interference. Consequently 11.5mS is used for all the data acquisitions in this chapter and those in chapter 5 which present details of a dual modality tomography system.

3.3.2 THREE DIMENSIONAL ANALYSIS

A potential problem associated with implementing an electrical impedance tomography system to measure flow rates of suspended solids is the three dimensional effect. It is not possible to limit current flow to two dimensions in a three dimensional flow, as is illustrated by the HSPICE modelling outlined earlier in this chapter.

Results presented in Fig.3.34 detail the effect that various lengths of tubular plastic (2cm diameter) have on the measured adjacent electrode potentials when using polar current injection over a single projection. The plastic tubing is moved, in 1cm steps, toward the electrode plane while remaining at discontinuity position '4' (Fig.3.32). Fig.3.34 illustrates how the voltage profile changes as the tube moves towards the electrode plane, where the data at the back of each graph is for the tube within the electrode plane. The results shown in Fig.3.35 repeat the steps presented above but for different radial substance positions (Fig.3.32): (a) position '2' (b) position '2/3' (c) position '3'. This provides information on how the radial position of a material affects the results as a function of its distance from the electrode plane.

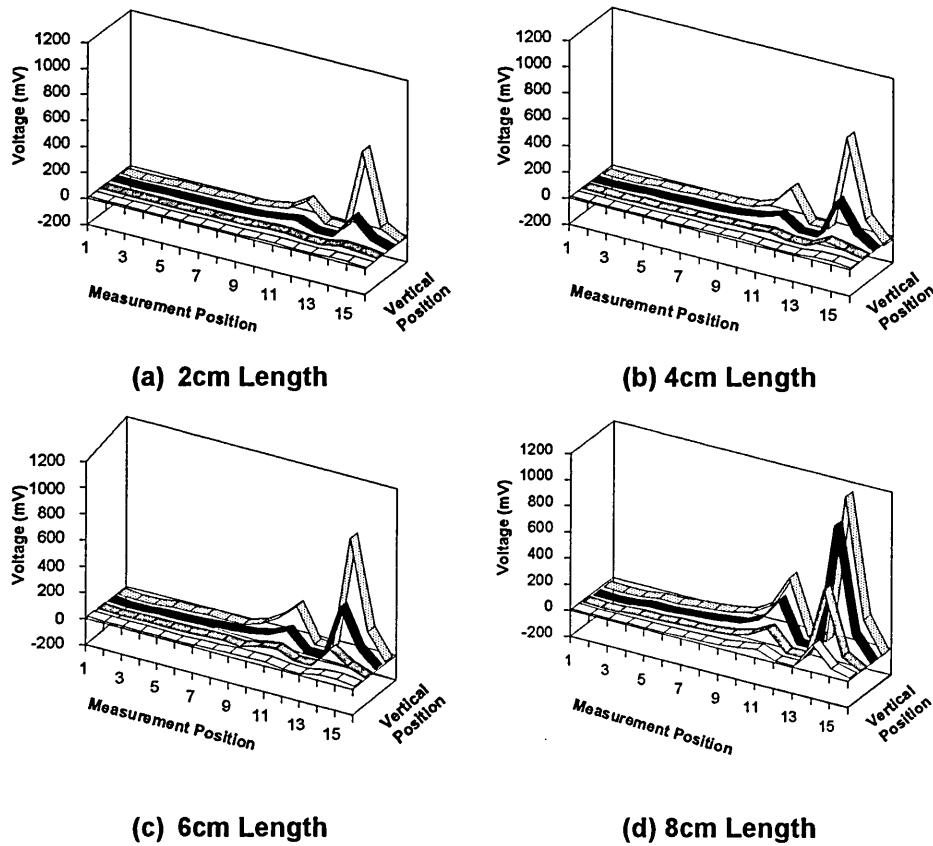


Fig.3.34 Varying lengths of 2cm diameter tube moved through the electrode plane

The modelling presented earlier in this chapter suggested that the closer an object is to the wall of the phantom the closer it has to be to the electrode plane before it affects the acquired data.

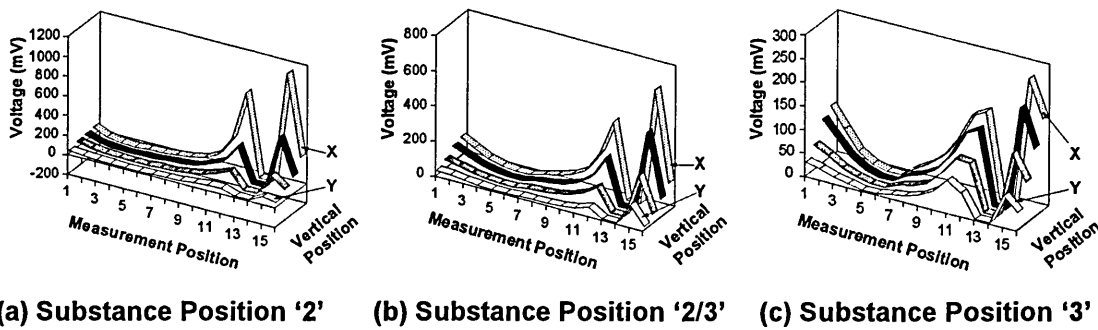


Fig.3.35 The 2cm Plastic pipe, in varying substance positions

It can be seen that the absolute measured potentials are higher for objects closer to the phantom wall (Fig.3.35 (a)), while objects nearer the centre (Fig.3.35 (c)) have a greater relative affect on the measured potentials at

distances further from the electrode plane. The latter can be seen more clearly when comparing voltage plots for vertical positions 'X' and 'Y' (Fig.3.35 (a - c)).

3.3.3 IMAGE RECONSTRUCTIONS FOR FIVE SAMPLES

This section presents image reconstructions for five substances that have differing physical properties. 2cm diameter cylinders of each material are used and Fig.3.36 presents the resulting image reconstructions for:

- (a) Paper tube (b) Plastic tube (c) Bubble
(d) Perspex bar (e) Rubber tube

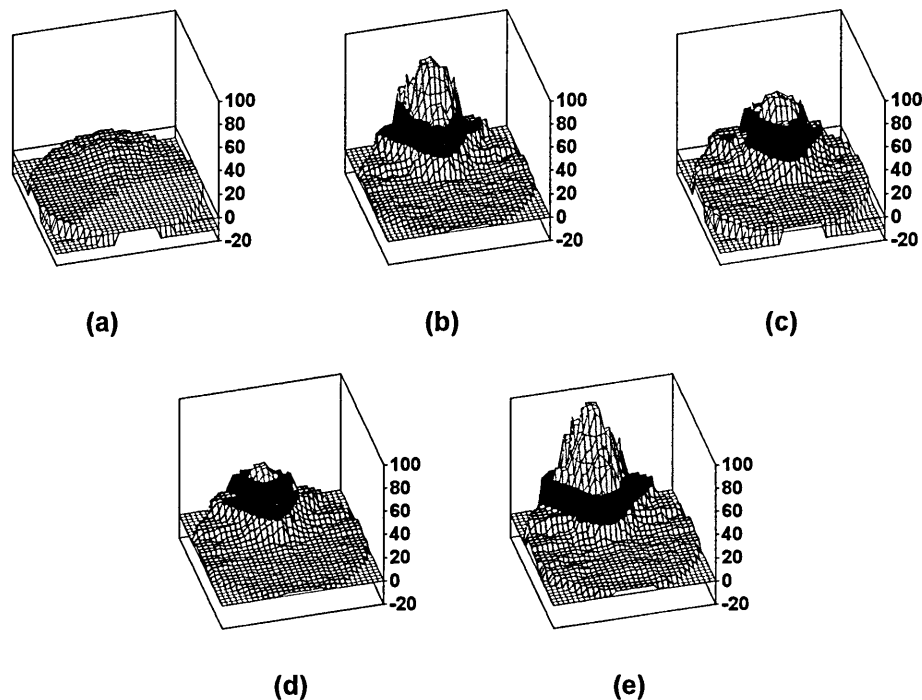


Fig.3.36 Image reconstructions for: (a) Paper tube, (b) Plastic tube, (c) Bubble, (d) Perspex bar, (e) Rubber tube

None of the image reconstructions shown in Fig.3.36 is filtered and therefore noise degradation is visible. This is because the relatively low signal to noise ratio present in the measured voltages has a bearing on image reconstructions for materials having low levels of contrast. The same approach was taken as

that detailed in section 3.3.1 when producing the image reconstructions, where each pixel location is converted to a percentage value of the largest overall resistivity (R_{MAX}). Using a percentage scale in this way allows a qualitative comparison of results and is employed in all situations where image reconstructions are compared. These results are discussed in the concluding section of this chapter (section 3.3.5).

3.3.4 IMAGE RECONSTRUCTIONS FOR MULTIPLE SUBSTANCES

This section presents image reconstructions for three combinations of two substances to allow comparison of the reconstructed images produced.

Fig.3.37 shows image reconstructions for: (a) Paper (position '1') and perspex (position '2'); (b) Rubber (position '1') and perspex (position '2') and (c) Rubber (position '1') and paper (position '2'). Each object is 2cm in diameter and Fig.3.32 illustrates where each is positioned within the phantom. These results are discussed in section.3.3.5.

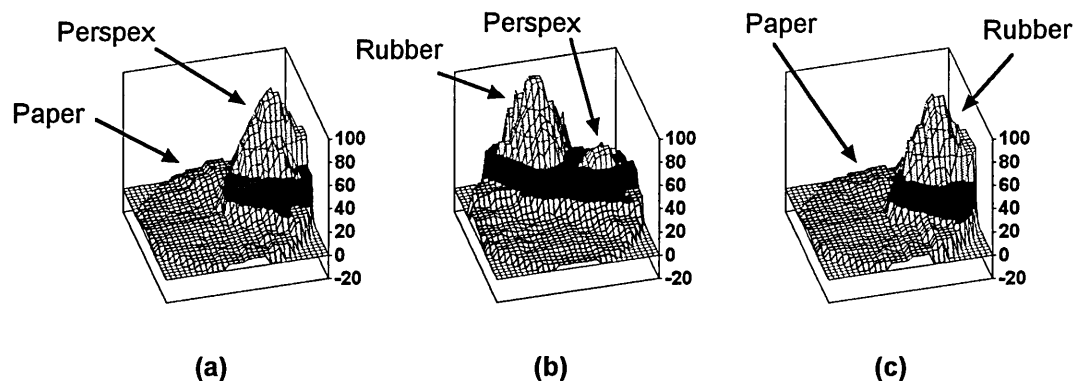


Fig.3.37 Image reconstructions for: (a) perspex and paper (b) perspex and rubber (c) rubber and paper

3.3.5 CONCLUSIONS FROM MEASURED RESULTS

The results presented in this chapter have demonstrated the operation of hardware designed and constructed to carry out electrical resistance

tomography. Fig.3.33 illustrates how the background conductivity affects the final image reconstruction, with a value of 11.5mS found to produce the best results. These changes are due to the physical limitations placed on the hardware when extremes of resistivity are present in the phantom. For low conductivities a high voltage is required to maintain a constant 5mA injection current and this may produce saturation in certain situations. For high conductivities a low voltage is required, producing results that are susceptible to a low signal to noise ratio.

Fig.3.34 presents measured voltages for a three dimensional situation where varying lengths of 2cm diameter plastic pipe are gradually lowered into a vertical phantom, from a point above the electrode plane. From these results it is evident that long objects produce larger measured voltage changes in relative terms at distances further from the electrode plane than shorter length objects.

Fig.3.35 repeats the test described for Fig.3.34 but lowers a plastic tube of 2cm diameter and length into the phantom. Three radial positions are used: one at the phantom's centre; one at the edge and one in an intermediate position. The results indicate that positions closest to the phantom wall produce the highest absolute measured electrode voltage disturbance while positions closest to the centre are more sensitive, in relative terms, to objects further from the electrode plane. This confirms the modelling presented earlier in this chapter which can be explained using Fig.3.38.

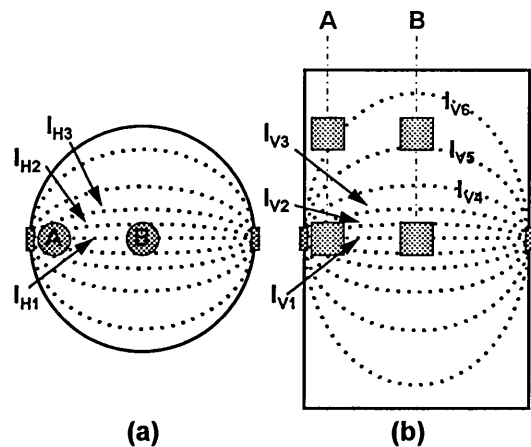


Fig.3.38 Three dimensional current paths

Two views of a three dimensional phantom are presented in Fig.3.38 for objects at radial positions 'A' and 'B'. Fig.3.38 (a) shows a plan view which represents both objects within the electrode plane. From this it can be seen that the current density due to the applied electrode voltage is greater for objects closer to the phantom wall. This is illustrated in Fig.3.38 (a) by three current paths (I_{H1} , I_{H2} and I_{H3}) intercepting the object at radial position 'A' while only two (I_{H1} and I_{H2}) intercept the object at radial position 'B'. Consequently, for objects at a particular distance from the electrode plane those closest to the phantom wall will produce the greatest absolute electrode voltage disturbance. However, as the object at position 'B' moves towards the electrode plane maintaining a constant radial position (Fig.3.38 (b)) it intercepts current path I_{V5} , earlier than the object at radial position 'B'. This results in image reconstructions for position 'B' being more sensitive to objects further from the electrode plane, in relative terms, than position 'A'. Fig.3.36 and Fig.3.37 present image reconstructions for five materials, both singularly and in selected pairings. These results indicate that saturated paper is not visible to electrical resistance

tomography; perspex is only partially visible and bubbles, plastic and rubber are all highly visible.

3.3.6 DISCUSSION OF DATA ACQUISITION SPEED.

One important aspect of any tomographic equipment design is the question of an acceptable data acquisition speed. Equation {3.9} presents a formula that illustrates this point:

$$d = n \times v \times t_a \quad \{3.9\}$$

Where 'd' is the **measurement distance** that a single object moves during the time taken to acquire a full set of readings; 'n' is the number of voltages that are acquired for a full set of data; 'v' is the flow velocity and 't_a' is the time taken for one voltage to be acquired. For the opposite method of data collection 96 unique voltage measurements are required to produce a full set of data.

The time taken to acquire this amount of data using the hardware presented in this chapter is approximately 80ms (eight unique current injection positions) when the r.m.s./d.c. converter settling time due to ripple voltages is taken into account. This produces a 'measurement length,' from equation {3.9}, of:

$$d = v \times 80.1 \times 10^{-3} m \quad \{3.10\}$$

Fig.39 draws this graphically as measurement length (d) 'vs.' velocity (v) for a variety of data acquisition speeds. From Fig.39 it can be seen that a flow having a velocity of 0.3ms^{-1} , monitored by a tomographic system that acquires a full set of data in 80.1ms will have a measurement length of 24mm. The hardware presented in this thesis is intended for use on a prototype system

with a flow velocity of less than 0.3ms^{-1} . This example illustrates the importance of fast data acquisition in commercial systems and this is addressed in chapter 7.

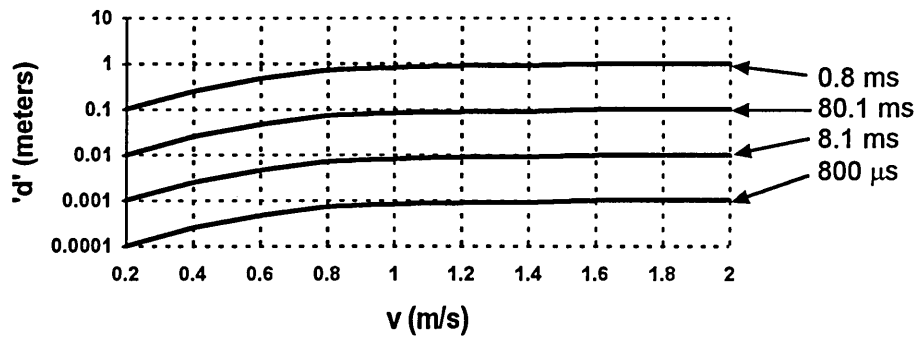


Fig.39 Distance 'd' vs. velocity 'v' for various data acquisition times

CHAPTER 4

OPTICAL TOMOGRAPHY

This chapter is divided into four parts. Firstly, models verifying the behaviour of light in liquid flows are developed; secondly, system hardware is discussed and circuit diagrams presented; thirdly, experimental results are presented to test the validity of modelled data and finally there is an analysis of the results.

4.1 MODELLING OF OPTICAL DISCONTINUITIES

This section describes optical modelling carried out to characterise certain aspects of liquid flows. Formulae are presented that illustrate the attenuation of light passing through various materials and multiple media combinations; the behaviour of light passing through a bubble within the conveying 'liquid' and refraction of light due to a variable depth conveying liquid. All of these situations affect the level of detected light and give an indication of the potential difficulties involved in using optical tomography for the characterisation of multi-component flows. Dugdale [17] describes several flow regimes that can occur in a two component liquid/gas flow but for the purposes of this thesis multi-component flows are assumed to be mainly liquid/solid. Gas bubbles are therefore optically modelled to assess the possible adverse affect that they may have on an optical tomography system.

When light passes through any non-opaque substance its intensity suffers attenuation due to many factors such as scattering, absorption and refraction. Scattering of light is complex to describe mathematically due to the random positioning of the particles responsible, but absorption and refraction may be

quantified by relatively simple mathematical models. Absorption occurs when incident light energy is converted to heat causing attenuation, and some materials exhibit selective absorption to specific frequencies of light.

Refraction happens at boundaries between optically different materials as the speed of light increases or decreases when moving from one to the other.

Refraction is a result of materials having different optical densities, a measure of which is provided by the refractive index of a material. Laws of refraction are available to describe general aspects of liquid/gas interfaces and these are used to construct more specific models related to bubbles.

4.1.1 ATTENUATION OF LIGHT

The attenuation of light in any isotropic optical material can be described by the following equation:

$$\ln(I) = \ln(I_0) - \alpha_n d_n \quad \{1\}$$

Where 'I' is the intensity of light received over a distance d_n , for an initial light intensity I_0 and an attenuation constant α_n . The attenuation constant is frequency dependent and therefore quoted for a particular wavelength (λ).

Over a particular light path there may be several substances having differing attenuation constants:

$$= I_0 e^{-\sum \alpha_n d_n} \quad \{2\}$$

Where 'n' is the number of materials negotiated by the light path, α_n is the attenuation constant and d_n is the distance travelled in each material.

Consequently, if d_n is summed for all possible values of n this will produce the

total path length. If this is applied to a phantom where light passes vertically through air and water (of variable depth), as illustrated in Fig.4.1 then only two attenuation constants are involved:

$$= I_0 e^{-(\alpha_a d_a + \alpha_w d_w)} \quad \{3\}$$

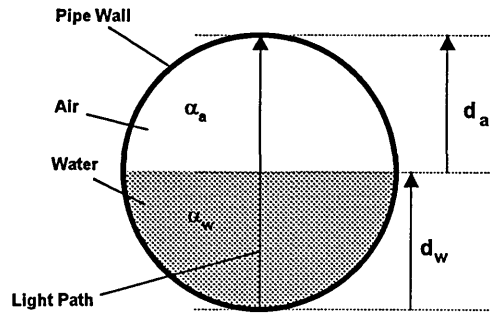


Fig.4.1 Variable water air boundary for a constant total path length

Where ($d_a + d_w =$ phantom diameter). At 930nm α_a and α_w are 0.142cm^{-1} and 0.287cm^{-1} respectively [16], producing maximum and minimum values for 'I' for an 8cm phantom of $0.321 \times I_0$ (maximum) and $0.101 \times I_0$ (minimum).

4.1.2 REFRACTION AND REFLECTION AT A 'BUBBLE' INTERFACE

Consider the situation of a light 'pencil' incident upon an air bubble, Snells' law states that:

$$\frac{\sin(\theta_i)}{\sin(\theta_r)} = \frac{\eta_{\text{air}}}{\eta_{\text{water}}} \quad \{4\}$$

Where θ_i is the angle of incidence, θ_r is the refracted angle after entering the bubble (Fig.4.2) and the refractive indexes of air and water are η_{air} and η_{water} respectively. For a horizontal pencil of light incident at a point 'A' above the optical axis of the bubble (Fig.4.2):

$$\sin(\theta_i) = \frac{h}{r}$$

Where 'r' is the radius of the spherical bubble.

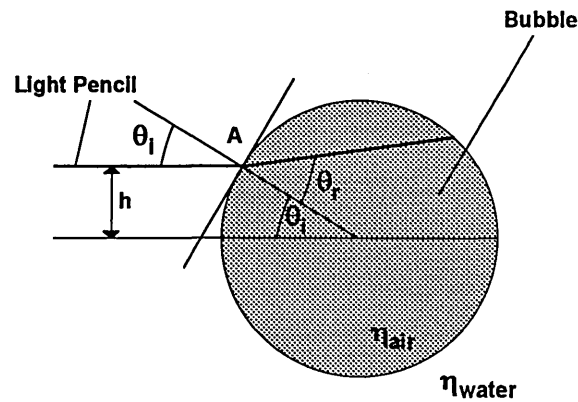


Fig.4.2 Refraction of light at a spherical water/air 'bubble' interface

Substituting in {4} and using values for η_{air} and η_{water} of 1 and 1.3 respectively

[16]:

$$r = \sin^{-1}\left\langle \frac{1.3 \times h}{r} \right\rangle \quad \{5\}$$

Therefore light pencils passing through this type of interface will diverge upwards, relative to the optical axis (Fig.4.2). Further diffraction occurs until the point of total internal reflection is reached, which happens when θ_r equals 90° :

$$\sin^{-1}\left\langle \frac{1.3 \times h}{r} \right\rangle = 90^\circ$$

Therefore:

$$h = \frac{r}{1.3} \quad \{6\}$$

Consequently, when the value of 'h' exceeds approximately 77% of 'r', total internal reflection takes place and any light striking above this point will not enter the bubble. Consider the three situations illustrated in Fig.4.3 where light pencils of differing sizes, relative to a bubble, are depicted. Equations {5} and

{6} allow an estimate of the refractive/reflective effect to be calculated for a bubble and light pencil of known dimensions.

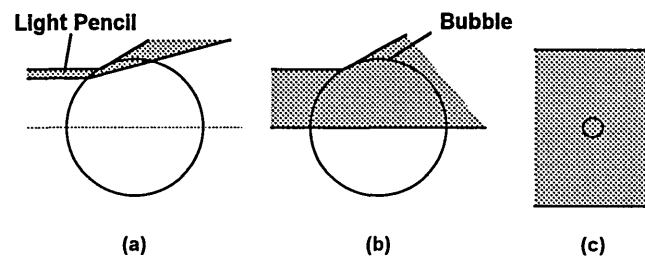


Fig.4.3 Light pencils of varying relative size

They also allow generalisations to be applied, for example Fig.4.3 (a) shows a bubble that is large (in relative terms) to the light pencil and under certain circumstances no light will be transmitted towards the initial point of aim.

Fig.4.3 (b) shows a smaller bubble, in relative terms, and here a proportion of the light pencil is totally deflected; most is partially deflected and a fragment passing along the central bubble axis suffers no deviation. Fig.4.3 (c)

represents a very small bubble within a light pencil and because most of the light passes around the bubble there is a minimal affect on sensors positioned at the point of aim.

For these reasons it is not adequate to model only the attenuation characteristics of the two component water/air interface of a bubble, equation {3}. This is because refraction and reflection may have a more significant affect than attenuation on the light intensity detected at a sensor as a diverging beam will produce a reduced light intensity per unit area. Consequently, an important consideration is the bubble's size and distance from any light sensor as this is the controlling factor in the level of divergence that occurs, and the next section models this.

4.1.3 DIVERGENCE DUE TO 'BUBBLE' INTERFACES

Fig.4.4 (a) illustrates the divergent effect of a bubble suspended in liquid on a thin, incident light pencil where 'Disp' is the total deviation of the beam from its original path. The triangle 'abc' is isosceles and therefore $\theta_r \equiv \theta_{ii}$. Using equation {4} and values for η_{air} and η_{water} of 1 and 1.33 respectively:

$$r_r = \sin^{-1} \left\langle \frac{\sin(\theta_r)}{1.33} \right\rangle \quad \{7\}$$

From Fig.4.4 (a):

$$\theta_t = 180 - \theta_r - \theta_{ii} \quad \text{and} \quad \theta_x = 180 - \theta_t - \theta_i$$

$$\therefore \theta_x = 2\theta_r - \theta_i \quad \{8\}$$

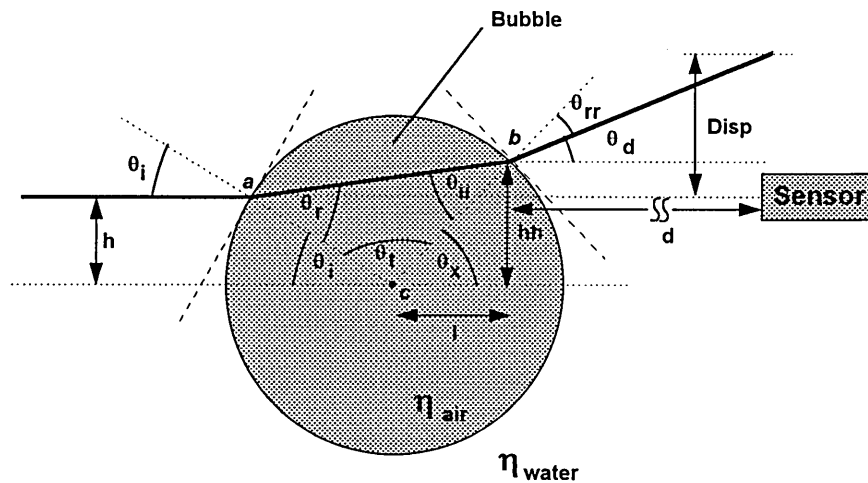


Fig.4.4 (a) Divergence at a bubble interface

It is also possible to deduce the height 'hh':

$$hh = r \times \sin(\theta_x) = r \times \sin(2\theta_r - \theta_i)$$

From Fig.4.4 (a) and equations {7} and {8}:

$$d = \theta_x - \theta_{rr} = 2\theta_r - \theta_i - \sin^{-1} \left\langle \frac{\sin(\theta_r)}{1.33} \right\rangle \quad \{9\}$$

The portion of Fig.4.4 (a) referring to the displacement 'Disp' can be redrawn as Fig.4.4 (b).

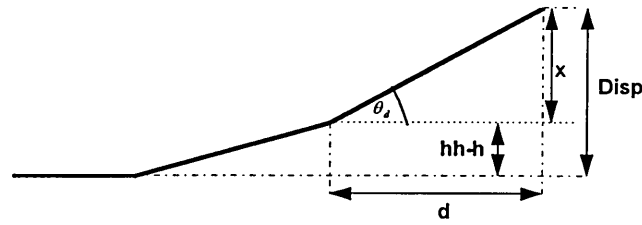


Fig.4.4 (b) Derivation of the displacement 'Disp'

From this: $x = d \times \tan(\theta_d)$, giving a total displacement of:

$$\text{isp} = (hh - h) + d \tan(\theta_d) \quad \{10\}$$

Therefore if the bubble were to move along the axis of the light pencil, towards the light source, θ_d , 'hh' and 'h' would remain constant and the distance 'd' would be the only variable. Under these conditions the displacement (Disp) would be linearly proportional to the change in 'd'.

4.1.4 REFRACTION DUE TO A VARIABLE LIQUID DEPTH

A major characteristic of some suspended solid flows, such as those found in sewer outflows etc., is the variable depth of the conveying liquid. This introduces added complexity for optical hardware design, as at certain times, there will exist a water/air interface for non horizontal light beams, as illustrated in Fig.4.5. In order to simplify the model the assumption is made that the water depth is only 50% of the maximum allowing the radial displacement ' α ' to be calculated. The circumference of a circle is $2\pi r$ and the angle of deviation that produces ' α ' can be stated as Deviation = $\theta_r - \theta_i$. Therefore:

$$\alpha = \frac{\text{Deviation}}{360} \times \text{Circumference} = \frac{(\theta_r - \theta_i)}{180} \times \pi r \quad \{11\}$$

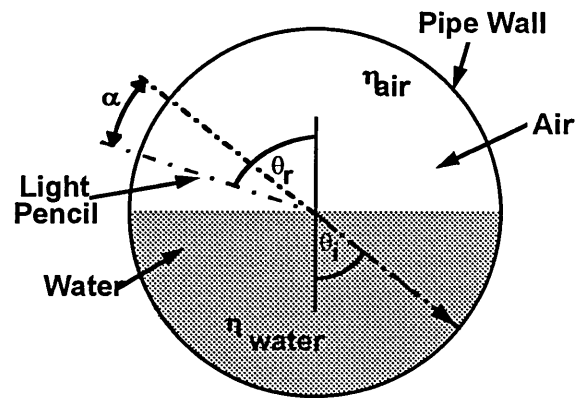


Fig.4.5 Refraction due to a variable conveying liquid depth

Using Snells' law to determine θ_r from θ_i {4} this can be rewritten as:

$$= \frac{\sin^{-1}[1.3 \times \sin \theta_i] - \theta_i}{180} \pi r \quad \{12\}$$

Which is plotted graphically in Fig.4.6.

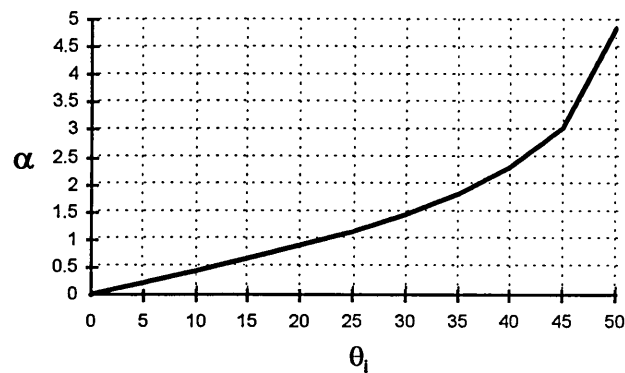


Fig.4.6 Graph of θ_i versus. ' α ' for equation {12}

4.1.5 MODELLING CONCLUSIONS

Modelling described in this chapter investigates the behaviour of light for two possible situations, for air bubbles present in liquid flows and for liquid/air boundaries in variable depth flows. Section 4.1.1 examines the equations governing attenuation of light and Fig.4.1 relates this to conditions where light moves from liquid to air with an angle of incidence of 90° . Fig.4.2 illustrates the effect of refraction due to bubbles in liquids and Fig.4.3 links this to bubble and

light beams of various sizes. The main conclusion that can be drawn is that light pencils with a width significantly less than the bubble diameter will pass unaffected through a bubble centre. For other paths through the bubble it will be reflected, refracted and deviated to varying degrees up to the point of total internal reflection, after which point the beam is deviated only.

Fig.4.4 (a) progresses a stage further by examining the level of displacement that a light pencil receives when a bubble moves along different optical paths. This displacement is significant for all circumstances other than when a relatively 'thin' light pencil passes through the bubble centre, producing the relationship described in equation {10}.

Finally, Fig.4.5 illustrates how far a light pencil is displaced from its original target point when passing through an air/liquid boundary with varying angles of incidence. It appears to be non-linear and significant for relatively small angles of incidence.

4.2 HARDWARE

Hardware designed for the optical tomography system falls into three categories. Firstly, control of the optical sources for the selected projection is required; secondly, buffering, amplification and conversion to a digital format of the optical sensor voltages is carried out and finally a personal computer interface is utilised to acquire the digital data and supply the necessary control signals. The design in Fig.4.7 uses the spare channels from the 40 channel digital I/O board described in chapter 3. Logic decoding of the four address lines supplied by the I/O port (Appendix.1) is carried out, to allow expansion of

the system to eight optical projections. Two 8-bit data latches store (in a digital format) control bits for the selected LEDs and present them to an 8-bit LED driver device, which uses them to select specific combinations of LEDs for application of the 15V supply voltage.

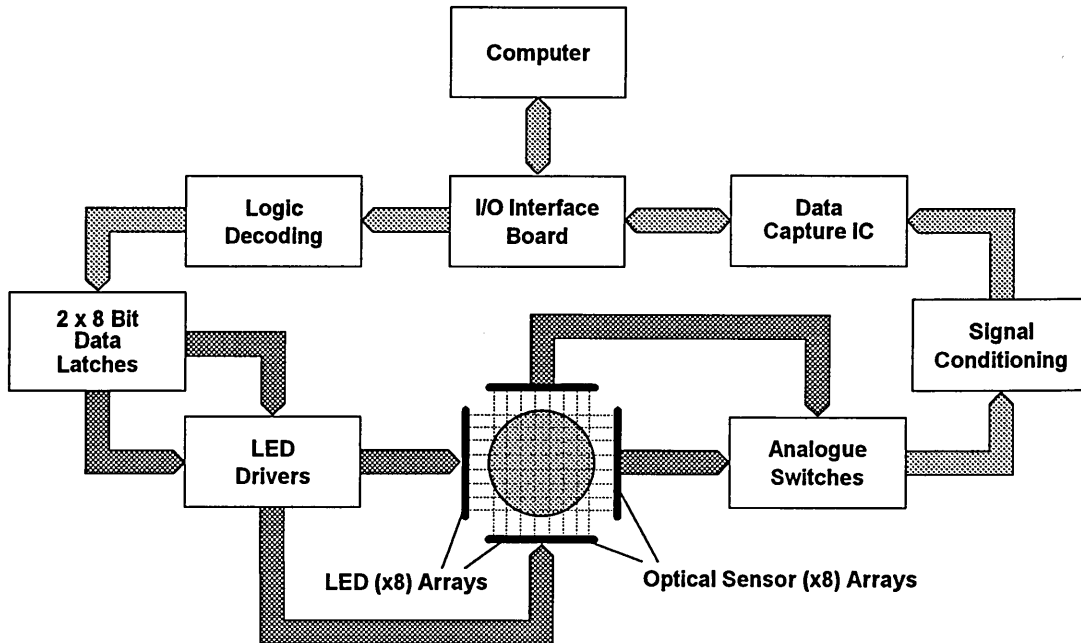


Fig.4.7 Schematic diagram of an Optical Tomography system.

Analogue switches are used as multiplexers to connect the eight analogue sensor currents associated with a particular optical projection to signal conditioning circuitry, which converts them to voltages and amplifies the result. These amplified voltages are then transferred to a data capture integrated circuit which converts them to a digital format. Finally, these digital values are passed to a personal computer via a 40 way digital I/O port (Appendix 1) for processing by the system software (Chapter 2).

4.2.1 OPTICAL TRANSDUCERS

The circuitry presented in this chapter switches an optical source on, configures the signal conditioning circuitry, takes a set of readings and

switches the optical source off. The choice of what type of light emitter and sensor to use depends on the application, as some situations demand light at a specific frequency to gain full advantage of an optical window in the attenuation spectrum of the conveying medium [7].

Various forms of emitters and sensors exist including filament light sources, LEDs, laser-diodes, photo-diodes, photo-transistors and light dependent resistors. Choice of emitter is usually constrained by the requirement to collimate the radiated light pencil in order to maximise incident light intensity and reduce the magnification of reconstructed images. To achieve good collimation the choice of light source would be a **laser-diode** due to its excellent coherence, low spectral width, high optical intensity and fast switching times. The main drawback of this type of device is its cost, at £20+ per device (excluding lenses). Most **filament** light sources are extremely incoherent when focused and have very slow turn on/off times leaving **LEDs** as the most cost effective option for the prototype design.

There are various categories of LED each having differing characteristics, but for the prototype system a Siemens SFH484-2 was chosen due to its low cost (less than £1.00 each), small half angle and a peak wavelength that is readily matched to a standard photo-diode detector. This device has a peak wavelength of 880nm and a half angle of 8° allowing it to be collimated in a phantom of a radius of 8cm without gross degradation of optical intensity at the sensor. Collimation is achieved using a mounting arrangement that restricts

the light to a narrow 'pencil' (Fig.4.8). Table 4.1 lists the major characteristics of the Siemens SFH484-2 LED [41].

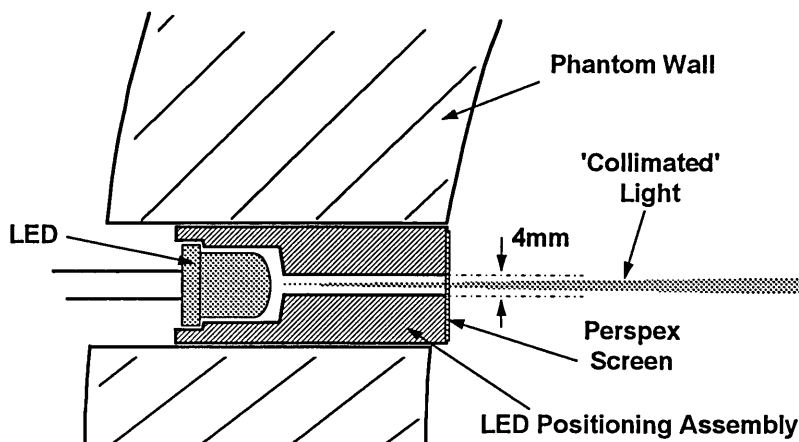


Fig.4.8 A collimated light source

Types of sensor available are more numerous than types of emitter and include the families of photo diodes, photo voltaic cells, photo transistors and photo multipliers. Here also the choice of sensor is application and budget dependent. Ideally it has a linear characteristic, generates an electric current as a function of incident light and has a fast response time.

Light Output (@ 100 mA)	15 mW
Half Angle	8°
Peak Wavelength	880 nm
Turn 'ON' Time (t_r)	0.6 μ s
Turn 'OFF' Time (t_f)	0.5 μ s

Table.4.1 Characteristics of the Siemens SFH484-2 LED

Equation {13} is an outline response function, where I_i is the current produced due to the light intensity, L_i , incident on the sensor which has a constant of proportionality Φ .

$$I_i = \Phi \times L_i \quad \{13\}$$

The **photo multiplier** is a complex device in which the incident light on a particular material causes the emission of charged particles (usually electrons) which are increased in velocity by the application of an electric field. Several such sections can be connected in series with the final device producing an image on a coated screen which phosphoresces when the charged particles strike.

The **photo voltaic cell**, more commonly known as the light dependent resistor (LDR), is the simplest of all the light sensing devices. Incident light photons provide the extra energy required for charge carrying particles to bridge the depletion region of a PN junction, thus reducing the resistance 'seen' by an applied voltage. These types of device are usually non-linear, have extremely slow response times and require a large surface area to sense very low levels of light.

The **photo diode** also uses a PN junction to generate free charge carriers in the presence of light creating an increase in reverse current, known as photo current, proportional to the incident light intensity. This photo current is usually in the order of nA and occurs when the device is connected in reverse bias mode. The main disadvantage of the photo diode is the necessity of a large gain amplifier to convert these very small photo currents into measurable voltages.

The **photo transistor** partially overcomes this limitation by using the current generated by a PN junction as the base current of an adjoining transistor therefore effectively amplifying the signal. This added complexity produces

drawbacks as the resulting devices are less linear than a photo diode, slower and also more sensitive to temperature variations.

A Siemens SFH2030 Photo-diode was chosen due to its fast switching speed, excellent linearity and a peak spectral response close to that of the emitter.

Table.4.2 illustrates the main characteristics of this device [41].

Sensitivity (@ $\lambda=850$ nm)	0.62 A/W
Half Angle	40°
Peak Response	850 nm
Turn 'ON' Time (t_r)	0.002 μ s
Turn 'OFF' Time (t_f)	0.002 μ s

Table.4.2 Characteristics of the Siemens SFH2030 Photo-diode

In order to reduce the effect of reflections on the SFH2030 due to its large half angle acceptance cone, it was positioned away from the conveying liquid, in a hollow circular section fronted by a clear plastic film. This is illustrated in Fig.4.9.

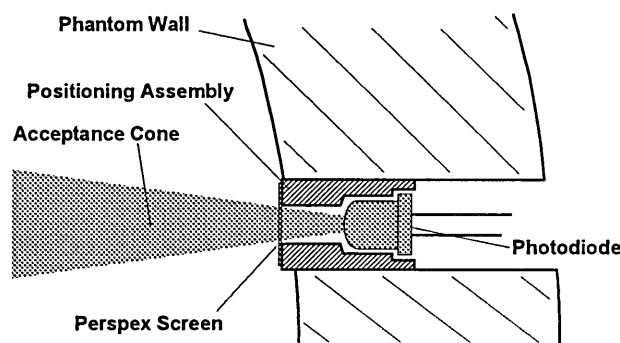


Fig.4.9 Positioning of the photo diode within the phantom cross section

4.2.2 LOGIC DECODING / DATA LATCHES

The complete optical tomography system is designed to provide two 'projections', each having eight 'views', although expansion to a maximum of eight separate projections is possible. More than one optical projection is

achieved by decoding the three available address lines (A_0 , A_1 and A_2), using a 74LS138 3 to eight line digital decoder, as shown in Fig.4.10. Table.4.3 illustrates how the address bus is decoded to allow selection of the correct projection, although for two projections only '1' and '2' are used.

A_0	A_1	A_2	Selected Projection
0	0	0	1
0	0	1	2
0	1	0	3
0	1	1	4
1	0	0	5
1	0	1	6
1	1	0	7
1	1	1	8

Table.4.3 Selection of 'Projection' by address decoding

Consequently, to make projection '1' the **active** projection address 000 is selected, and CS (OPTICAL - 1) is set 'HIGH'.

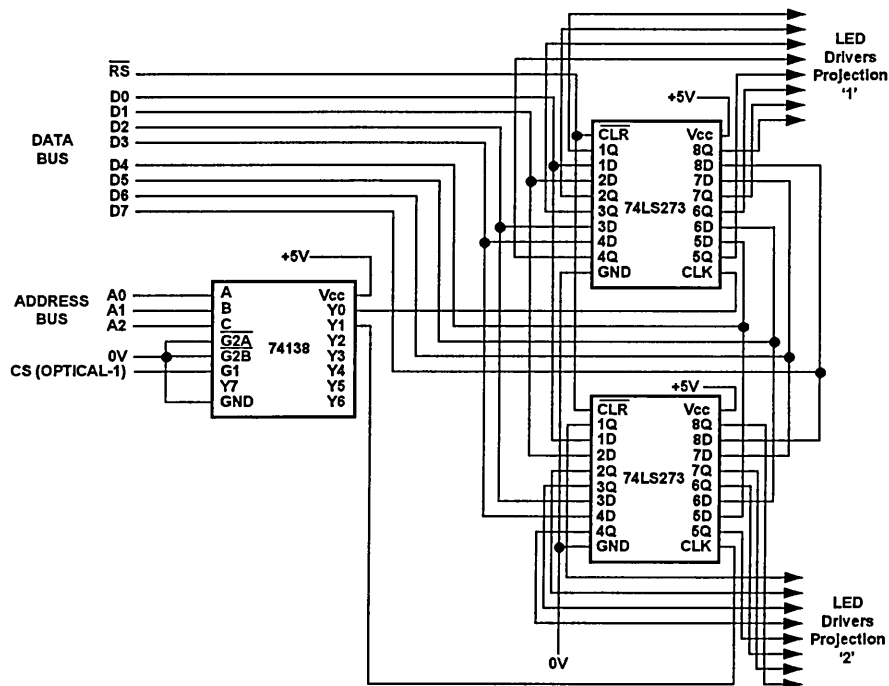


Fig.4.10 Address decoding and data latching circuit (2 projections)

On the positive going edge of CS (OPTICAL - 1) the current value on the data bus is transferred to the outputs of the 74LS273 8-bit latch associated with the

active projection. For example, if LED 3 of the active projection is to be turned on then the data bus is set to 00000100. Fig.4.11 illustrates the delay, t_1 (of 5ns) taken for the 74LS138 to respond to a particular address and the time t_2 (of 15ns) taken for the 74LS273 to latch.

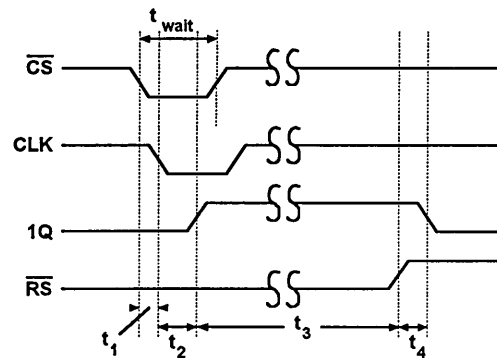


Fig.4.11 Timing diagram for the decoding circuit

The selected LED remains 'ON' for a time t_3 (Fig.4.11) which is variable and controlled by the system software and t_4 is the time taken for the Siemens SFH484-2 LED (section 4.2.1) to switch 'OFF' after \overline{RS} (the reset pin) is pulsed 'LOW'.

4.2.3 LED DRIVERS

The outputs from the data latching circuits are used to control a specialised LED driver, the ULN2803 (Fig.4.12), which is TTL compatible and capable of switching 0.5A per channel and 2.2W (@50V) over all eight channels if selected concurrently. Two ULN2803 devices are required, one for each optical projection, with the output pins ($O_1 - O_8$) connected to eight LEDs via current limiting resistors.

The suggested operating current [41] for the Siemens SFH484-2 LEDs is 20mA. This can be increased to 100mA if the devices are pulsed on for less than 1ms, which is well within the limits of the ULN2803 drivers.

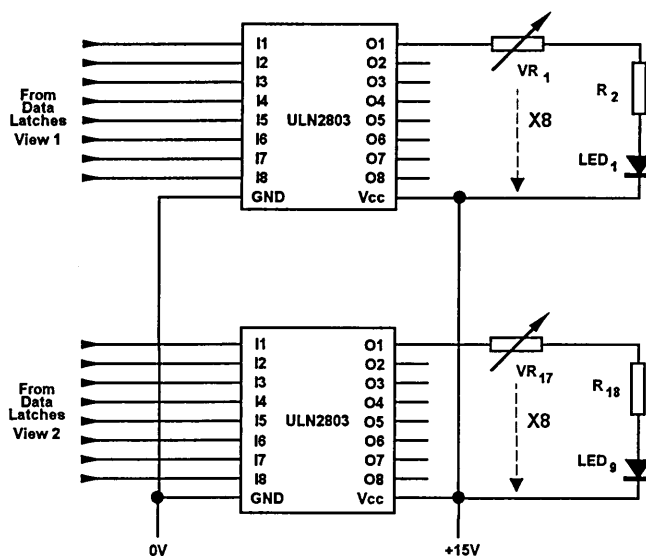


Fig.4.12 LED driver circuit

An LED current range of 10mA to 70mA was chosen to allow the brightness levels to be varied if required, producing resistor values for VR_1 and R_2 of 200Ω and 1200Ω respectively. Variation of VR_1 causes the brightness of each LED to change.

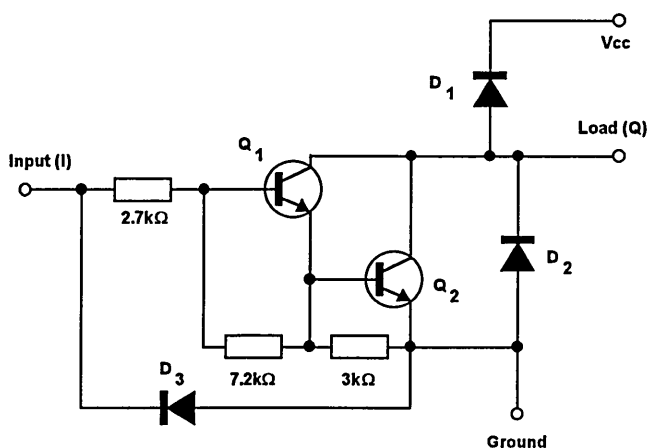


Fig.4.13 Internal structure for single channel of the ULN2803

The ULN2803 comprises a single Darlington driver per channel (Fig.4.13) to allow switching of relatively large currents. This type of configuration acts in

the same way as a single transistor but has a total current gain (β) equal to the product of those of both transistors and a high input resistance to allow safe connection to TTL logic circuitry. The $3k\Omega$ resistor acts to improve the turn on/off speed of the circuit.

4.2.4 ANALOGUE SWITCHES

Measurements are made for a single optical 'projection' at a time and therefore only one data acquisition device is required. Consequently, some form of sensor multiplexing is required and this is achieved by using two DG309 (quad) analogue switches, per projection (Fig.4.14). To permit future expansion a 3 to 8 line address decoder device (74LS138) is used to decode the 3 available address lines allowing a total of 8 projections to be monitored. A block diagram of the complete circuit for two projections is illustrated in Fig.4.15. The DG309 produces a low resistance between its inputs (D_n) and outputs (S_n) when a logic LOW is applied to the corresponding control pins (IN_n), returning them to a high resistance when a logic HIGH is applied.

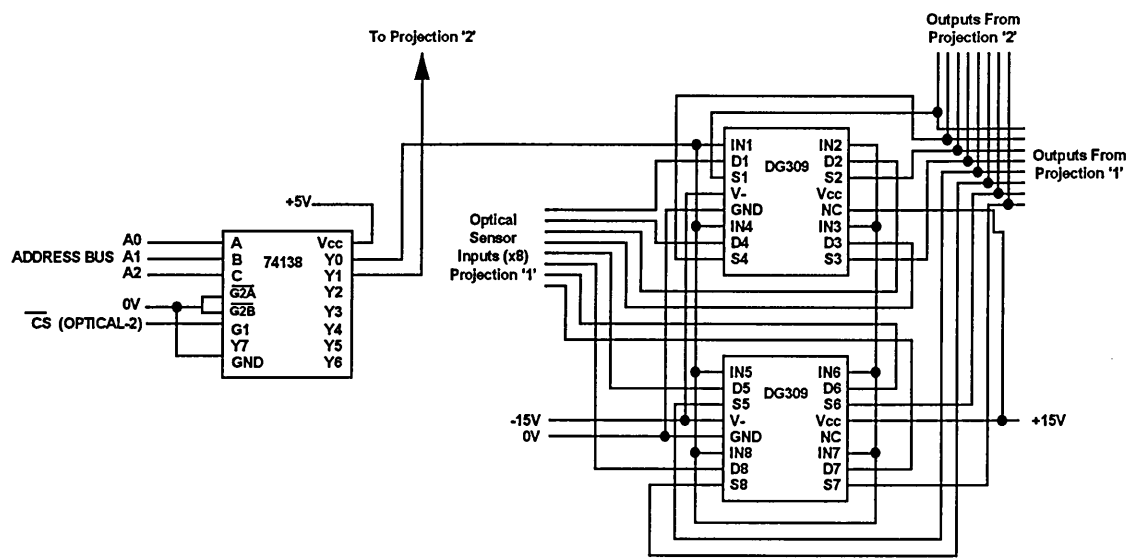


Fig.4.14 Analogue switches (1 projection only)

Two DG309s are used in parallel providing 8 analogue channels with inputs derived from the optical sensors and outputs connected to the eight input channels of a data acquisition device (section 4.2.6). The control inputs to the analogue switches for a particular projection are all supplied by a single output of the address decoder.

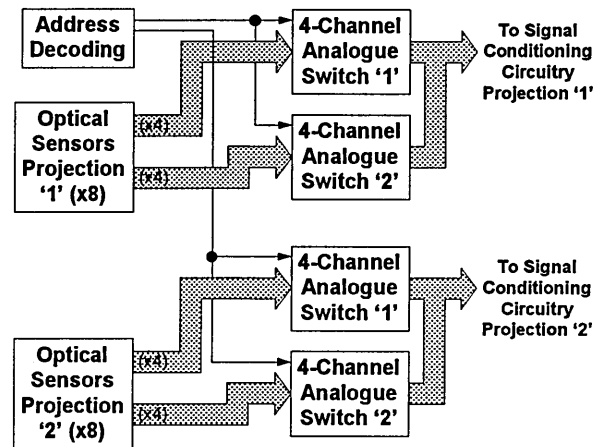


Fig.4.15 A block diagram of the total analogue switch circuit for 2 'projections'

Projection '1' is selected by setting the address bus (A_0 , A_1 and A_2) to 000 and pulsing \overline{CS} 'LOW' (Fig.4.16). Following a delay (t_1) of 5ns, $IN_1 - IN_8$ also go LOW connecting the individual cathodes of the optical sensors (section 4.2.1), for projection '1', to the signal conditioning circuit.

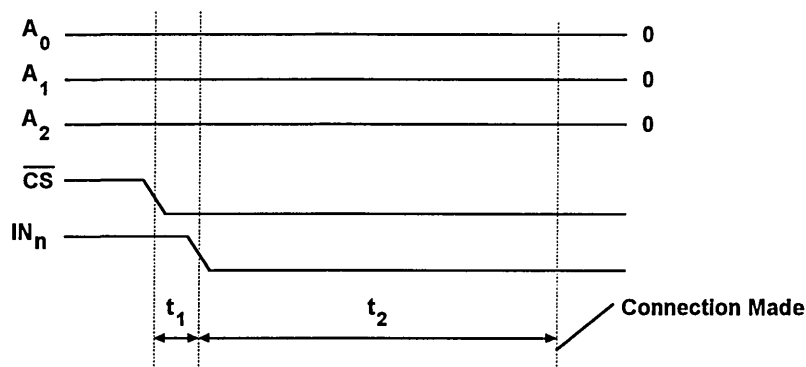


Fig.4.16 Connection of channel 1 sensors to the signal conditioning circuit

The analogue switching time (t_2) taken to make this connection is approximately 130ns which is a relatively long delay compared to those

involved in TTL logic circuitry, but as this only occurs once per channel this is not significant.

4.2.5 SIGNAL CONDITIONING

Incident light falling on a reverse biased SFH2030 pin photo-diode causes a current to flow with a magnitude that is a function of the light intensity. To interface this signal to a computer it has to be converted to a voltage in the range 0-5V (compatible with the data acquisition device of section 4.2.6), requiring a current to voltage converter with a high gain (Fig.4.17).

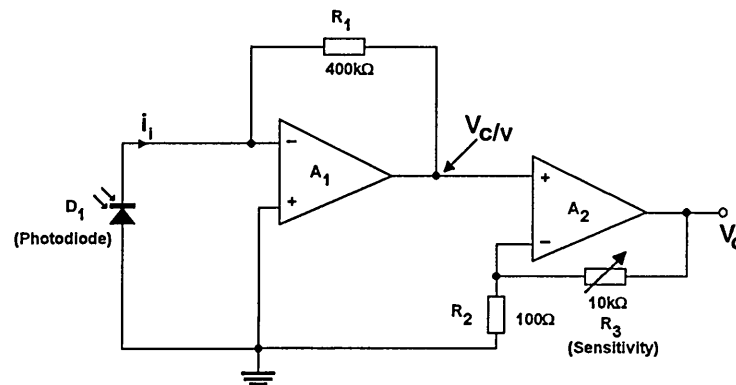


Fig.4.17 Signal conditioning circuit (single channel) and amplifier

The output voltage of A_1 , described by equation {14}, has a magnitude proportional to the current produced by the photo-diode and resistance R_1 . A_2 is a non-inverting amplifier supplying secondary gain to reduce the size of feedback resistor required in the first stage. Consequently, two stages are used to minimise noise levels that would occur with very high gain, single stage operational amplifiers. Equation {15} describes the output voltage of Fig.4.17.

$$V_{c/v} = i_i \times R_1 \quad \{14\}$$

$$V_o = \left\langle 1 + \frac{R_3}{R_2} \right\rangle \times i_i \times R_1 \quad \{15\}$$

The Siemens SFH2030 photo-diode produces a current of approximately 120nA when positioned 8cm away from a Siemens SFH484-2 LED in distilled water. Therefore the following resistor values are required for this current magnitude, to produce an output voltage of 5V (a variable resistor (R_3) is used to allow fine tuning of the output level for sensor/emitter separations other than 8cm):

$$R_1 = 400k\Omega, \quad R_2 = 100\Omega, \quad R_3 = 10k\Omega \text{ (var)}$$

4.2.6 DATA CAPTURE

Once the sensors associated with a particular optical 'projection' are selected the resulting amplified voltages are passed directly to a MAX155 [30] 8 channel, 8 bit data acquisition device (Fig.4.18).

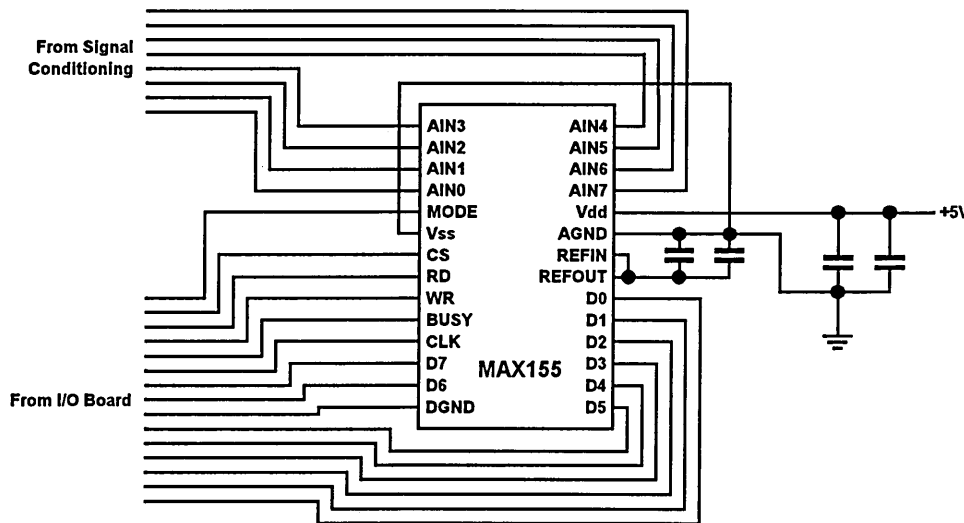


Fig.4.18 8 channel data capture using the MAX155

This device contains eight parallel sample and hold circuits that are internally multiplexed to an 8-bit A/D converter which stores the resulting eight conversions in internal 8X8 RAM. The MAX155 has a conversion time of 3.6 μ s per channel, an internal 2.5V reference and a single +5V operation.

Conversions are initiated by a pulse to the \overline{WR} pin and data sets are accessed from the onboard RAM with a pulse to the \overline{D} pin. A digital output is provided via an 8-bit tri-state buffered data bus and this is also used to configure internal registers which control operations such as addressing the internal RAM, power down, inhibit and conversion polarity. However, the design illustrated in Fig.4.18 uses the MAX155s hardwired mode of operation requiring no initial register configuration.

To make a full set of readings all 8 channels are sampled by the internal sample and hold circuitry when \overline{CS} and \overline{WR} go LOW (Fig.4.19), and A/D conversion commences when these return HIGH. The sample and hold acquisition time is between 800ns and $1\mu\text{s}$ and the A/D conversion time (t_{conv}) can be calculated using equation {16}, where 'N' is the number of channels to be converted (which for single ended 8-bit mode is 8).

$$t_{\text{conv}} = \frac{(9 \times N \times 2)}{f_{\text{clk}}} \quad \{16\}$$

With a clock frequency of 5MHz a total conversion time (including sample and hold delays) of $29.8\mu\text{s}$ can be achieved allowing both optical projections to be sampled in less than $60\mu\text{s}$.

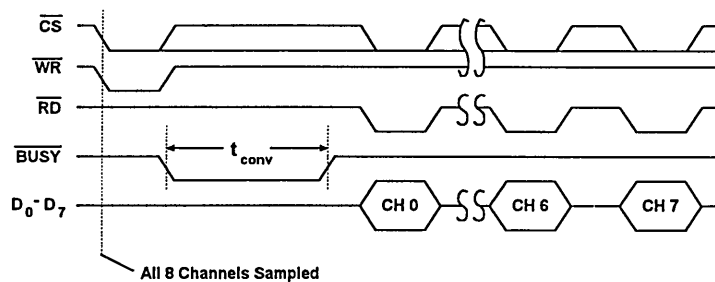


Fig.4.19 Hard-wired mode timing, eight single ended conversions

Once conversion is complete \overline{USY} returns HIGH allowing data for each channel to be placed on the data bus once \overline{D} has been taken LOW. The data is supplied to the data bus in sequential order from CH0 to CH7.

4.2.7 COMPUTER INTERFACE

All digital control signals and data lines required by the hardware are supplied via a 40 channel digital input/output (I/O) board. The I/O board is positioned in a spare expansion slot of an IBM compatible computer and mapped into two vacant memory locations allowing access by the system software. A full outline of the system software is given in chapter 2 and a description of the I/O board is presented in Appendix 1. The circuitry described in sections 4.2.2 - 4.2.6 of this chapter is constructed on two printed circuit boards. On the first board is the circuitry to control the LED switching and on the second are the optical sensor signal conditioning and A/D conversion components. Each board connects to a common 'backplane' via a Eurocard connector (as described in Appendix 1).

4.3 RESULTS

Results presented in this chapter test the validity of the modelling outlined earlier and demonstrate reconstructed images for five different materials using the back-projection reconstruction algorithm described in chapter 2. These reconstructions are for each of the five substances in isolation and also for selected multiple combinations. The voltage scale used to present all the results in this section originates from the digital value obtained from the

analogue to digital (A/D) converter. Therefore, maximum attenuation of the light source is represented by a value of 255 and minimum by 0 (8 bit).

4.3.1 DETERMINATION OF ' α ' FOR AIR AND WATER

Fig.4.20 is a graph of sensor voltage (V_d) for a partially collimated light beam in air for an increasing path length d . The LED emitter was pulsed with a current of 20mA, using a supply voltage of +15V. The PIN photo-diode sensor was sampled using a single channel of the data acquisition circuit outlined in section 4.2 of this chapter.

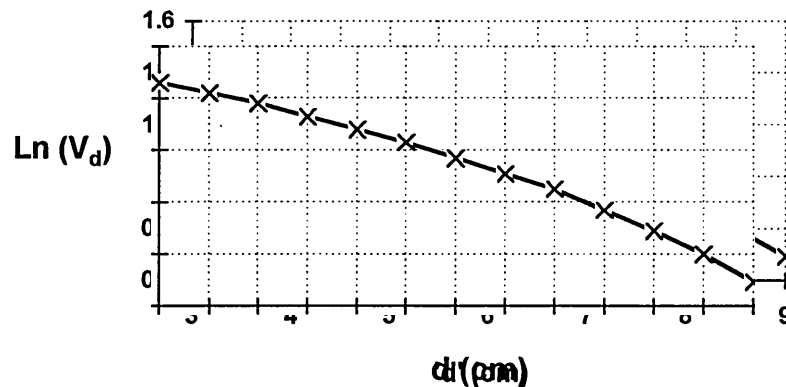


Fig.4.20 Attenuation in AIR as a function of sensor - emitter separation

For a high degree of collimation Fig.4.20 would have been a straight line but the technique used for the results presented in this thesis only partially collimates the beam (Fig.4.21). Fig.4.21 also shows that the smallest value that can be obtained for ' d ' is 3cm (2.5cm + 0.5cm).

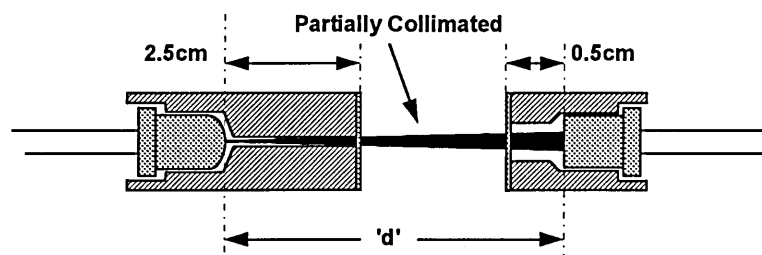


Fig.4.21 Optical sensor - emitter separation ' d '

Attenuation of a collimated light beam as it passes through a medium over a known distance can be described as:

$$\ln(V_a) = \ln(V_o) - \alpha_a d_a \quad \{17\}$$

Where V_a is the voltage detected by the sensor for a finite distance 'd' and V_o is the voltage detected by the sensor when $d = 0$ for a medium having an attenuation constant of α . Consequently α_a , the value for 'air', is the negative gradient of the graph in Fig.4.20 (when approximated to a straight line) where:

$$\alpha_a = -\text{gradient} = \left\langle \frac{0.693 - 1.46}{9 - 3} \right\rangle = 0.128 \text{ cm}^{-1} \quad \{18\}$$

This experiment was repeated for water and the results plotted in Fig.4.22 allowing the gradient ' α_w ' to be calculated:

$$\alpha_w = -\text{gradient} = \left\langle \frac{-0.466 - 1.46}{9 - 3} \right\rangle = 0.321 \text{ cm}^{-1} \quad \{19\}$$

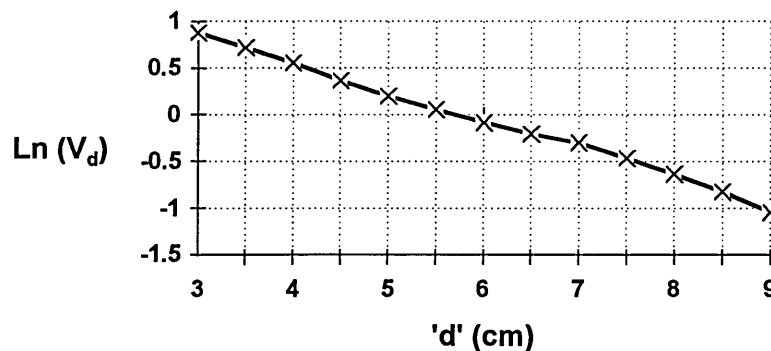


Fig.4.22 Attenuation in 'WATER' as a function of sensor - emitter separation

In a practical situation, for example inside a sewer, there will be a constant separation 'd' but a varying liquid level.

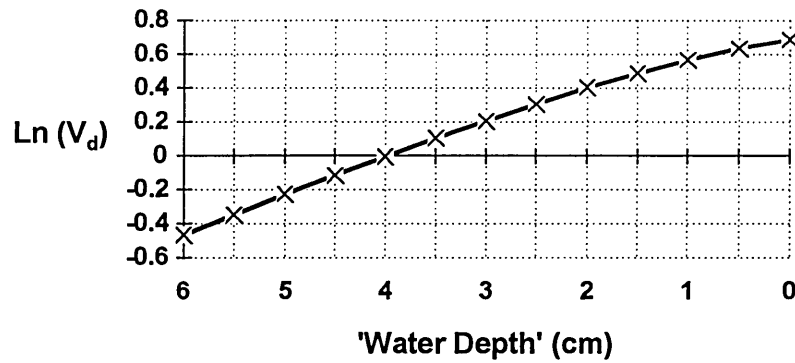


Fig.4.23 Variable water depth for separation, $d=9\text{cm}$

Fig.4.23 presents results for $d=9\text{cm}$, the effective diameter of the sewer, when the water depth is varied between 6cm (the maximum possible with the equipment used) and 0cm. When no water is present the sensor voltage is three times the magnitude of readings when the whole space between sensor and emitter is filled with water.

4.3.2 AIR BUBBLES IN WATER

A potentially important component of any liquid based flow is gas in bubble form which, from modelling presented earlier in this chapter, exhibits complex behaviour. In order to verify this modelling work and gain further information, these effects were investigated experimentally. The main problem when making measurements involving air bubbles in water is the difficulty involved in controlling the experiment.

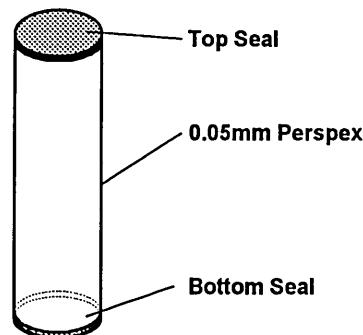


Fig.4.24 Bubble constructed from 0.05mm flexible perspex

To simplify this 'pseudo' bubbles were constructed using 0.05mm thick flexible perspex sheet rolled into tubes and the ends sealed (Fig.4.24).

This section presents two sets of results, both obtained using the 8x8 sensor and detector pairs described in section 4.2. The optical transducers were mounted on the 8cm diameter pipe and the bubble was constructed to have a diameter of 2cm. The optical system produces collimated light pencils of approximately 3mm diameter which are 1cm apart. The complete system, when constructed was initially calibrated in air. Fig.4.25 (a) shows a side elevation and Fig.4.25 (b) a plan view of the experiment using the 'pseudo' bubble.

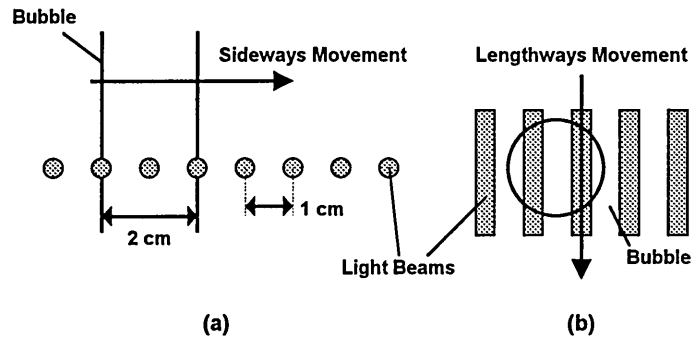


Fig.4.25 (a) Sideways movement (b) Lengthways movement

Fig.4.26 presents the results obtained from one sensor/emitter pair for the bubble moving sideways through the light pencil.

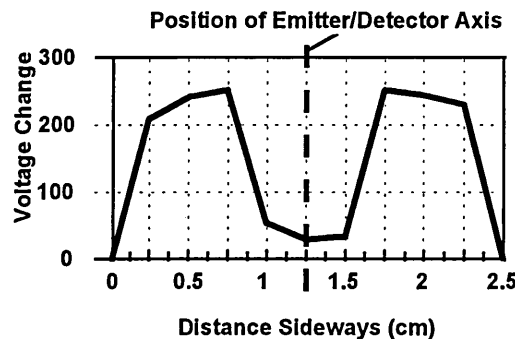


Fig.4.26 Voltage readings for sideways movement

The first reading, for a sideways distance of 0cm, represents the bubble before it enters the light pencil's path and by the 2.5cm mark it has passed through completely. Attenuation occurs initially due to reflection and refraction as the edge of the bubble begins to intercept the light pencil however, when the bubble is positioned centrally along the emitter/detector axis (Fig.4.26) it is mainly unattenuated. If this experiment is repeated for a bubble moving along the emitter/detector axis of the light pencil (Fig.4.25 (b)) the graph illustrated in Fig.4.27 results. In this case the distances marked are those between the sensor and the bubble centre. The measured light intensity is a function of distance from the bubble to the sensor and this relationship appears to be non-linear.

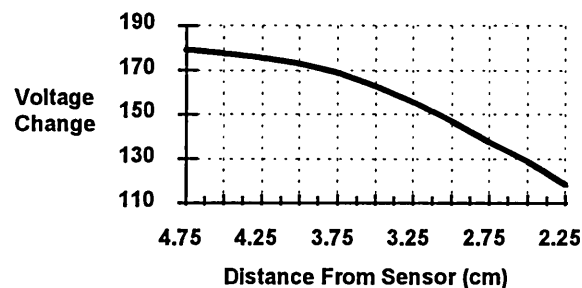


Fig.4.27 Voltage readings for lengthways movement

4.3.3 VARIABLE DEPTH LIQUIDS IN PIPES

This section presents analytical results for liquids in horizontal pipes, where the depth varies. Section 4.1.1 dealt with the effect that a variable depth liquid has on the overall attenuation of a light beam and section 4.1.4 outlined the effect of refraction at a liquid/gas interface on a light pencil for various angles of incidence. Both of these phenomena have relevance for optical tomography hardware that is to be implemented in a variable depth liquid based flow.

When three or more projections are required one of these will produce an angle of incidence (θ_i) at the liquid surface of between 0 and 90 degrees depending on the systems design (Fig.4.28).

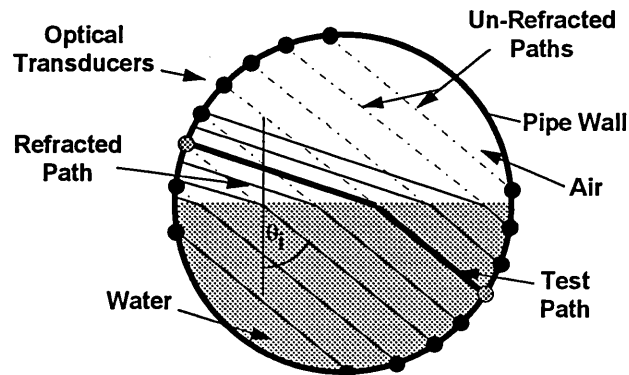


Fig.4.28 Refraction due to an acute angle of incidence θ_i

Identical hardware was used to that in section 4.3.2, with results presented for the central sensor/emitter pair, highlighted on Fig.4.28. For this experiment the phantom was sealed at the top using a clear perspex plug and positioned horizontally. It was then filled to a depth of 4cm (50%), through a hole drilled at one end, and rotated anticlockwise to simulate various angles of incidence (θ_i). The results of detected voltage (V_d) vs' θ_i are illustrated in Fig.4.29 over the range 0° to 14° (for θ_i), as angles of incidence greater than this produced no response at the sensor.

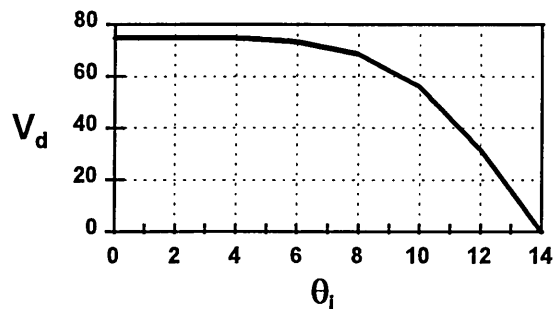


Fig.4.29 Optical sensor voltage (V_d) versus θ_i

4.3.4 IMAGE RECONSTRUCTIONS FOR FIVE SAMPLES

This section presents image reconstructions, using the back projection method outlined in chapter 2, for five physically different substances of 2cm diameter.

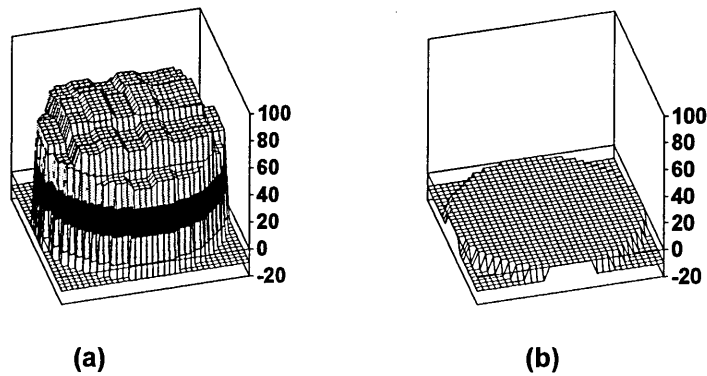


Fig.4.30 Calibrations for (a) water and (b) air.

Fig.4.30 illustrates two image reconstructions, the first is for transducers calibrated in water when only air is present (a) and the second is for transducers calibrated in air when only water is present in the phantom (b). In each graph the vertical axis represents, in relative terms, the optical attenuation at a particular location on the phantom cross-section (the x-y axis). For the purposes of this experiment the system was calibrated in air. Fig.4.31 illustrates the labelling of material positions used when looking at a plan view of the pipe.

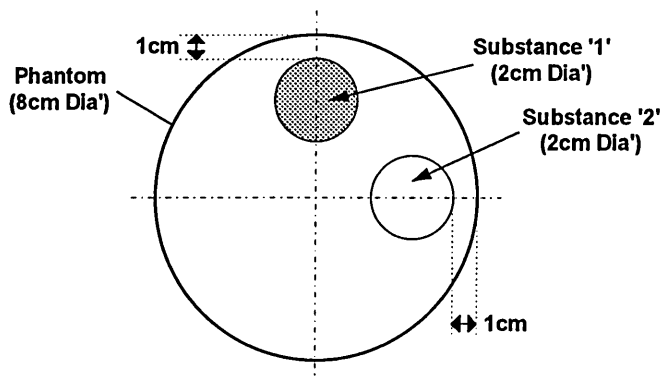


Fig.4.31 Positioning of substances

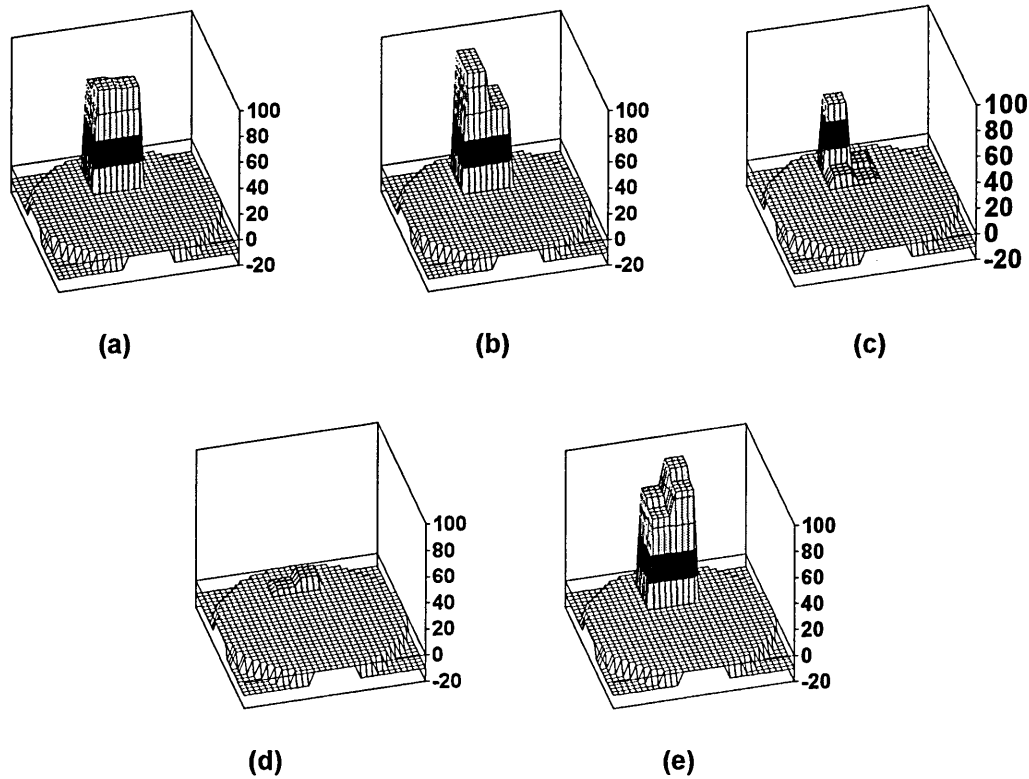


Fig.4.32 Image reconstructions for: (a) Paper tube, (b) Plastic tube, (c) Bubble, (d) Perspex bar, (e) Rubber tube

Fig.4.32 presents the resulting image reconstructions for: (a) Paper tube; (b) Plastic tube; (c) Bubble; (d) Perspex bar and (e) Rubber tube.

4.3.5 IMAGE RECONSTRUCTIONS FOR MULTIPLE SUBSTANCES

This section presents image reconstructions for three combinations of two substances, to test the resulting image contrast (Fig.4.33). The combinations used were: (a) Paper (position '1') and perspex (position '2'); (b) Rubber (position '1') and perspex (position '2') and (c) Rubber (position '1') and paper (position '2'). Fig.4.31 illustrates positions '1' and '2' within the phantom.

Because the system design presented earlier in this chapter only uses two optical projections the image reconstructions shown in Fig.4.33 are the result of superimposing reconstructions obtained for each material in isolation. The

reason for this is that reconstructions for multiple substances using optical tomography require more than two projections (chapter 2).

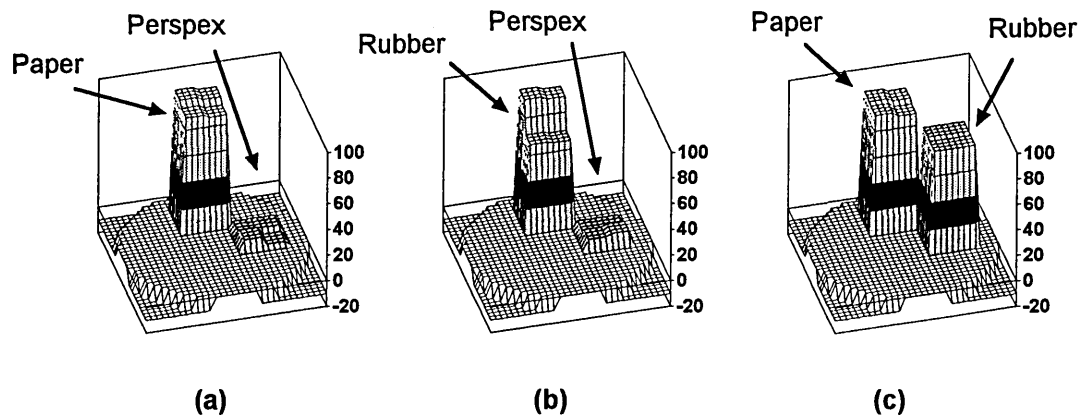


Fig.4.33 Image reconstructions for: (a) paper and perspex (b) rubber and perspex (c) rubber and paper

The results presented in Fig.4.33 illustrate that opaque substances such as paper and rubber produce approximately 100% attenuation and that clear substances such as perspex produce less than 20% attenuation of the sensor/emitter light pencils.

4.3.6 CONCLUSIONS FROM MEASURED RESULTS

Section 4.2 determined the optical attenuation constants of water and air and also investigated how optical attenuation is affected when the proportions of water and air between the sensor and emitter vary. Fig.4.26 shows a graph of received light intensity for a single sensor/emitter pair as a simulated bubble passes across the light path. The results illustrate that total internal reflection occurs when the light path connects with the edge of the bubble and that the beam is largely unattenuated when passing through the bubble centre. This agrees well with modelling presented in section 4.1.

Fig.4.27 presents results for a bubble moving along a light pencil, when slightly offset from its centre. Again, the light intensity attenuation due to divergence matches the modelling results presented in section 4.1.3. Fig.4.29 presents measured light intensity results for a single sensor/emitter pair when a light pencil passes through a water/air boundary for a range of angles of incidence. These results match the modelling carried out in section 4.1.4.

Fig.4.32 presents image reconstructions of acquired data for five different substances. From these it is apparent that paper, plastic and rubber are easily detected, as the samples used were all opaque. Clear perspex appeared largely invisible to the reconstruction algorithm and bubbles are only detected when light is significantly refracted or caused to diverge, as explained by the modelling of section 4.1.

Finally, Fig.4.33 introduces reconstructions for selected substance pairings. When perspex and paper are imaged together only paper is visible; when perspex and rubber are together only the rubber is visible and when rubber and paper are placed in the phantom together they are both equally detectable.

From the results presented in this chapter it can be seen that the simulated bubbles attenuate the incident light pencils more than the background water. Theoretically, air attenuates light less than water but as simulated bubbles were used a water/perspex/air interface is produced rather than a water/air interface. This may account for any discrepancy, as may the physical size of the simulated bubble (2cm diameter) which, when used in conjunction with light pencils of 2mm diameter (section 4.2.1) may cause refraction.

CHAPTER 5

DUAL MODALITY TOMOGRAPHY

Chapters 3 and 4 present hardware designed to implement both optical and electrical resistance tomography in conjunction with modelling and physical results relating to both. This chapter will present aspects of hardware design detailing a combination of both modalities and discuss the implications of such a process. Also included are results of single/dual modality analysis relating to five materials:

1. Paper
2. Plastic
3. Bubbles
4. Clear Perspex
5. Rubber

When saturated with the conveying liquid, paper acquires a very similar resistivity making it virtually undetectable to resistance tomography. However, this saturation will not grossly affect its opaque optical properties. Plastic has a high resistivity making it detectable by resistance tomography and being opaque it can also be detected by optical tomography. Bubbles have a high resistivity but optical properties that are difficult to define which complicates optical image reconstruction. Clear perspex has a high resistivity but similar optical properties to water (saline solution) and rubber is detectable by both resistance and optical tomography as it is highly resistive but transmits no light (if totally opaque).

Testing these materials illustrates the advantages of a dual modality system in situations where multi-component flows are diverse and not easily resolved by

a single tomographic technique. Reconstructions are presented for each material using each modality in isolation and also combining both. This illustrates improvements in system performance that can be achieved between single and dual modality technologies.

5.1 DUAL MODALITY CONFIGURATION

The hardware used for dual modality readings is identical to that described separately in chapters 3 and 4 but with both modalities' sensors mounted in the same section of pipe. Ideally, both the optical and electrical resistance sensors should be positioned in the same two dimensional plane however, they are actually slightly offset, as illustrated in Fig.5.1 (a).

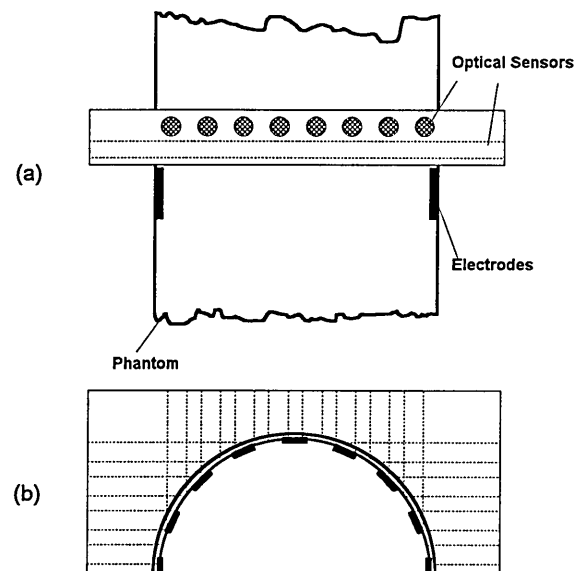


Fig.5.1 Combination of sensors for two modalities

Fig.5.1 (b) shows how both sets of sensors are superimposed using a plan view. Because a flow will move suspended solids through both sets of sensors in sequence, measurements on a moving liquid will require some form of timing to ensure that both sets of data refer to the same two dimensional section. For

measurements made on a static phantom this is not a problem as objects of sufficient length to span both sets of transducers are used.

5.2 DUAL MODALITY RESULTS

Investigations are described using the dual modality hardware outlined in section 5.1 and reconstruction software described in chapter 2. Initially, the methods used to combine reconstructed images for both optical and electrical resistance modalities are discussed and then results are presented for each of these using a combination of materials. Fig.5.2 illustrates the labelling convention used when positioning materials in the phantom.

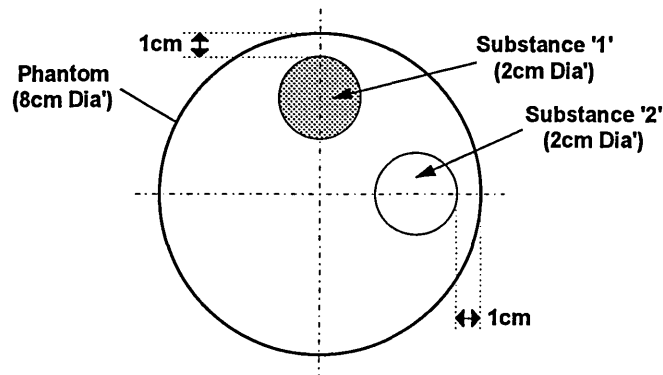


Fig.5.2 Position of substances (Plan view)

5.2.1 DUAL MODALITY IMAGE COMBINATION TECHNIQUES

Paper and clear perspex are used to demonstrate several approaches used to produce dual modality image reconstructions. Results presented in chapters 3 and 4 illustrate the difficulties experienced by electrical resistance tomography in detecting saturated paper and by optical tomography in detecting perspex. A saline solution with a background conductivity of 11 mS; an oscillator frequency of 8 kHz and an injection current of 5 mA are used. To allow comparison the

paper (substance '1') and perspex (substance '2') cylinders are placed in the test phantom in the positions shown in Fig.5.2.

The optical and electrical resistance tomography software written for this project (Appendix 4) allows image reconstructions to be saved to disk in a tab delimited text format. The dual modality image reconstructions presented in this chapter are the result of manipulations performed on individual optical and electrical resistance tomograms by the spreadsheet package Excel [32]. This approach was used because most of the data had already been imported into Excel to produce the three dimensional images presented in chapters 3 and 4.

Possible 'data fusion' techniques include:

- (a) Superimposing the primary images using an 'averaging' function
- (b) Using a software based test function to select one of the original images using criteria such as contrast etc.
- (c) Combining both using a 'logical' function to choose the highest contrast on a pixel by pixel basis.

Results for each of these approaches are presented in un-filtered and filtered formats. For the filtered results a threshold filter is used which establishes the threshold value as the average non-zero pixel value. In this way any spurious data can be removed from the image reconstructions producing an improved contrast at an object's border.

5.2.1.1 Averaging Functions

An averaging function, within Excel, was applied to corresponding pixel pairs for both the 32x32 optical and EIT image arrays producing a combined 32x32

dual modality array. Both of the initial arrays contain percentage values relating to the relative electrical and optical properties at individual pixel locations and therefore the final array also has values in the range 0-100%. The averaging function sums each optical and electrical image matrix at individual pixel locations, and divides the result by two, as described by equation {1}.

$$D_{n,m} = \sum_{n,m} \frac{[O_{n,m} + E_{n,m}]}{2} \quad \{1\}$$

Where $O_{n/m}$ and $E_{n/m}$ are the individual pixel values of the optical and electrical reconstruction arrays at row n , column m and $D_{n/m}$ is the value produced for the dual modality array. Fig.5.3 (a) shows results for an un-filtered image and Fig.5.3 (b) shows the corresponding filtered results where the threshold value is computed to be 40%.

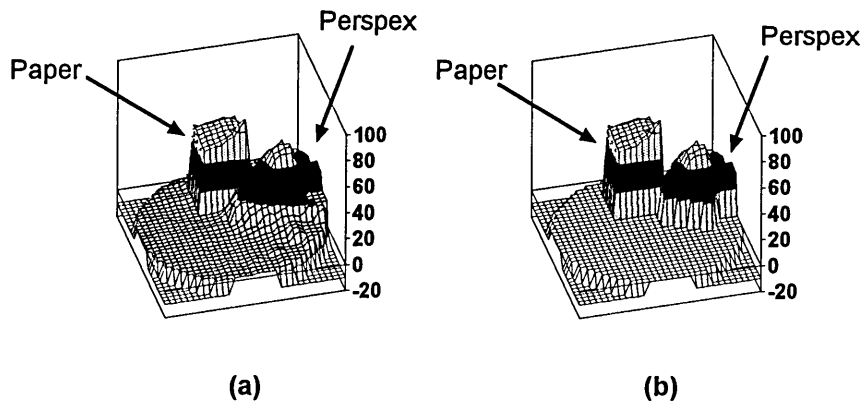


Fig.5.3 Dual modality image reconstructions using an averaging function

5.2.1.2 Criteria Based Decision Function

The design of this technique depends on the type of reconstruction acceptable to the user. One approach would be to choose either of the single modality

reconstructions depending on which has the highest contrast. Fig.5.4 (a) illustrates an electrical resistance reconstruction and Fig.5.4 (b) an optical reconstruction for the objects shown in Fig.5.2. From this, it is not apparent which of the two images should be chosen, as neither fully describes both the paper and perspex discontinuities, although Fig.5.4 (b) does identify the position of both. Therefore assuming that Fig.5.4 (b) is the most useful image then a technique for deciding this mathematically is required. This must be applied after both reconstructions are performed, otherwise improvements and alterations in the individual reconstruction algorithms used may invalidate the choice. This topic will be discussed further in chapter 7.

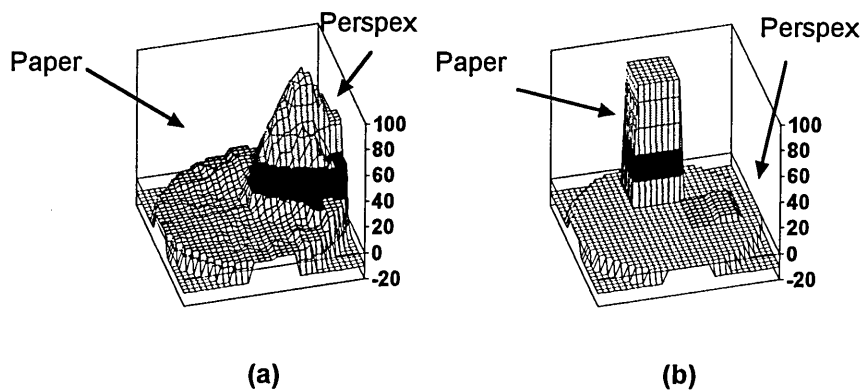


Fig.5.4 Image reconstructions using (a) ERT (b) Optical tomography

5.2.1.3 Logical Combination Function

The 'logical combination' function is a variation of the 'criteria based decision' function described in section 5.2.1.2, but the decision is made at a pixel level rather than a whole image level. In the case of Fig.5.4 choosing either of the images (a) or (b) will result in the loss of data. The following function implements such an approach:

$$\begin{aligned} D_{n,m} &= O_{n,m} & (O_{n,m} > E_{n,m}) \\ D_{n,m} &= E_{n,m} & (O_{n,m} \leq E_{n,m}) \end{aligned} \quad \{2\}$$

Where $O_{n/m}$ and $E_{n/m}$ are the individual pixel values of the 32x32 optical and EIT image reconstruction arrays at row n , column m and $D_{n/m}$ is the value produced for the dual modality array. Therefore if array position $n=3$, $m=5$ is used this function can be rewritten as equation {3}.

$$\begin{aligned} D_{3,5} &= O_{3,5} & (O_{3,5} > E_{3,5}) \\ D_{3,5} &= E_{3,5} & (O_{3,5} \leq E_{3,5}) \end{aligned} \quad \{3\}$$

This function {3} chooses the highest of the two original array components to be placed in the dual modality array. Fig.5.5 (a) shows an un-filtered image using this method and Fig.5.5 (b) shows the corresponding filtered image where the threshold computes to 70%.

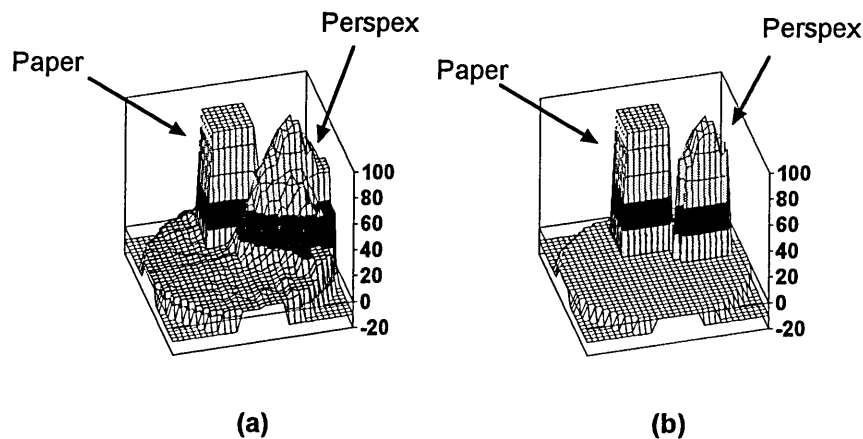


Fig.5.5 Dual modality image reconstructions using a logical combination function

5.2.2 IMAGE RECONSTRUCTIONS FOR FIVE SAMPLES

Using the logical combination function described in section 5.2.1.3 dual modality image reconstructions for five different materials are presented in Fig.5.6. Each sample is the same size and they are all placed in position '1' of

Fig.5.2. The threshold values that compute for each sample shown in Fig.5.6

are:

paper = 60% plastic = 70%
 bubble = 50% perspex = 35%
 rubber = 70%.

The electrical resistance tomography data used to produce each of the dual modality images is scaled (in % units) relative to the highest pixel value (100%) computed for all five substances, as outlined in chapter 3. This approach is utilised because the back projection algorithm used (chapter 2) produces results that represent changes in resistivity rather than absolute values.

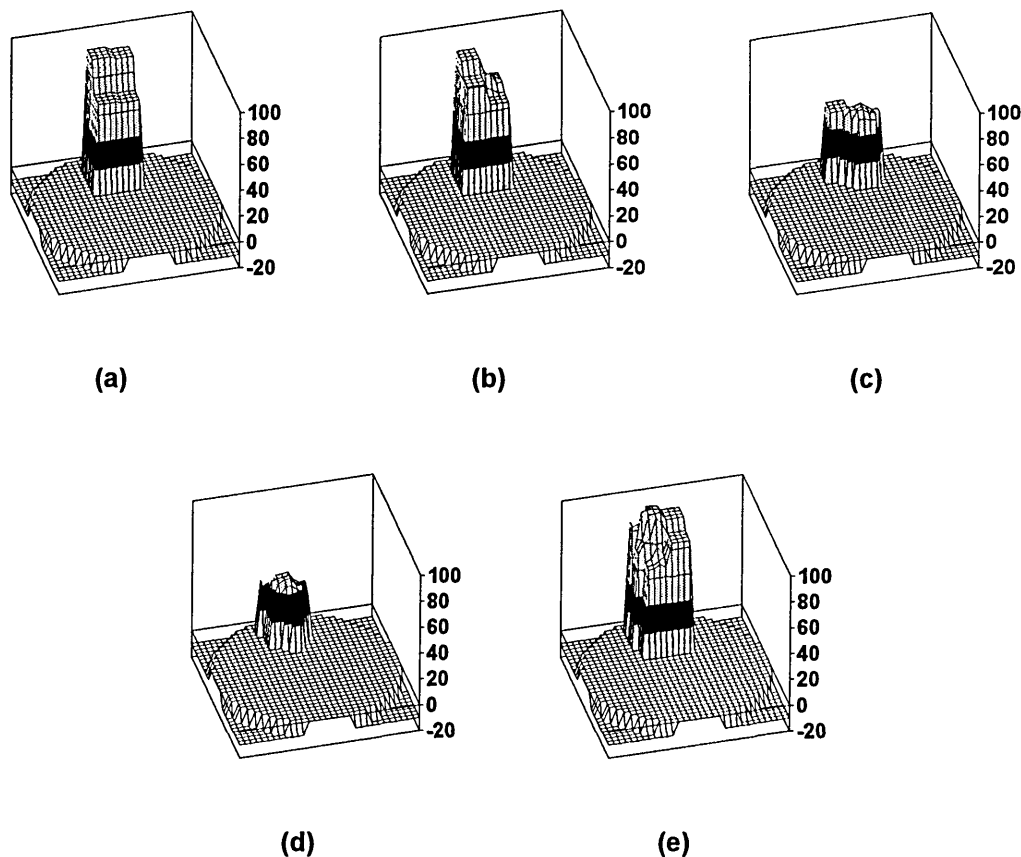


Fig.5.6 Image reconstructions using the 'logical combination function' for:
 (a) Paper Tube (b) Plastic Tube (c) Bubble (d) Perspex Rod (e) Rubber Tube

5.2.3 IMAGE RECONSTRUCTIONS OF MULTIPLE SUBSTANCES

This section presents image reconstructions for more than one substance placed in the phantom at a time. This poses an extremely non-linear problem for the EIT image reconstruction algorithm used, due to the wide range of resistivities, and consequently only combinations of two substances are presented in order to minimise image overlapping. Both substances are positioned as illustrated in Fig.5.2 and the 'logical combination function' is used to produce a dual modality image. Fig.5.7 shows results for perspex (position '2') and paper (position '1'). Fig.5.7(a) is a filtered image and Fig.5.7 (b) is unfiltered.

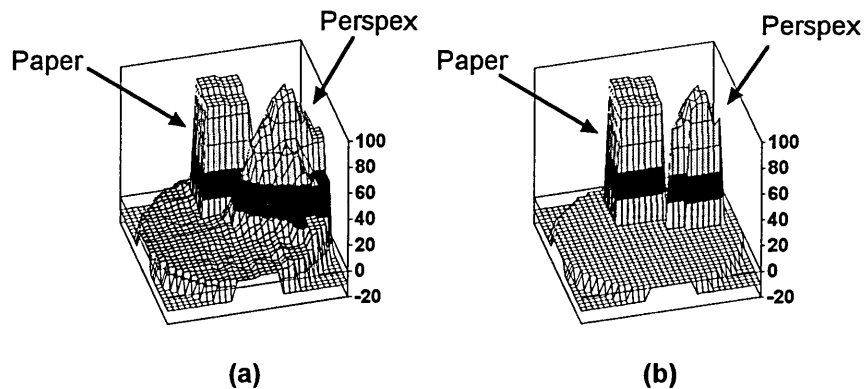


Fig.5.7 Perspex and paper reconstructions, (a) un-filtered (b) filtered

When this is repeated for rubber (position '1') and perspex (position '2') Fig.5.8 (a) and (b) are the resulting images.

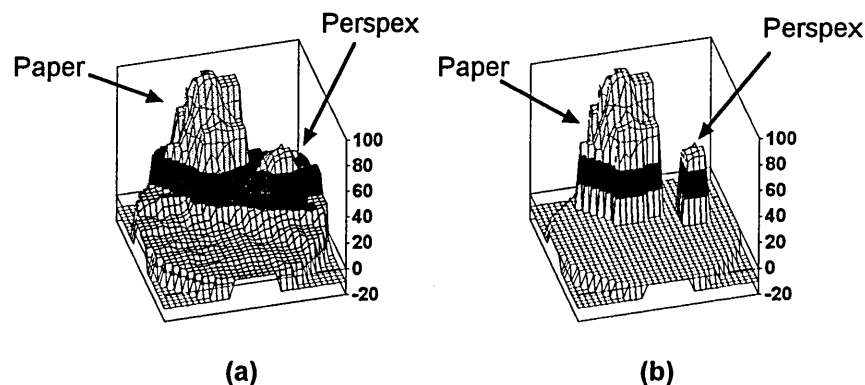


Fig.5.8 Rubber and perspex reconstructions, (a) un-filtered (b) filtered

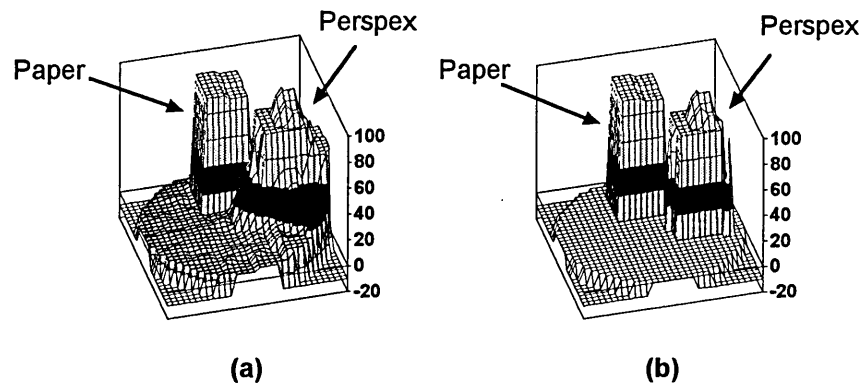


Fig.5.9 Paper and rubber reconstructions, (a) un-filtered (b) filtered

Finally results for paper (position '1') and rubber (position '2') are presented in Fig.5.9.

5.3 CONCLUSIONS

Three methods of combining single modality data to produce a dual modality tomogram have been demonstrated in conjunction with one filtering technique. The 'averaging' function produces an image similar in shape to the logical combination function, however the averaging function Fig.5.3 results in a degraded 'compromise' image. Averaging images for a substance hardly visible to one modality, but highly visible to the other produces a dual modality tomogram which is a compromise between the images produced by the two modalities in isolation.

The 'criteria based decision' function is useful when only a single material is being monitored at a time as the most appropriate image for one substance (for a particular modality) may not be the best for the other and the dominant substance overrides the other. When more than one substance is present one option for this method could be to display both 'single modality' images side by side.

The logical combination method in conjunction with some form of filtering is the most effective (Fig5.6, Fig.5.7, Fig.5.8 and Fig.5.9), although it may introduce complications if the individual substances have to be identified. This problem may be overcome if each of the substances has a unique set of characteristics. For example, rubber is highly visible to both optical and electrical modalities while perspex and paper are only visible to one. It would be possible to incorporate a subroutine within the system software to utilise this knowledge and decide what each material is. Consequently, if prior knowledge of a multi-component flow were available then dual modality tomography, using some form of 'logical combination' reconstruction algorithm, would be capable of flow component identification. If multiple sensor sets were used in conjunction with some form of cross correlation, velocity profile information could also be synthesised.

CHAPTER 6

CONCLUSIONS AND FUTURE WORK

This chapter consists of two parts. Firstly, general conclusions are presented resulting from work outlined in chapters 2 to 5. This is followed by a discussion of possible options for future work. The nature of the project undertaken covers two areas of tomography and consequently a large amount of design was required to produce both systems before a unified dual modality system could be produced. As a result many ideas for future work have emerged.

6.1 CONCLUSIONS

Chapters 2 to 5 present conclusions for electrical resistance, optical and dual modality tomography modelled and acquired data. This section will summarise these and comment on progress made towards achieving the project aims outlined in section 1.4 of chapter 1.

6.1.1 DEVELOPMENT OF MODELS FOR THE OPTICAL AND ELECTRICAL MODALITIES (AIM '1')

Chapter 3 (sections 3.1.1 to 3.1.6) presents theory and results of modelling for the electrical resistance tomography modality. Conclusions for these are drawn in section 3.1.7. Chapter 4 (sections 4.1.1 to 4.1.4) presents corresponding results for the optical modality with conclusions presented in section 4.1.5. Consequently, two and three dimensional models have been developed for the electrical resistance modality and the attenuation, refraction, reflection and divergent properties of light at liquid/air interfaces were also successfully modelled for the optical tomography modality.

6.1.2 DEVELOPMENT OF HARDWARE FOR THE OPTICAL AND ELECTRICAL RESISTANCE MODALITIES (AIM '2')

Chapter 3 (sections 3.2.1 to 3.2.9) outlines the hardware developed for the electrical resistance modality and chapter 4 (sections 4.2.1 to 4.2.7) presents corresponding information for the optical modality. This hardware was constructed and successfully tested using a static phantom and used to produce the measurement data presented in chapters 3, 4 and 5.

6.1.3 THE COMBINATION OF SENSORS FOR BOTH MODALITIES ON THE SAME SECTION OF PIPE (AIM '3')

Chapter 5, section 5.1 describes how sensors for the two modalities of electrical resistance and optical tomography were mounted on the same section of pipe. Section 5.2 presents results gained using this configuration and therefore dual modality hardware was successfully developed and employed to produce measured data.

6.1.4 THE DEVELOPMENT OF WINDOWS BASED SOFTWARE FOR IMAGE RECONSTRUCTION AND DATA ACQUISITION (AIM '4')

Chapter 2 describes software developed, using the Windows programming environment, to control the hardware presented in chapters 3, 4 and 5. This software implements a back projection algorithm (chapter 2) to produce image reconstructions for both modalities. Consequently, aim '4' was achieved in full.

6.1.5 THE COMPARISON OF MEASURED AND MODELLED DATA (AIM '5')

Chapters 3 and 4 present results for modelled and measured electrical and optical tomography data. The validity of the modelling approaches used, with reference to measured results, is examined below using an example from

chapter 3 (electrical resistance tomography) and chapter 4 (optical tomography).

6.1.5.1 Electrical Resistance Tomography

Fig.3.14 and Fig.3.15, of chapter 3, show image reconstructions using the three dimensional HSPIICE model configured to simulate an object 'flowing' toward the electrode plane for two different radial positions. These results suggest that an object's radial position, with respect to the pipe's centre, influences the image reconstruction algorithm. This is confirmed by measured results, as illustrated in Fig.3.35, which suggests that positions closest to the phantom wall produce the highest absolute measured electrode voltage disturbance, but positions closest to the centre are more sensitive (relative to the electrode plane image) to objects further from the electrode plane.

6.1.5.2 Optical Tomography

Fig.4.6 of chapter 4 illustrates the modelled displacement (α) of a light pencil due to a changing angle of incidence (θ_i) at a water air boundary. This indicates that α increases as a function of θ_i . If a sensor were to be positioned at the initial point of aim of the light pencil (in Fig.4.6) then its output would reduce as θ_i increases. Fig.4.29 illustrates the results of an experiment to test this and clearly shows the modelled prediction to be accurate. Consequently, these examples demonstrate the validity of each modelling approach used. Chapters 3 and 4 provide a complete set of results and individual conclusions.

6.1.6 DEVELOPMENT OF IMAGE COMBINATION TECHNIQUES TO PRODUCE DUAL MODALITY IMAGES (AIM '6')

Chapter 5, section 5.2.1 introduces three possible image combination techniques capable of producing dual modality tomograms from the individual images produced by the electrical resistance and optical modalities. The Logical Combination Function was selected for incorporation into the final Windows based dual modality software. Consequently, the original single modality software was upgraded to produce dual modality images resulting in the development of a complete dual modality system.

6.1.7 DETERMINING THE ADVANTAGES OF A DUAL MODALITY APPROACH (AIM '7')

To determine whether the dual modality system described in this thesis produces benefits over individual single modality approaches two sets of measurements were made for the electrical resistance, optical and dual modality configurations. These first produced image reconstructions for five physically different substances (paper, opaque plastic, bubbles, clear perspex and opaque rubber) and the second used selected combinations of these (perspex/paper; perspex/rubber and rubber/paper). The relevant sections are: chapter 3 (sections 3.3.3 and 3.3.4); chapter 4 (sections 4.3.4 and 4.3.5) and chapter 5 (sections 5.2.1 and 5.2.2). The results of these tests for each modality are discussed below.

6.1.7.1 Electrical Resistance Tomography Results

Fig.3.36 of chapter 3 presents image reconstructions for the five individual substances using the electrical resistance modality. These show a good image contrast for plastic and rubber and illustrate that bubbles and perspex are also

detected. However, these results also indicate that electrical methods are incapable of detecting fibrous materials (such as paper) which, when saturated, assume a resistivity that is similar to the surrounding liquid. Fig.37 presents image reconstructions for the three substance pairings. In each of these three tomograms the substance with the highest resistivity tends to overwhelm its pair. Only in the case of the perspex/rubber combination is it obvious that two substances are present in the tomogram, as both have very high resistivities.

6.1.7.2 Optical Tomography Results

Fig.4.32 of chapter 4 presents tomograms for the five materials. Here again the plastic and rubber tubing produces a good contrast as they are both opaque. Paper and bubbles are also detectable but clear perspex produces a similar response to that produced by paper for the electrical resistance images. Fig.4.33 presents the image reconstructions for the three substance pairings. For Fig.4.33 (a) and (b) the opaque substances (paper and rubber) dominate and only in Fig.4.33 (c) where two opaque materials are used is it possible to clearly identify two objects.

6.1.7.3 Dual Modality Results

Fig.5.6 of chapter 5 presents the dual modality image reconstructions using the logical combination function for the five individual substances. In each of the five tomograms of Fig.5.6 a high image contrast is produced. For the three substance pairings (Fig.5.7 - Fig.5.9) two object positions are clearly visible.

Consequently it can be concluded that the original aims of the research project were achieved. Also, there are advantages in using a dual modality approach

when no single modality is capable of detecting all materials present in multi-component flows.

6.2 FUTURE WORK

Suggestions presented here for future work fall into four main categories: hardware design, software development, mathematical modelling and investigative experimentation.

Electrical resistance tomography (ERT) hardware can be broken down into four main areas: sensor design, hardware control, signal conditioning, and data acquisition. The first section presented below deals with improvements in the data acquisition hardware, followed by sections on sensor design, software development and further mathematical modelling work.

6.2.1 FASTER DATA ACQUISITION

The ultimate purpose of any process tomography system is to provide measurement data on component flow rates. Section 3.3.5, of chapter 3, presents formulae to describe how far an object moves when travelling at a specific velocity for a given data acquisition time. Fig.39 illustrates this graphically and shows that for a flow velocity of 1ms^{-1} and using the data acquisition hardware described in chapter 3 an object would move 8cm during data acquisition. This would be unacceptable for small objects and consequently fast data acquisition systems are important for certain applications. This section suggests ways of improving the data acquisition time of the hardware presented in chapters 3, 4 and 5.

6.2.1.1 Improved Data Acquisition Technology

The WIN/30D data acquisition board [1], with a sampling rate of 1MHz (for a single channel) and 16 configurable input channels, should be considered. When all 16 channels are in use it acquires data at a rate of 62.5kHz per channel, allowing a full set of 16 readings to be made in 25 μ s. Using the opposite method of current injection, described in chapter 3, an EIT system with 16 electrodes could acquire a full set of data in approximately 130 μ s. This is more than five times faster than the system presented in chapter 3 but presents a relatively high cost at £1000. The WIN/30D is capable of Direct Memory Access (DMA) which allows data to be transferred to a personal computer's memory at a rate of 900k words per second, which is independent of the computer's central processor. Consequently, image reconstruction could be implemented at the same time as data is being transferred, producing further time savings.

6.2.1.2 Direct Wave Sampling (ERT)

The limiting factor when designing a fast Electrical Resistance Tomography (ERT) system using r.m.s./d.c. converters is their settling time. Consequently, methods of eliminating the rectification process should be investigated. One example is the approach of Grootvelt et. al. [24] who presents results for a general EIT system that does not require any form of voltage rectification, but more can be done.

Firstly, after the electrode potentials are buffered and amplified they could be sampled using a very fast 16 channel data acquisition card, such as that suggested in section 6.2.1.1. Timing problems can be simplified by using a

voltage controlled oscillator that produces a trigger pulse connected directly to the data acquisition card to initiate operation.

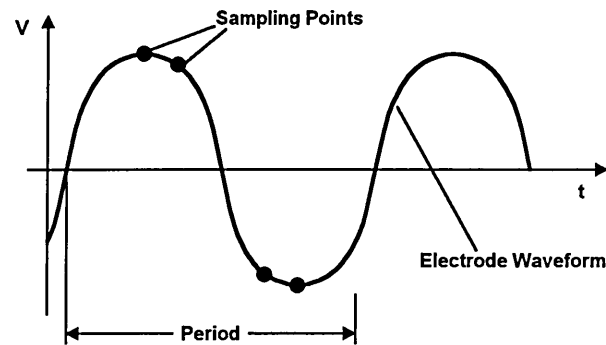


Fig.6.1 Four sampling points per cycle for a 20kHz wave form

The trigger pulse is set to occur when the oscillator is at a peak producing a single voltage reading. Using this technique, a full set of 96 readings would take approximately 4.8ms (for an oscillator frequency of 20kHz). This time could be further reduced if the voltage wave-form were more efficiently sampled, for example making readings at points other than the oscillator voltage amplitude peaks and troughs (Fig.6.1).

Finally, another possibility would be to use a sample and hold circuit at the input to the data acquisition channels to sample the peak voltage of all the electrode wave forms. Both of these final approaches introduce further complexity into the circuit design and may introduce errors due to noise when sampling very small voltages.

6.2.1.3 Switched d.c. Operation (ERT)

A more radical approach is to use d.c. voltages. There are two main reasons for using a.c. voltages in electrical tomography designs: firstly, to prevent electrolysis when using liquid solutions and secondly, to allow both phase and

magnitude data to be extracted from the sampled electrode voltages. The hardware presented in this thesis, for Electrical Resistance Tomography (ERT), utilises only magnitude information and if a short d.c. pulse were used, of the type illustrated in Fig.6.2, then electrolysis could be prevented as the overall d.c. component of this waveform is zero. Fig.6.2 illustrates the result of connecting a 100kHz square wave to opposite electrodes of a 10cm radius, circular phantom (containing a 11mS saline solution) via a constant current source and measuring the voltage at separate electrodes.

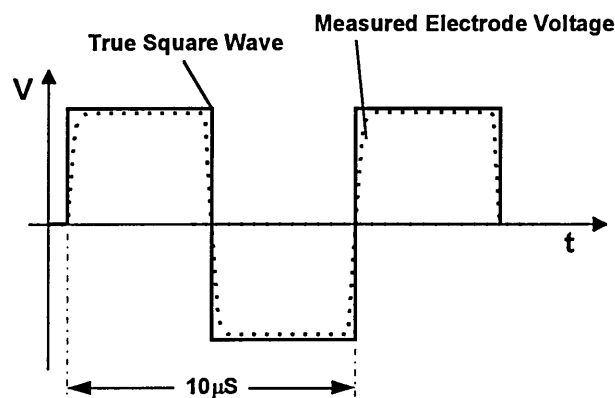


Fig.6.2 Measured 5 μ s voltage pulse compared to a 'true' square wave

The measured result (perforated line) was a waveform with a short rise time (less than 1 μ s) followed by a shorter fall time (approximately 0.5 μ s).

Consequently, if such a d.c. voltage were used to replace the usual sinewave source in an ERT design there would be a rise time delay of 1 μ s before the electrode voltages could be sampled. For hardware such as the WIN-30/D, introduced in section 6.2.1.1, data acquisition would take approximately 16 μ s for 16 electrodes and utilising eight unique projections (opposite current injection) a total acquisition time of 140 μ s would result. Allowing 20-40 μ s for digital logic propagation delays elsewhere in the system this would allow an

ERT design, based on this concept, to acquired over 2000 sets of data per second. If this were the case then flows of 2m/s could be interrogated with a measurement length of 1mm (Section 6.2.1).

6.2.2 ELECTRICAL RESISTANCE TOMOGRAPHY SENSORS

An important area of electrical tomography system development is that of electrode design and positioning. Electrical Resistance Tomography (ERT) interrogates a three dimensional space and subsequent reconstruction algorithms approximate the resulting data to two dimensions. For process flows this will produce problems (Section 6.1) as objects outside the two dimensional electrode plane will interfere with image reconstructions, under certain conditions. Outlined below are some approaches that may reduce or overcome this problem along with other electrode improvement possibilities.

6.2.2.1 *Electrode Length*

With Electrical Resistance Tomography the electrodes are the physical means by which an electric field is induced in a phantom or pipe. For this reason an investigation into the effect of varying electrode lengths may be beneficial . A large electrode length, relative to the pipe diameter, may confine most of the electric field to the measurement section, Fig.6.3. However, a relatively large volume of the conveyor will be interrogated.

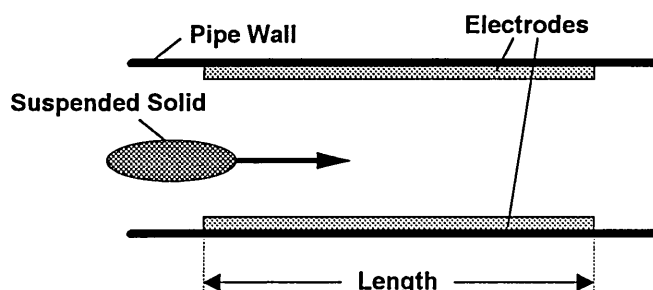


Fig.6.3 The use of longer electrodes

An alternative approach is to use end guard electrodes as used in capacitance methods, to prevent current from flowing away from the measurement section. Also, if the guard electrodes are wide compared with the injection electrode the result may be very significant in obtaining a two dimensional measurement.

6.2.2.2 Compound Electrodes

Hau et. al. [25] use a compound electrode design to improve the sensitivity of an EIT system. Chapter 3, section 3.2 introduces this concept which allows all electrodes to be used for data acquisition, as separate electrodes are used for current injection and voltage measurement. It may be useful to investigate whether any other benefits would result from this approach, such as an improved image reconstruction resolution due to the increased number of voltage measurements per current injection position. The main drawback of compound electrodes is that the same cable cannot be used by the current injection and voltage measurement electrodes, further complicating the design and increasing construction costs.

6.2.2.3 Multi-Layer Electrode Configurations

An alternative method of reducing the three dimensional effect may be to use it positively. Ilyas et. al. [27] describe a multi-plane impedance tomography design utilising four sets of sixteen electrodes positioned at different positions along a mixing vessel. The information derived from these four electrode planes is used to construct a pseudo three dimensional image of the processes.

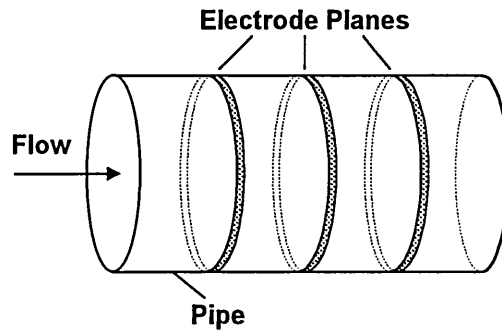


Fig.6.4 A multi-plane electrode configuration

One possibility with suspended solid flows may be to use three sets of sensors along the pipe, Fig.6.4. In this way weighted images from the left and right hand electrode planes could be combined with the central image to produce a more accurate two dimensional representation. The mechanism for achieving this combination of images would require investigation, and it may be possible to combine the data at a voltage level to minimise the computational overheads. Also, this type of electrode architecture would provide the opportunity for cross-correlation to be implemented to produce velocity information.

6.2.2.4 Alternative Electrode Numbers

Image resolution may be improved by the use of more electrodes in a single plane. 16 electrodes restrict the image resolution to some finite value which, for pipes of a relatively large diameter, may not be adequate. Using 32 electrodes would produce improvements in image resolution which would have to be offset against increased circuit complexity and software overheads. A 16 electrode system employing polar current injection requires a minimum of 96 voltage readings before repetition occurs while a 32 electrode design requires 448.

6.2.3 OPTICAL TOMOGRAPHY SENSORS

The optical tomography hardware presented in this thesis uses only two projections of eight views. This would not be adequate for a practical design due to aliasing effects. Also, LEDs were chosen as a source due to their low cost and adequate light intensities for the diameter of pipe used in chapter 4. When designing a system that uses optical tomography methods then the choice of correct light source is essential in order that acceptable light intensities reach the sensors. Outlined below are suggestions for improvements that can be made to the optical tomography system described in chapter 4.

6.2.3.1 Increased Views and Projections

Dugdale [16] designed an optical tomographic system to image two component gas/liquid flows and describes the limiting factor (with respect to the maximum number of optical views that can be used per projection) as their physical size. The typical diameter of a pin photodiode package, Fig.6.5 (a) is 6mm restricting the number that can be used per projection, Fig.6.5 (b) to:

$$AX = \frac{d}{\text{dia}} = \frac{d}{6\text{mm}} \quad \{1\}$$

where 'd' and 'dia' are the pipe diameter and LED diameters respectively. One approach to solving this problem is currently being investigated by the process tomography group at Sheffield Hallam University and uses optical fibres to couple transmitters and receivers to the pipe [38].

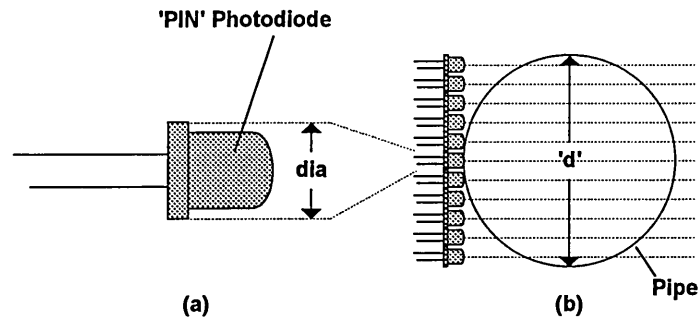


Fig.6.5 Maximum resolution limitation

Due to the relatively small diameter of modern optical fibres this allows many more views per projection than the approach illustrated in Fig.6.5 (b).

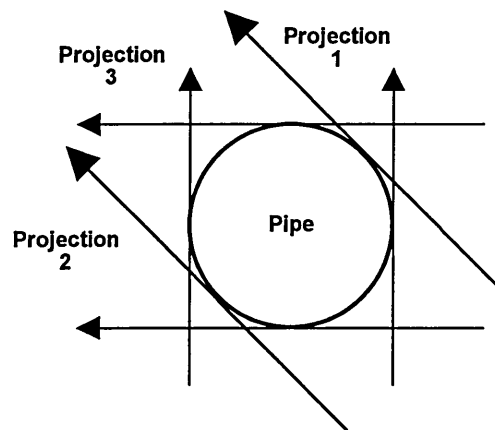


Fig.6.6 A three projection optical arrangement

The main drawbacks of using optical fibres include complexities associated with coupling light sources and detectors to the fibre and also the problem of collimating light emerging from a fibre. The main benefit is that greatly enhanced resolutions become possible allowing much better images to be reconstructed than those presented in chapters 4 and 5.

Another method of improving optical resolution and reducing the aliasing effects, documented by Dugdale [16], is the use of more projections (Fig.6.6).

Using more than two projections introduces the problem of how to mount the

transducers in the same two dimensional plane. It is possible to use two or more transducer planes but these would have to be offset by a minimum distance of 6mm, along the flow axis, using the current LEDs. Therefore, an investigation into the consequences of axial displacement is required.

6.2.3.2 Other Light Sources

A light source with a superior specification to a high intensity LED is the laser diode. A typical device, the SLD1131VS [43], can be obtained for approximately £23 which is ten times more expensive than an average LED. The SLD1131VS has an optical output power of 6mW, an operating wavelength of 670nm and a response time of less than 5ns, making it ideal for high speed data acquisition. This particular device operates in a single longitudinal mode and is extremely stable over a wide temperature range. The light emitted has a radiation angle of approximately 10° (Fig.6.7 (a)) and therefore some form of collimation is required which is simplified by the devices' high coherence. Another feature of this device is an internal PIN photodiode with an external connection (Fig.6.7(b)) and this can be used to monitor optical power output, allowing calibration to be performed automatically.

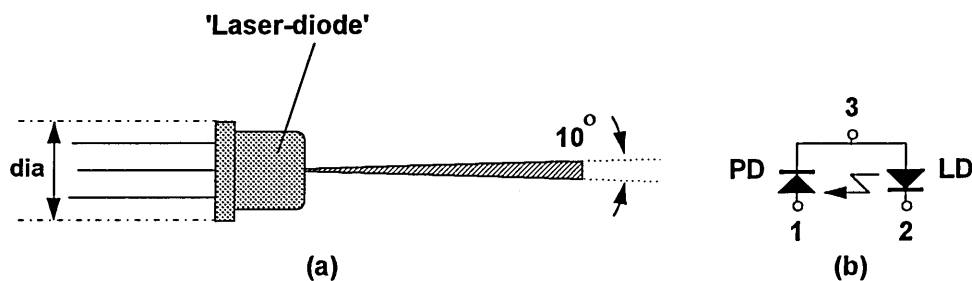


Fig.6.7 A laser diode - (a) Beam Divergence (b) Electrical connections

In an industrial environment where accuracy and ease of calibration is important then a system using laser diodes may be necessary and therefore further investigation in this area would be beneficial.

6.2.3.3 Alternative Light Frequencies

Saeed [39] demonstrated that infra-red light frequencies produce better transmission results through oil, water and gas mixtures. The LEDs outlined in chapter 4 operate at a peak frequency of 880nm which produces 'red' light. For future applications it would be useful to conduct an investigation into the optical transmission properties of the conveying medium over a wide range of source frequencies to determine an optimum value.

6.2.4 FURTHER MATHEMATICAL MODELLING

The mathematical modelling presented in chapters 3 and 4 of this thesis was carried out as part of a study into the use of optical and electrical resistance tomography for the monitoring of multi-component flows. There remains further scope for the development of these models. This is especially true when designing high resolution systems where component costs are high, as preliminary modelling may highlight problems that were not initially obvious. This section of the thesis presents ideas for further modelling work and improvements of existing techniques.

6.2.4.1 An Improved HSPICE Model

HSPICE was chosen as a modelling tool for electrical resistance tomography because of its ease of use and availability. It is possible to construct large three dimensional models in HSPICE to represent the complex impedance bounded by the measurement electrodes. One problem with HSPICE is the

user interface since to describe a circuit, only two options are available: a textual description or a graphical interface. Both methods present their own limitations when describing three dimensional component meshes: textual descriptions become complex and difficult to interpret at a later date and using a graphical interface circuit descriptions in three dimensions are extremely difficult. One solution to this would be to write software that produces the initial HSPICE listing, allowing the user to choose from a variety of options:

1. Shape of pipe and size
2. Number of electrodes
3. Resolution required (number of nodes)
4. Position, size and electrical properties of any impedance discontinuity
5. Source frequency, frequency sweeps etc.
6. Definition of noise sources
7. Format of output etc.

A graphical package using EIT terminology could produce an optimised HSPICE input listing and it would also be possible to embed the HSPICE software within this package, and allow the user to choose an image reconstruction algorithm that would use the HSPICE output file as its reference.

6.2.4.2 Optical Modelling Software Development

The optical modelling work carried out in chapter 4 did not use any form of computational analysis. One possible use for any mathematical model is the production of data which can be used to test a reconstruction algorithm. This would be particularly useful for a dual modality design when experimenting with

methods of data combination. Section 6.2.4.1 outlines the possibilities for impedance modelling and although optical methods are commercially available they are usually designed for specific applications and are therefore expensive. It would be possible to write a basic software based optical modelling system and therefore further investigation in this area may be useful.

6.2.5 OTHER POSSIBILITIES FOR FUTURE WORK

The following sections describe further ideas for future work.

6.2.5.1 Timing Between Modalities

The dual modality hardware presented in this thesis needs to be developed further before flow monitoring can be implemented. An area requiring attention is the timing between the sensor sets of each modality. Section 6.2.3.1 illustrated the difficulties involved in mounting all the sensor sets on the same two dimensional plane. The hardware in chapter 5, takes an alternative approach and positions the sensors from each modality on different planes. To do this and avoid sampling different flow positions with each modality would require an accurate method of co-ordinating both sets of data acquisition hardware. This would have to take into account changes in flow velocity and consequently further investigation of this problem is required.

6.2.5.2 Improved Image Reconstruction and Alternatives

Chapter 2 introduced the concept of image reconstruction and described the back-projection algorithm used to produce tomograms for this thesis. Yorkey et. al. [55] outline the possible methods of image reconstruction and conclude that the most accurate approach is the modified Newton Raphson algorithm,

which requires an iterative solution. Therefore any future development may benefit from investigating iterative methods of image reconstruction.

One consideration that may also be useful is whether image reconstructions are actually required and whether some other form of flow identification may be possible. This may take the form of a statistical analysis of electrode and optical sensor voltages or some form of neural network flow recognition. Image reconstructions alone do not provide information about volume flow rates but do require large amounts of computation.

6.2.5.4 Flow Modelling and Environmental Monitoring

There are many applications that would benefit from a dual modality tomographic approach and two suggestions are described here. First is the environmental monitoring of gross solids for combined sewer overflows. A water research council publication [48] outlines a method by which this is currently achieved. In operation storm sewage is pumped into a viewing cell and images are recorded on tape Fig.6.8. Analysis consists of manually counting the number of objects that pass the window per minute. This system would benefit from some form of automation and a dual modality tomography system with a relatively low resolution may be capable of performing this task.

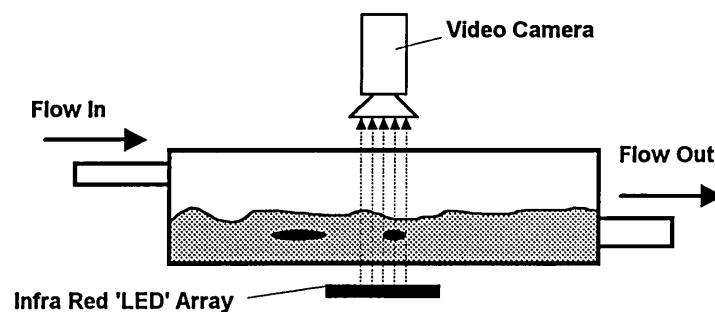


Fig.6.8 WRc gross solids monitor

A second possibility for dual modality tomography is in the design and analysis of sewage systems [47, 2]. Often, sewage component behaviours have to be modelled in order to improve a system's efficiency and, at present, there are few ways of verifying the results with measured data. Methods of sampling sewage flows do exist [45] but irrespective of their accuracy they provide little information regarding velocity and lateral drift of individual sewage components. To achieve this a flow has to be sampled without being disturbed, making tomographic techniques suitable. One specific application could be the investigation of 'sewage rake' efficiency. These rakes are used to remove gross solids from sewage flows, are empirically designed and tend to have low efficiencies. New designs could be investigated using an upstream and downstream dual tomography system with high speed data capture. In this way different designs could be analysed quickly.

REFERENCES

1. Amplicon Liveline summer 1994 catalogue, p84
2. Balmforth D J, 1991, "Model testing of the park road storm sewage overflow", Report on behalf of Calderdale Metropolitan Borough Council, Department of Civil Engineering, Sheffield Hallam University
3. Bamford (Instruments) LTD, "Series 2000 electronic 'smart' flowmeter", Company literature, F Bamford (Instruments) LTD, Stockport
4. Barber D C, Brown B H and Freeston I L, 1983, "Imaging spatial distributions of resistivity using applied potential tomography", *Electron. Lett.*, 19, p933-5
5. Barber D C and Brown B H, 1987, "Fast reconstruction of resistive images", *Clin.Phys.Physiol.Meas*, 8 (Suppl A), p47-54
6. Beck M S, Green R G and Thorn R, 1987, "Non-intrusive measurement of solids mass flow in pneumatic conveying", *J.Phys.E. E:Sci.Instrum.*, Vol. 20, p835-40
7. Beck M.S. et al, "Flow imaging for the complete characterisation and measurement of multi-component flows", *Trans.Inst. Measurement Control*, April - June 1987, vol. 9, no.2, p113-122
8. Bidin A R, Green R G and Shackleton M E, 1992, "A prototype electrodynamic imaging system for pneumatic conveyors", *First Meeting of the European Concerted Action on Process Tomography*, 26-29 March, Manchester, p60-73
9. Bidin A R, Green R G, Shackleton M E, Stott A L and Taylor R W, 1993, "Process tomography using electrodynamic sensors", *Process Tomography - A strategy for industrial exploitation*, Karlsruhe, 25-27 March, p229-32
10. Blickley G J, April 1991, "Mass flow measurement aided by Coriolis methods", *Control Engineering*, p53-6

11. Bolomey J C, Joachimowicz N and Pichot C, 1993, "Microwave imaging techniques for non-destructive testing of industrial materials: from projections to tomography", *Process Tomography - A strategy for industrial exploitation*, Karlsruhe, 25-27 March, p233-7
12. Brant M R, Yang W Q and Beck M S, 1993, "Safety aspects in instrument design - explosive hazards", *Process Tomography - A strategy for industrial exploitation*, Karlsruhe, 25-27 March, p316-21
13. Breckon W R, Paulson K S, Pidcock M K, 1991, "Parallelism in EIT, in information processing in medical imaging", *Edited by: Ortendahl D A and Lacer J, Wiley-Liss*, p187-96
14. Curtis E, Thaddeus E, Morrow J, 1989, "Calculating resistors in a network", *IEEE Engineering in Medicine & Biology Society*, 1989, Images of the 21st century, Vol. 9 (Part 2/6), p451-2
15. Dines K A, Lytle R J, July 1981, "Analysis of electrical conductivity imaging", *Geophysics*, Vol. 46, No. 7, p1025-36
16. Dugdale W P, 1994, "An optical instrumentation system for the imaging of two component flow", *PhD thesis, Bolton Institute*
17. Dugdale W P, Green R G, Hartley A J, Jackson R G, Landauro J, 1994, "Characterisation of single bubbles by an optical tomographic system", *Process Tomography - A strategy for industrial exploitation*, Norway, p229-32
18. Furness, A R, 1989, "Fluid flow measurement", *Longman, ISBN: 0-582-03165-6*
19. Gadd R, Record P, Rolfe P, 1992, "A sensitivity region reconstruction algorithm using adjacent drive current injection strategy", *Clin.Phys.Physiol.Meas.*, 13 (Suppl A), p101-5
20. Garaets J J and Borst J C, 1987, "A capacitance sensor for two phase void fraction measurement and flow pattern recognition", *Int.J. Multiphase Flow*, Vol. 14, No. 3, p305-20

21. Geselowitz D B, 1971, "An application of electrocardiographic lead theory to impedance plethsmography", *IEEE Trans.Biomed.Eng.*, BME-18, p38-41
22. Govier G W and Aziz K, 1970, "The flow of complex mixtures in pipes", *Robert Krieger*
23. Griffiths H, 1988, "A phantom for electrical impedance tomography", *Clin.Phys.Physiol.Meas*, Vol. 9 (Suppl A), p5-14
24. Grootveld C J, van Weert G and Scarlett B, 1993, "Concentration profiles measurement using EIT", *Process Tomography - A strategy for industrial exploitation*, Karlsruhe, 25-27 March, p335-7
25. Hua P, Eung J W, Webster J G Tompkins W J, "An electrical impedance tomograph using compound electrodes", *IEEE Engineering in Medicine & Biology Society*, 1989, Images of the 21st century, Vol. 9 (Part 2/6), p472-3
26. Huang S M, Plaskowski A B, Xie C G and Beck M S, 1989, "Tomographic imaging of two-component flow using capacitance sensors", *J.Phys.E:Sci.Instrum.*, Vol. 22, p173-7
27. Ilyas O M, Williams R A, Mann R, Ying P, Rushton A and Edwards R B, 1993, "Investigation of batch mixing using multi-plane impedance tomography", *Process Tomography - A strategy for industrial exploitation*, Karlsruhe, 25-27 March, p316-21
28. Kim Y and Woo H W, 1987, "A prototype system and reconstruction algorithms for the electrical impedance technique in medical body imaging", *Clin.Phys.Physiol.Meas.*, Vol. 8, Suppl. A, p63-70
29. King J D and Rollowitz W L, 1983, "Magnetic resonance measurement of flowing coal", *ISA Trans.*, Vol. 22, p69-76
30. MAXIM, 1992, "New releases data book"
31. Microsoft Corporation, Windows users guide (3.1), 1990 - 1992
32. Microsoft Corporation, Microsoft Excel users guide (Ver. 4), 1991

33. Microsoft Corporation, Microsoft Visual C++ (Manuals), 1994
34. Murphy D and Rolfe P, "Aspects of instrumentation design for impedance imaging", *Clin.Phys.Physiol.Meas.*, 1988, Vol. 9 (Suppl. A), p5-14
35. Mylroi M G and Calvert G, 1986, "Measurement and instrumentation for control", *Peter Peregrinus, ISBN: 0-86341-024-3*
36. Nowicki. D. J., Webster. J. G., "A one op-amp current source for electrical impedance tomography", *IEEE Engineering in Medicine and Biology Society*, 11th International Conference, 1989, p457-8
37. Parr A, 1991, "Hydraulics and Pneumatics, a Technician's and Engineer's guide", *Newnes, ISBN: 0-7506-0015-2*
38. Ruzairie M F, 1995, "Ph.D. conversion report", *Department of EIT, Sheffield Hallam University*
39. Saeed N, 1987, "Two component flow measurement using digital processing of optical signals", *MSc Thesis, CNA A*
40. Saeed N, Browne M A, Green R G and Martin P, 16-21 October 1988, "Two component flow regime identification and imaging with optical sensors", *IMEKO XI, Houston Texas*
41. Siemens, 1993, "Optoelectronics data book"
42. Smith R W M, Brown B H, Freeston I L and McArdle F J, 1991, "Real-time electrical impedance imaging", *Trans.Inst.MC.*, Vol. 13, No. 3, p125-8
43. Sony Optical Devices Data Book, Sony Electronics, 1994
44. Southern P W and Deloughry, 1993, "Imaging of oil/gas/water/sand interface levels in an oil separation vessel", *Process Tomography - A strategy for industrial exploitation, Karlsruhe, 25-27 March*, p335-37
45. Walsh A M, 1990, "The gross solids sampler - development of a sampler for combined sewer overflows", *WRc Internal Report, WRc, Swindon*

46. Wang M, Dickin F J and Williams R A, 1994, "Electrical resistance tomography of metal walled vessels and pipelines", *Electronics Letters*, 12 May, Vol. 30, No. 10, p771-3.
47. Wardle J, 1980, "Development work in vortex sewage separation", Internal report, Department of Civil Engineering, Sheffield Hallam University
48. Water Research Council Internal Report, "An Investigation into Applying Ultrasonic Techniques to Gross Solids Monitoring in Combined Sewer Outflows", *Water Research Council*, UM1171, November, 1990.
49. Webster J G (Editor), "Electrical impedance tomography", *Adam Hilger*, 1990
50. Wexler A, Fry B and Neuman M R, 1985, "Impedance computed tomography algorithm and system", *Appl. Opt.*, 24, p3985-92
51. Xie C G, Stott A L, Huang S M, Plaskowski A and Beck M S, 1989, "Mass flow measurement of solids using electrodynamic and capacitance sensors", *J.Phys., E:Sci.Instrum.*, Vol. 22, p712-9
52. Xu L A, Green R G, Plaskowski A and Beck M S, 1988, "The pulsed ultrasonic cross-correlation flometer for two phase flow measurement", *J.Phys., E:Sci.Instrum.*, Vol.21, p406-14
53. Yang W Q and Stott A L, 1992, "Low value capacitance measurements for process tomography", First Meeting of the European Concerted Action on Process Tomography, 26-29 March, Manchester, p60-73
54. Yorkey T J, Webster J G and Tompkins W J, 1986, "An optimal impedance tomographic reconstruction algorithm", *Proceedings of the 8th annual conference, IEEE Eng.Med.biol.soc.*, p339-42
55. Yorkey T J, Webster J G, 1987, "A comparison of impedance tomographic reconstruction algorithms", *Clin.Phys.Physiol.Meas*, 8 (Suppl. A), p55-62
56. Yu Z Z, Peyton A J and Beck M S, 1993, "A feasibility study of Electromagnetic Tomography", *Process Tomography - A strategy for industrial exploitation, Karlsruhe*, 25-27 March, p218-21

LIST OF APPENDIXES

TITLE	PAGE
40 Channel Digital I/O Port and 'Backplane'	A1
SPICE Listing for the 2 Dimensional Impedance Model	A3
SPICE Listing for the 3 Dimensional Impedance Model	A10
Dual Modality Tomography Software	A18
Publications	A51

APPENDIX 1

40 CHANNEL DIGITAL I/O PORT AND 'BACKPLANE'

All digital control signals required by system hardware are provided via an Arcom PCIB40, 40 channel digital I/O board, positioned in a spare expansion slot of an IBM compatible personal computer. It provides 40 TTL level lines which can be configured as either input or output using five 8-bit registers mapped into vacant bytes of the computer's memory. The first of the addresses sets a pointer to one of the 5 I/O ports or control registers on the I/O board (Table.A.1) and the second address allows an 8-bit read/write operation to be performed to/from the selected port/register. Also included on the Arcom board are 3 counters/timers, two test addresses and an output enable control, which has to be set to 255 to allow data to be written to the ports.

Pointer Value	Register Name	Read/Write	Comments
13	Control	W	Counter/Timer Control
12	CT2	R/W	Counter 2 Count
11	CT1	R/W	Counter 1 Count
10	CT0	R/W	Counter 0 Count
05-0F	Not used	-	-
04	G4	R/W	I/O Port 4
03	G3	R/W	I/O Port 3
02	G2	R/W	I/O Port 2
01	G1	R/W	I/O Port 1
00	G0	R/W	I/O Port 0
90	Output Enable	W	Enables Outputs of Certain Ports
81	Board Ident	R	Returns a Zero for PCIB40
80	User LED	W	'01' Switches Board LED on

Table.A.1 Pointer values for the 40 way digital I/O ports' register locations

Connections to the port are made via a 40 way D-type socket. On the hardware designed for this project the port is connected to a 'backplane', which has eight 62 way sockets for attachment of each circuit board. The

connections to the 62 way sockets (Table.A.1) fall into three areas. Firstly the 40 digital I/O lines have connections to 40 of the pins; secondly, the 16 electrical impedance electrode connections are required by three boards and this is achieved by passing them over via the 'backplane' board and finally the (+15V, 0V, -15V) and (0V, 5V) power supply rails occupy five spaces.

I/O	Pin	Connection	I/O	Pin	Connection
1	A1	D2 (OPT1/2) (EIT1/2)	2	B1	A2 (EIT1/2) (OPT2)
3	A2	D3 (OPT1/2) (EIT1/2)	4	B2	A1 (EIT1/2) (OPT2)
5	A3	D4 (OPT1/2) (EIT1/2)	6	B3	A0 (EIT1/2) (OPT2)
7	A4	D5 (OPT1/2) (EIT1/2)	8	B4	BIP (EIT1/2)
9	A5	D6 (OPT1/2) (EIT1/2)	10	B5	DIFF (EIT1/2)
11	A6	D7 (OPT1/2) (EIT1/2)	12	B6	N_BSY (EIT1/2)
13	A7	D8 (EIT1/2)	14	B7	-----
15	A8	D9 (EIT1/2)	16	B8	-----
17	A9	D10 (EIT1/2)	18	B9	N_WR (EIT1/2)
19	A10	D11 (EIT1/2)	20	B10	N_RD (EIT1/2)
21	A11	MODE (EIT1/2)	22	B11	HBEN (EIT1/2)
23	A12	CS(1) (EIT1/2)	♦	B12	CLKIN (OPT2) (EIT1/2)
24	A13	CS(2) (EIT1/2)	25	B13	D0 (OPT1/2) (EIT1/2)
26	A14	SPARE	27	B14	D1 (OPT1/2) (EIT1/2)
28	A15	SPARE	29	B15	N_RS (OPT1) (EIT1)
30	A16	N_BUSY (OPT2)	31	B16	N_WR_1 (EIT1)
32	A17	N_CS (OPT2)	33	B17	A3 (EIT1)
34	A18	N_CS (1) (OPT1)	35	B18	A2 (EIT1) (OPT1)
36	A19	N_CS (2) (OPT2)	37	B19	A1 (EIT1) (OPT1)
♦	A20	Electrode 10	39	B20	A0 (EIT1) (OPT1)
♦	A21	Electrode 9	40	B21	EN (EIT1)
♦	A22	Electrode 8	38	B22	N_WR_2 (EIT1)
♦	A23	Electrode 7	♦	B23	Electrode 16
♦	A24	Electrode 6	♦	B24	Electrode 15
♦	A25	Electrode 5	♦	B25	Electrode 14
♦	A26	Electrode 4	♦	B26	Electrode 13
♦	A27	Electrode 3	♦	B27	Electrode 12
♦	A28	Electrode 2	♦	B28	Electrode 11
♦	A29	Electrode 1	♦	B29	-15 V
♦	A30	+5 V	♦	B30	AGND
♦	A31	DGND	♦	B31	+15 V
♦	A32	Spare	♦	B32	Spare

Table.A.2 Connections to the 'backplane'

APPENDIX 2

SPICE LISTING FOR THE 2 DIMENSIONAL IMPEDANCE MODEL

* The initial cross-piece subcircuit

```
.SUBCKT BLOCK 1 2 3 4
R1 1 5 25
R2 2 5 25
R3 3 5 25
R4 4 5 25
.ENDS
```

* The insert cross-piece subcircuit

```
.SUBCKT INSBLOCK 1 2 3 4
R1 1 5 25
R2 2 5 25
R3 3 5 25
R4 4 5 25
.ENDS
```

* The cubed building block, 4 cross pieces

```
.SUBCKT CUBE 1 2 3 4 5 6 7 8
X1 1 9 12 8 BLOCK
X2 2 3 10 9 BLOCK
X3 10 4 5 11 BLOCK
X4 12 11 6 7 BLOCK
.ENDS
```

* The insert building block, 4 cross-pieces

```
.SUBCKT INSERT 1 2 3 4 5 6 7 8
X1 1 9 12 8 INSBLOCK
X2 2 3 10 9 INSBLOCK
X3 10 4 5 11 INSBLOCK
X4 12 11 6 7 INSBLOCK
.ENDS
```

* 2 building blocks in an oblong, for unusual shapes

```
.SUBCKT STRIP2 1 2 3 4 5 6
X1 1 2 7 6 BLOCK
X2 7 3 4 5 BLOCK
.ENDS
```

* 6 building blocks in an oblong, for unusual shapes

```
.SUBCKT STRIP6 1 2 3 4 5 6 7 8 9 10 11 12 13 14
X1 1 2 15 14 BLOCK
X2 15 3 16 13 BLOCK
X3 16 4 17 12 BLOCK
X4 17 5 18 11 BLOCK
X5 18 6 19 10 BLOCK
X6 19 7 8 9 BLOCK
.ENDS
```

* The listing. Firstly the cubes

```
XMOD1 31 32 13 8 2 1 7 12 CUBE
XMOD2 33 34 14 9 4 3 8 13 CUBE
XMOD3 35 36 15 10 6 5 9 14 CUBE
XMOD4 51 52 23 12 18 17 11 22 CUBE
XMOD5 53 54 27 16 20 19 15 26 CUBE
XMOD6 65 66 43 22 30 29 21 42 CUBE
XMOD7 67 68 45 24 32 31 23 44 CUBE
XMOD8 69 70 46 25 34 33 24 45 CUBE
XMOD9 71 72 47 26 36 35 25 46 CUBE
XMOD10 73 74 49 28 38 37 27 48 CUBE
XMOD11 87 88 58 44 52 51 43 57 CUBE
XMOD12 89 90 62 48 54 53 47 61 CUBE
XMOD13 103 104 77 57 66 65 56 76 CUBE
XMOD14 105 106 79 59 68 67 58 78 CUBE
XMOD15 107 108 80 60 70 69 59 79 CUBE
XMOD16 109 110 81 61 72 71 60 80 CUBE
XMOD17 111 112 83 63 74 73 62 82 CUBE
XMOD18 114 115 94 76 86 85 75 93 CUBE
XMOD19 116 117 96 78 88 87 77 95 CUBE
XMOD20 118 119 100 82 90 89 81 99 CUBE
XMOD21 120 121 102 84 92 91 83 101 CUBE
XMOD22 135 136 126 95 104 103 94 125 CUBE
XMOD23 137 138 128 97 106 105 96 127 CUBE
XMOD24 139 140 129 98 108 107 97 128 CUBE
XMOD25 141 142 130 99 110 109 98 129 CUBE
XMOD26 143 144 132 101 112 111 100 131 CUBE
XMOD27 157 158 147 125 115 114 124 146 CUBE
XMOD28 159 160 149 127 117 116 126 148 CUBE
```

XMOD29 161 162 153 131 119 118 130 152 CUBE
XMOD30 163 164 155 133 121 120 132 154 CUBE
XMOD31 177 178 168 148 136 135 147 167 CUBE
XMOD32 179 180 170 150 138 137 149 169 INSERT
XMOD33 181 182 171 151 140 139 150 170 INSERT
XMOD34 183 184 172 152 142 141 151 171 INSERT
XMOD35 185 186 174 154 144 143 153 173 CUBE
XMOD36 199 200 189 167 158 157 166 188 CUBE
XMOD37 201 202 191 169 160 159 168 190 CUBE
XMOD38 203 204 195 173 162 161 172 194 CUBE
XMOD39 205 206 197 175 164 163 174 196 CUBE
XMOD40 219 220 210 190 178 177 189 209 CUBE
XMOD41 221 222 212 192 180 179 191 211 INSERT
XMOD42 223 224 213 193 182 181 192 212 INSERT
XMOD43 225 226 214 194 184 183 193 213 INSERT
XMOD44 227 228 216 196 186 185 195 215 CUBE
XMOD45 241 242 231 209 200 199 208 230 CUBE
XMOD46 243 244 233 211 202 201 210 232 CUBE
XMOD47 245 246 237 215 204 203 214 236 CUBE
XMOD48 247 248 239 216 206 205 216 238 CUBE
XMOD49 261 262 253 232 220 219 231 252 CUBE
XMOD50 263 264 255 234 222 221 233 254 CUBE
XMOD51 265 266 256 235 224 223 234 255 CUBE
XMOD52 267 268 257 236 226 225 235 256 CUBE
XMOD53 269 270 259 238 228 227 237 258 CUBE
XMOD54 281 282 272 252 242 241 251 271 CUBE
XMOD55 283 284 274 254 244 243 253 273 CUBE
XMOD56 285 286 278 258 246 245 257 277 CUBE
XMOD57 287 288 280 260 248 247 259 279 CUBE
XMOD58 299 300 291 273 262 261 272 290 CUBE
XMOD59 301 302 293 275 264 263 274 292 CUBE
XMOD60 303 304 294 276 266 265 275 293 CUBE
XMOD61 305 306 295 277 268 267 276 294 CUBE
XMOD62 307 308 297 279 270 269 278 296 CUBE
XMOD63 320 321 312 292 284 283 291 311 CUBE
XMOD64 322 323 316 296 286 285 295 315 CUBE
XMOD65 333 334 326 311 300 299 310 325 CUBE
XMOD66 335 336 328 313 302 301 312 327 CUBE
XMOD67 337 338 329 314 304 303 313 328 CUBE
XMOD68 339 340 330 315 306 305 314 329 CUBE

XMOD69 341 342 332 317 308 307 316 331 CUBE
XMOD70 349 350 344 327 321 320 326 343 CUBE
XMOD71 351 352 348 331 323 322 330 347 CUBE
XMOD72 357 358 354 345 336 335 344 353 CUBE
XMOD73 359 360 355 346 338 337 345 354 CUBE
XMOD74 361 362 356 347 340 339 346 355 CUBE

* The 2x1 blocks

XMOD75 91 64 50 40 49 63 STRIP2
XMOD76 324 318 298 287 297 317 STRIP2
XMOD77 319 310 290 282 289 309 STRIP2
XMOD78 86 56 42 39 41 55 STRIP2

* The 6x1 blocks

XMOD79 250 240 218 198 176 156 134 122 133 155 175 197 216 239 STRIP6
XMOD80 249 230 208 188 166 146 124 113 123 145 165 187 207 229 STRIP6

* The low value resistors that provide the electrodes

RE1 3 4 1U
RE2 10 19 1U
RE3 28 40 1U
RE4 102 122 1U
RE5 176 198 1U
RE6 250 260 1U
RE7 324 332 1U
RE8 351 356 1U
RE9 359 360 1U
RE10 350 353 1U
RE11 319 325 1U
RE12 249 251 1U
RE13 165 187 1U
RE14 113 93 1U
RE15 39 21 1U
RE16 18 7 1U

* Resistors to compensate for single connections to a node

R1 7 1 142
R2 1 2 100
R3 2 3 100
R5 4 5 100

R6 5 6 100
R7 6 10 142
R9 19 20 100
R10 20 16 142
R11 16 37 142
R12 37 38 100
R13 38 28 142
R15 40 50 142
R16 50 64 100
R17 64 92 142
R18 92 84 142
R19 84 102 100
R21 122 134 142
R22 134 156 100
R23 156 176 100
R25 198 218 100
R26 218 240 100
R27 240 250 142
R29 260 280 100
R30 280 288 142
R31 288 298 142
R32 298 318 100
R33 318 324 142
R35 332 342 142
R36 342 341 100
R37 341 348 142
R38 348 352 142
R39 352 351 100
R41 356 362 142
R42 362 361 100
R43 361 360 100
R45 359 358 100
R46 358 357 100
R47 357 353 142
R49 350 349 100
R50 349 343 142
R51 343 334 142
R52 334 333 100
R53 333 325 142
R55 319 309 142

R56 309 289 100
R57 289 281 142
R58 281 271 142
R59 271 251 100
R61 249 229 142
R62 229 207 100
R63 207 187 100
R65 165 145 100
R66 145 123 100
R67 123 113 142
R69 93 75 100
R70 75 85 142
R71 85 55 142
R72 55 41 100
R73 41 39 142
R75 21 29 142
R76 29 30 100
R77 30 11 142
R78 11 17 142
R79 17 18 100

* Now for the resistors to connect the ZERO node to the correct electrode:

* These will not need to be duplicated in a 3D model.

RZERO1 0 187 100MEG
RZERO2 0 113 100MEG
RZERO3 0 39 100MEG
RZERO4 0 18 100MEG
RZERO5 0 3 100MEG
RZERO6 0 10 100MEG
RZERO7 0 28 100MEG
RZERO8 0 102 100MEG
RZERO9 0 176 100MEG
RZERO10 0 250 100MEG
RZERO11 0 324 100MEG
RZERO12 0 351 100MEG
RZERO13 0 360 100MEG
RZERO14 0 353 100MEG
RZERO15 0 325 100MEG
RZERO16 0 251 100MEG

* The Constant Current Sources:

```
ICON1  3 359 PULSE(0 5M 0 0.0001M 0.0001M 1.5M 50M)
ICON2  10 350 PULSE(0 5M 2M 0.0001M 0.0001M 1.5M 50M)
ICON3  28 319 PULSE(0 5M 4M 0.0001M 0.0001M 1.5M 50M)
ICON4  102 249 PULSE(0 5M 6M 0.0001M 0.0001M 1.5M 50M)
ICON5  176 165 PULSE(0 5M 8M 0.0001M 0.0001M 1.5M 50M)
ICON6  250 93 PULSE(0 5M 10M 0.0001M 0.0001M 1.5M 50M)
ICON7  324 21 PULSE(0 5M 12M 0.0001M 0.0001M 1.5M 50M)
ICON8  351 7 PULSE(0 5M 14M 0.0001M 0.0001M 1.5M 50M)
```

*CONTROL

```
.tran 2M 17M 1M
.print tran v(113,165) v(39,93) v(18,21) v(3,7) v(10,4)
.print tran v(28,19) v(102,40) v(176,122) v(250,198) v(324,260)
.print tran v(351,332) v(360,356) v(353,359) v(325,350) v(251,319)
.print tran v(187,249)
.END
```

APPENDIX 3

SPICE LISTING FOR THE 3 DIMENSIONAL IMPEDANCE MODEL

```
* Subcircuit 1
.SUBCKT UNIT1 1 2 3
R1 1 2 62.8
R2 2 3 102.85
R3 3 1 42.8
.ENDS
```

```
* Subcircuit 2
.SUBCKT UNIT2 1 2 3
R1 1 2 42.8
R2 2 3 62.8
R3 3 1 71.4
.ENDS
```

```
* Subcircuit 3
.SUBCKT UNIT3 1 2 3
R1 1 2 31.4
R2 2 3 91.4
R3 3 1 42.8
.ENDS
```

```
* Subcircuit 4
.SUBCKT UNIT4 1 2 3
R1 1 2 114.2
R2 2 3 31.4
R3 3 1 71.4
.ENDS
```

```
* Subcircuit 5
.SUBCKT UNIT5 1 2 3 4
R1 1 2 71.4
R2 2 3 71.4
R3 3 4 71.4
R4 4 1 71.4
R5 1 3 200
R6 2 4 200
.ENDS
```

```
* Subcircuit 6
.SUBCKT UNIT6 1 2 3
R1 1 2 50
R2 2 3 100
R3 3 1 71.4
.ENDS
```

```
* Insert subcircuit
.SUBCKT INS 1 2 3 4
R1 1 2 714
R2 2 3 714
R3 3 4 714
R4 4 1 714
R5 1 3 2000
R6 2 4 2000
.ENDS
```

* Vertical connector subcircuit

.SUBCKT HEIGHT 1 2

R1 1 2 100

.ENDS

* Vertical connector insert subcircuit

.SUBCKT HINS 1 2

R1 1 2 1000

.ENDS

* Connections to the electrode plane

XE1 37 34 32 33 UNIT5
XE2 38 35 17 34 UNIT5
XE3 41 37 33 36 UNIT5
XE4 42 38 34 37 UNIT5
XE5 43 39 35 38 UNIT5
XE6 45 41 36 40 UNIT5
XE7 46 42 37 41 INS
XE8 47 43 38 42 INS
XE9 48 44 39 43 UNIT5
XE10 49 45 40 29 UNIT5
XE11 50 46 41 45 INS
XE12 51 47 42 46 INS
XE13 52 48 43 47 INS
XE14 53 20 44 48 UNIT5
XE15 54 50 45 49 UNIT5
XE16 55 51 46 50 INS
XE17 56 52 47 51 INS
XE18 57 53 48 52 UNIT5
XE19 58 54 49 28 UNIT5
XE20 59 55 50 54 INS
XE21 60 56 51 55 INS
XE22 61 57 52 56 INS
XE23 62 21 53 57 UNIT5
XE24 63 59 54 58 UNIT5
XE25 64 60 55 59 INS
XE26 65 61 56 60 INS
XE27 66 62 57 61 UNIT5
XE28 67 64 59 63 UNIT5
XE29 68 65 60 64 UNIT5
XE30 69 66 61 65 UNIT5
XE31 25 68 64 67 UNIT5
XE32 24 69 65 68 UNIT5
XE34 34 1 32 UNIT6
XE35 34 1 17 UNIT6
XE52 53 5 20 UNIT6
XE54 53 5 21 UNIT6
XE71 68 9 25 UNIT6
XE72 68 9 24 UNIT6
XE51 49 13 29 UNIT6
XE53 49 13 28 UNIT6
XE42 39 18 3 UNIT1
XE44 39 19 3 UNIT1
XE64 66 23 7 UNIT1
XE62 66 22 7 UNIT1
XE61 63 27 11 UNIT1
XE63 63 26 11 UNIT1
XE43 36 30 15 UNIT1
XE41 36 31 15 UNIT1
XE46 44 19 39 UNIT2
XE40 35 18 39 UNIT2

XE60 62 22 66 UNIT2
XE66 69 23 66 UNIT2
XE59 58 27 63 UNIT2
XE65 67 26 63 UNIT2
XE45 40 30 36 UNIT2
XE39 33 31 36 UNIT2
XE48 44 4 19 UNIT3
XE38 35 2 18 UNIT3
XE58 62 6 22 UNIT3
XE68 69 8 23 UNIT3
XE67 67 10 26 UNIT3
XE57 58 12 27 UNIT3
XE47 40 14 30 UNIT3
XE37 33 16 31 UNIT3
XE36 17 2 35 UNIT4
XE50 20 4 44 UNIT4
XE56 21 6 62 UNIT4
XE70 24 8 69 UNIT4
XE69 25 10 67 UNIT4
XE55 28 12 58 UNIT4
XE49 29 14 40 UNIT4
XE33 32 16 33 UNIT4

* The resistors to connect the 'zero' node to the correct electrode:

RE1 0 1 100MEG
RE2 0 2 100MEG
RE3 0 3 100MEG
RE4 0 4 100MEG
RE5 0 5 100MEG
RE6 0 6 100MEG
RE7 0 7 100MEG
RE8 0 8 100MEG
RE9 0 9 100MEG
RE10 0 10 100MEG
RE11 0 11 100MEG
RE12 0 12 100MEG
RE13 0 13 100MEG
RE14 0 14 100MEG
RE15 0 15 100MEG
RE16 0 16 100MEG

* Connections to the upper plane(1)

XU1 137 134 132 133 UNIT5
XU2 138 135 117 134 UNIT5
XU3 141 137 133 136 UNIT5
XU4 142 138 134 137 UNIT5
XU5 143 139 135 138 UNIT5
XU6 145 141 136 140 UNIT5
XU7 146 142 137 141 UNIT5
XU8 147 143 138 142 UNIT5
XU9 148 144 139 143 UNIT5
XU10 149 145 140 129 UNIT5
XU11 150 146 141 145 UNIT5
XU12 151 147 142 146 UNIT5
XU13 152 148 143 147 UNIT5
XU14 153 120 144 148 UNIT5
XU15 154 150 145 149 UNIT5
XU16 155 151 146 150 UNIT5
XU17 156 152 147 151 UNIT5
XU18 157 153 148 152 UNIT5
XU19 158 154 149 128 UNIT5

XU20 159 155 150 154 UNIT5
XU21 160 156 151 155 UNIT5
XU22 161 157 152 156 UNIT5
XU23 162 121 153 157 UNIT5
XU24 163 159 154 158 UNIT5
XU25 164 160 155 159 UNIT5
XU26 165 161 156 160 UNIT5
XU27 166 162 157 161 UNIT5
XU28 167 164 159 163 UNIT5
XU29 168 165 160 164 UNIT5
XU30 169 166 161 165 UNIT5
XU31 125 168 164 167 UNIT5
XU32 124 169 165 168 UNIT5
XU34 134 101 132 UNIT6
XU35 134 101 117 UNIT6
XU52 153 105 120 UNIT6
XU54 153 105 121 UNIT6
XU71 168 109 125 UNIT6
XU72 168 109 124 UNIT6
XU51 149 113 129 UNIT6
XU53 149 113 128 UNIT6
XU42 139 118 103 UNIT1
XU44 139 119 103 UNIT1
XU64 166 123 107 UNIT1
XU62 166 122 107 UNIT1
XU61 163 127 111 UNIT1
XU63 163 126 111 UNIT1
XU43 136 130 115 UNIT1
XU41 136 131 115 UNIT1
XU46 144 119 139 UNIT2
XU40 135 118 139 UNIT2
XU60 162 122 166 UNIT2
XU66 169 123 166 UNIT2
XU59 158 127 163 UNIT2
XU65 167 126 163 UNIT2
XU45 140 130 136 UNIT2
XU39 133 131 136 UNIT2
XU48 144 104 119 UNIT3
XU38 135 102 118 UNIT3
XU58 162 106 122 UNIT3
XU68 169 108 123 UNIT3
XU67 167 110 126 UNIT3
XU57 158 112 127 UNIT3
XU47 140 114 130 UNIT3
XU37 133 116 131 UNIT3
XU36 117 102 135 UNIT4
XU50 120 104 144 UNIT4
XU56 121 106 162 UNIT4
XU70 124 108 169 UNIT4
XU69 125 110 167 UNIT4
XU55 128 112 158 UNIT4
XU49 129 114 140 UNIT4
XU33 132 116 133 UNIT4

* Connections between the upper plane(1) and the electrode plane

XUR1 1 101 HEIGHT
XUR2 2 102 HEIGHT
XUR3 3 103 HEIGHT
XUR4 4 104 HEIGHT
XUR5 5 105 HEIGHT
XUR6 6 106 HEIGHT

Appendix C: 6 Dimensional OF 10E Model

XUR7 7 107 HEIGHT
XUR8 8 108 HEIGHT
XUR9 9 109 HEIGHT
XUR10 10 110 HEIGHT
XUR11 11 111 HEIGHT
XUR12 12 112 HEIGHT
XUR13 13 113 HEIGHT
XUR14 14 114 HEIGHT
XUR15 15 115 HEIGHT
XUR16 16 116 HEIGHT
XUR17 17 117 HEIGHT
XUR18 18 118 HEIGHT
XUR19 19 119 HEIGHT
XUR20 20 120 HEIGHT
XUR21 21 121 HEIGHT
XUR22 22 122 HEIGHT
XUR23 23 123 HEIGHT
XUR24 24 124 HEIGHT
XUR25 25 125 HEIGHT
XUR26 26 126 HEIGHT
XUR27 27 127 HEIGHT
XUR28 28 128 HEIGHT
XUR29 29 129 HEIGHT
XUR30 30 130 HEIGHT
XUR31 31 131 HEIGHT
XUR32 32 132 HEIGHT
XUR33 33 133 HEIGHT
XUR34 34 134 HEIGHT
XUR35 35 135 HEIGHT
XUR36 36 136 HEIGHT
XUR37 37 137 HEIGHT
XUR38 38 138 HEIGHT
XUR39 39 139 HEIGHT
XUR40 40 140 HEIGHT
XUR41 41 141 HEIGHT
XUR42 42 142 HEIGHT
XUR43 43 143 HEIGHT
XUR44 44 144 HEIGHT
XUR45 45 145 HEIGHT
XUR46 46 146 HEIGHT
XUR47 47 147 HEIGHT
XUR48 48 148 HEIGHT
XUR49 49 149 HEIGHT
XUR50 50 150 HEIGHT
XUR51 51 151 HEIGHT
XUR52 52 152 HEIGHT
XUR53 53 153 HEIGHT
XUR54 54 154 HEIGHT
XUR55 55 155 HEIGHT
XUR56 56 156 HEIGHT
XUR57 57 157 HEIGHT
XUR58 58 158 HEIGHT
XUR59 59 159 HEIGHT
XUR60 60 160 HEIGHT
XUR61 61 161 HEIGHT
XUR62 62 162 HEIGHT
XUR63 63 163 HEIGHT
XUR64 64 164 HEIGHT
XUR65 65 165 HEIGHT
XUR66 66 166 HEIGHT
XUR67 67 167 HEIGHT

XUR68 68 168 HEIGHT
 XUR69 69 169 HEIGHT
 * Connections to the upper plane(2)
 XL1 237 234 232 233 UNIT5
 XL2 238 235 217 234 UNIT5
 XL3 241 237 233 236 UNIT5
 XL4 242 238 234 237 UNIT5
 XL5 243 239 235 238 UNIT5
 XL6 245 241 236 240 UNIT5
 XL7 246 242 237 241 UNIT5
 XL8 247 243 238 242 UNIT5
 XL9 248 244 239 243 UNIT5
 XL10 249 245 240 229 UNIT5
 XL11 250 246 241 245 UNIT5
 XL12 251 247 242 246 UNIT5
 XL13 252 248 243 247 UNIT5
 XL14 253 220 244 248 UNIT5
 XL15 254 250 245 249 UNIT5
 XL16 255 251 246 250 UNIT5
 XL17 256 252 247 251 UNIT5
 XL18 257 253 248 252 UNIT5
 XL19 258 254 249 228 UNIT5
 XL20 259 255 250 254 UNIT5
 XL21 260 256 251 255 UNIT5
 XL22 261 257 252 256 UNIT5
 XL23 262 221 253 257 UNIT5
 XL24 263 259 254 258 UNIT5
 XL25 264 260 255 259 UNIT5
 XL26 265 261 256 260 UNIT5
 XL27 266 262 257 261 UNIT5
 XL28 267 264 259 263 UNIT5
 XL29 268 265 260 264 UNIT5
 XL30 269 266 261 265 UNIT5
 XL31 225 268 264 267 UNIT5
 XL32 224 269 265 268 UNIT5
 XL34 234 201 232 UNIT6
 XL35 234 201 217 UNIT6
 XL52 253 205 220 UNIT6
 XL54 253 205 221 UNIT6
 XL71 268 209 225 UNIT6
 XL72 268 209 224 UNIT6
 XL51 249 213 229 UNIT6
 XL53 249 213 228 UNIT6
 XL42 239 218 203 UNIT1
 XL44 239 219 203 UNIT1
 XL64 266 223 207 UNIT1
 XL62 266 222 207 UNIT1
 XL61 263 227 211 UNIT1
 XL63 263 226 211 UNIT1
 XL43 236 230 215 UNIT1
 XL41 236 231 215 UNIT1
 XL46 244 219 239 UNIT2
 XL40 235 218 239 UNIT2
 XL60 262 222 266 UNIT2
 XL66 269 223 266 UNIT2
 XL59 258 227 263 UNIT2
 XL65 267 226 263 UNIT2
 XL45 240 230 236 UNIT2
 XL39 233 231 236 UNIT2
 XL48 244 204 219 UNIT3
 XL38 235 202 218 UNIT3

XL58 262 206 222 UNIT3
XL68 269 208 223 UNIT3
XL67 267 210 226 UNIT3
XL57 258 212 227 UNIT3
XL47 240 214 230 UNIT3
XL37 233 216 231 UNIT3
XL36 217 202 235 UNIT4
XL50 220 204 244 UNIT4
XL56 221 206 262 UNIT4
XL70 224 208 269 UNIT4
XL69 225 210 267 UNIT4
XL55 228 212 258 UNIT4
XL49 229 214 240 UNIT4
XL33 232 216 233 UNIT4

* Connection between upper layer(1) and upper layer(2)

XLR1 201 101 HEIGHT
XLR2 202 102 HEIGHT
XLR3 203 103 HEIGHT
XLR4 204 104 HEIGHT
XLR5 205 105 HEIGHT
XLR6 206 106 HEIGHT
XLR7 207 107 HEIGHT
XLR8 208 108 HEIGHT
XLR9 209 109 HEIGHT
XLR10 210 110 HEIGHT
XLR11 211 111 HEIGHT
XLR12 212 112 HEIGHT
XLR13 213 113 HEIGHT
XLR14 214 114 HEIGHT
XLR15 215 115 HEIGHT
XLR16 216 116 HEIGHT
XLR17 217 117 HEIGHT
XLR18 218 118 HEIGHT
XLR19 219 119 HEIGHT
XLR20 220 120 HEIGHT
XLR21 221 121 HEIGHT
XLR22 222 122 HEIGHT
XLR23 223 123 HEIGHT
XLR24 224 124 HEIGHT
XLR25 225 125 HEIGHT
XLR26 226 126 HEIGHT
XLR27 227 127 HEIGHT
XLR28 228 128 HEIGHT
XLR29 229 129 HEIGHT
XLR30 230 130 HEIGHT
XLR31 231 131 HEIGHT
XLR32 232 132 HEIGHT
XLR33 233 133 HEIGHT
XLR34 234 134 HEIGHT
XLR35 235 135 HEIGHT
XLR36 236 136 HEIGHT
XLR37 237 137 HEIGHT
XLR38 238 138 HEIGHT
XLR39 239 139 HEIGHT
XLR40 240 140 HEIGHT
XLR41 241 141 HEIGHT
XLR42 242 142 HEIGHT
XLR43 243 143 HEIGHT
XLR44 244 144 HEIGHT
XLR45 245 145 HEIGHT

XLR46 246 146 HEIGHT
 XLR47 247 147 HEIGHT
 XLR48 248 148 HEIGHT
 XLR49 249 149 HEIGHT
 XLR50 250 150 HEIGHT
 XLR51 251 151 HEIGHT
 XLR52 252 152 HEIGHT
 XLR53 253 153 HEIGHT
 XLR54 254 154 HEIGHT
 XLR55 255 155 HEIGHT
 XLR56 256 156 HEIGHT
 XLR57 257 157 HEIGHT
 XLR58 258 158 HEIGHT
 XLR59 259 159 HEIGHT
 XLR60 260 160 HEIGHT
 XLR61 261 161 HEIGHT
 XLR62 262 162 HEIGHT
 XLR63 263 163 HEIGHT
 XLR64 264 164 HEIGHT
 XLR65 265 165 HEIGHT
 XLR66 266 166 HEIGHT
 XLR67 267 167 HEIGHT
 XLR68 268 168 HEIGHT
 XLR69 269 169 HEIGHT

* The Constant Current Sources, each pulsed at a different time:

ICON1 1 9 PULSE(0 5M 0 0.0001M 0.0001M 1.5M 50M)
 ICON2 2 10 PULSE(0 5M 2M 0.0001M 0.0001M 1.5M 50M)
 ICON3 3 11 PULSE(0 5M 4M 0.0001M 0.0001M 1.5M 50M)
 ICON4 4 12 PULSE(0 5M 6M 0.0001M 0.0001M 1.5M 50M)
 ICON5 5 13 PULSE(0 5M 8M 0.0001M 0.0001M 1.5M 50M)
 ICON6 6 14 PULSE(0 5M 10M 0.0001M 0.0001M 1.5M 50M)
 ICON7 7 15 PULSE(0 5M 12M 0.0001M 0.0001M 1.5M 50M)
 ICON8 8 16 PULSE(0 5M 14M 0.0001M 0.0001M 1.5M 50M)
 ICON9 9 1 PULSE(0 5M 16M 0.0001M 0.0001M 1.5M 50M)
 ICON10 10 2 PULSE(0 5M 18M 0.0001M 0.0001M 1.5M 50M)
 ICON11 11 3 PULSE(0 5M 20M 0.0001M 0.0001M 1.5M 50M)
 ICON12 12 4 PULSE(0 5M 22M 0.0001M 0.0001M 1.5M 50M)
 ICON13 13 5 PULSE(0 5M 24M 0.0001M 0.0001M 1.5M 50M)
 ICON14 14 6 PULSE(0 5M 26M 0.0001M 0.0001M 1.5M 50M)
 ICON15 15 7 PULSE(0 5M 28M 0.0001M 0.0001M 1.5M 50M)
 ICON16 16 8 PULSE(0 5M 30M 0.0001M 0.0001M 1.5M 50M)

* SPICE control instructions

.tran 2M 33M 1M
 .print tran v(1,2) v(2,3) v(3,4) v(4,5) v(5,6)
 .print tran v(6,7) v(7,8) v(8,9) v(9,10) v(10,11)
 .print tran v(11,12) v(12,13) v(13,14) v(14,15) v(15,16)
 .print tran v(16,1)
 .END

APPENDIX 4

DUAL MODALITY TOMOGRAPHY SOFTWARE

A.4.1 MAIN PROGRAM FILE

```
// Windows/DOS headers:
#include <fcntl.h>
#include <io.h>
#include <dos.h>
#include <string.h>
#include <commdlg.h>
#include <conio.h>
#include <stdio.h>
#include <math.h>
#include <stdlib.h>
#include <windows.h>
// My headers, containing subroutines and definitions
#include <tomog_e.h>
#include <optrec_l.h>
#include <eitrec_e.h>
#include <eitinj_e.h>
#include <eitcap_e.h>
#include <fileio.h>

int PASCAL WinMain (HANDLE hInstance, HANDLE hPrevInstance,
                   LPSTR lpszCmdParam, int nCmdShow)
{
    char szAppName[] = "Tomography";
    HWND hwnd;
    MSG msg;
    WNDCLASS wndclass;
    lpszCmdParam+=0;

    if(!hPrevInstance)
    {
        wndclass.style =CS_HREDRAW | CS_VREDRAW;
        wndclass.lpfnWndProc =(WNDPROC)WndProc;
        wndclass.cbClsExtra =0;
        wndclass.cbWndExtra=0;
        wndclass.hInstance =hInstance;
        wndclass.hIcon =LoadIcon(hInstance, "icon1");
        wndclass.hCursor =LoadCursor(NULL, IDC_ARROW);
        wndclass.hbrBackground =GetStockObject(WHITE_BRUSH);
        wndclass.lpszMenuName ="Menu1";
        wndclass.lpszClassName =szAppName;
        RegisterClass (&wndclass);
    }

    hAccTable=LoadAccelerators(hInstance, "ACCELERATORS_1");
    hwnd=CreateWindow(szAppName, //window class name
                    "EIT Tomography Reconstruction", //window caption
                    WS_OVERLAPPEDWINDOW, //WINDOW STYLE
                    0, //INIT X POS
                    0, //INIT Y POS
                    GetSystemMetrics(SM_CXSCREEN), //INIT X SIZE
                    GetSystemMetrics(SM_CYSCREEN), //INIT Y SIZE
                    NULL, //PARENT WINDOW HANDLE
                    NULL, //WINDOW MENU HANDLE
```

```

hInstance,      //PROGRAM INSTANCE HANDLE
NULL);        //CREATION PARAMETERS
ShowWindow(hwnd, nCmdShow);
UpdateWindow(hwnd);

```

```

while (GetMessage(&msg, NULL, NULL, NULL))
{
    // Only translate message if it is not an accelerator message
    if (!TranslateAccelerator(hwnd, hAccTable, &msg))
    {
        TranslateMessage(&msg);
        DispatchMessage(&msg);
    }
}
return msg.wParam;
}

```

```

### This is a simple, basic ABOUT box routine ##
BOOL FAR PASCAL AboutDlgProc(HWND hwnd, WORD message, WORD wParam, LONG
IParam)
{

```

```

switch(message)
{
case WM_INITDIALOG:
    IParam+=0;
    return TRUE;

```

```

case WM_COMMAND:

```

```

switch(wParam)
{
case IDCANCEL:
case IDOK:
    EndDialog(hwnd, TRUE);
    return(TRUE);
}

```

```

break;

```

```

}
return(FALSE);
}

```

```

long FAR PASCAL WndProc(HWND hwnd, WORD message,WORD wParam, LONG IParam)
{

```

```

static HANDLE hInstance;
static FARPROC lpfnAboutDlgProc;
HDC hDC, hMemoryDC;
HBITMAP hOldBitmap;
BITMAP Bitmap;
PAINTSTRUCT ps;
int inc, cnt1, cnt2;

```

```

switch(message)
{

```

```

case WM_CREATE:
    lpfnAboutDlgProc=MakeProcInstance((FARPROC)AboutDlgProc, hInstance);
    hInstance=((LPCREATESTRUCT)IParam)->hInstance;
    bitmapX=800; ### This is used in printing the image ##
    bitmapY=600;

```

```

hDC=GetDC(hwnd);
hBitmap=CreateCompatibleBitmap(hDC, bitmapX, bitmapY);
hFont1=CreateFont(18,    /// Size of font ##
0,
0,
0,
FW_MEDIUM,
0,
0,
0,
ANSI_CHARSET,
OUT_DEFAULT_PRECIS,
CLIP_DEFAULT_PRECIS,
PROOF_QUALITY,
VARIABLE_PITCH,
"Times New Roman");
///## The brushes used to draw the coloured x-section ##
hPen0= CreatePen(PS_NULL,0, RGB(0,0,0));
hBrush0= CreateSolidBrush(RGB(250,250,250));
hBrush1= CreateSolidBrush(RGB(225,225,225));
hBrush2= CreateSolidBrush(RGB(200,200,200));
hBrush3= CreateSolidBrush(RGB(175,175,175));
hBrush4= CreateSolidBrush(RGB(150,150,150));
hBrush5= CreateSolidBrush(RGB(125,125,125));
hBrush6= CreateSolidBrush(RGB(100,100,100));
hBrush7= CreateSolidBrush(RGB( 75, 75, 75));
hBrush8= CreateSolidBrush(RGB( 50, 50, 50));
hBrush9= CreateSolidBrush(RGB( 25, 25, 25));
hBrush10=CreateSolidBrush(RGB( 0, 0, 0));
hWidePen=CreatePen(PS_SOLID, 17, RGB(0, 0, 0));
DeleteDC(hDC);
InitialiseIOPort(hwnd);
FillMats();
return 0;

case WM_SIZE:
cxClient=LOWORD(IParam);
cyClient=HIWORD(IParam);
InvalidateRect(hwnd, NULL, TRUE); ///## Repaint Workspace ##
return 0; ///## Update 2 parameters and repaint if size changes ##

///## Monitor the menu bar for any selections ##
case WM_COMMAND:
GetMenu(hwnd); ///## Has the menu provided the command ##
///## and if so what is it ##
switch(wParam)
{
case IDM_ABOUT: ///## The about dialog box ##
DialogBox(hInstance, "About2", hwnd, lpfnAboutDlgProc);
return 0;

case IDM_SETUP_HOMOG:
for(cnt1=0; cnt1<=15; cnt1++)
{
for(cnt2=0; cnt2<=15; cnt2++)
{
readings[cnt1][cnt2]=0;
}
}
}
// First injection position = 1 -> 9
// This is the 1'st set of readings

```

```

// It refers to inject1
SetupSwitches(hwnd, eElectrode1, eElectrode9);
ReadElectrodes(hwnd, 0);
SetupSwitches(hwnd, eElectrode2, eElectrode10);
ReadElectrodes(hwnd, 1);
SetupSwitches(hwnd, eElectrode3, eElectrode11);
ReadElectrodes(hwnd, 2);
SetupSwitches(hwnd, eElectrode4, eElectrode12);
ReadElectrodes(hwnd, 3);
SetupSwitches(hwnd, eElectrode5, eElectrode13);
ReadElectrodes(hwnd, 4);
SetupSwitches(hwnd, eElectrode6, eElectrode14);
ReadElectrodes(hwnd, 5);
SetupSwitches(hwnd, eElectrode7, eElectrode15);
ReadElectrodes(hwnd, 6);
SetupSwitches(hwnd, eElectrode8, eElectrode16);
ReadElectrodes(hwnd, 7);
// Only 1/2 the readings are required for 'opposite'

for(cnt1=0; cnt1<=15; cnt1++)
{
    for(cnt2=0; cnt2<=15; cnt2++)
    {
        homog[cnt1][cnt2]=readings[cnt1][cnt2]/ave;
    }
}

// Inform the user that its over
// via a message box
MessageBox(hwnd, "Homogenous Update Finished",
"Finished Update",
MB_OK | MB_ICONINFORMATION);
return 0;

case IDM_START_READINGS:
for(cnt1=0; cnt1<=15; cnt1++)
{
    for(cnt2=0; cnt2<=15; cnt2++)
    {
        readings[cnt1][cnt2]=0;
    }
}
SetupSwitches(hwnd, eElectrode1, eElectrode9);
ReadElectrodes(hwnd, 0);
SetupSwitches(hwnd, eElectrode2, eElectrode10);
ReadElectrodes(hwnd, 1);
SetupSwitches(hwnd, eElectrode3, eElectrode11);
ReadElectrodes(hwnd, 2);
SetupSwitches(hwnd, eElectrode4, eElectrode12);
ReadElectrodes(hwnd, 3);
SetupSwitches(hwnd, eElectrode5, eElectrode13);
ReadElectrodes(hwnd, 4);
SetupSwitches(hwnd, eElectrode6, eElectrode14);
ReadElectrodes(hwnd, 5);
SetupSwitches(hwnd, eElectrode7, eElectrode15);
ReadElectrodes(hwnd, 6);
SetupSwitches(hwnd, eElectrode8, eElectrode16);
ReadElectrodes(hwnd, 7);
// Only 1/2 the readings are required for 'opposite'

```

```

for(cnt1=0; cnt1<=15; cnt1++)
{
  for(cnt2=0; cnt2<=15; cnt2++)
  {
    readings[cnt1][cnt2]=readings[cnt1][cnt2]/ave;
  }
}

Difference();
Average();
InvalidateRect(hwnd, NULL, TRUE);
///  
Repaint Workspace ///  


// **** Now the OPTICAL Readings: ****
// First set up the port
for(cnt1=0; cnt1<=7; cnt1++)
{
  iowrite(BOTTOMDATA, bits[cnt1]); // D1 = 1
  // RESET=1... AND ABus = 000
  iowrite(GROUP3, 255-A0-A1-A2); // LED Set '0'
  iowrite(GROUP4, 255-BIT6); // CS low
  iowrite(GROUP4, 255); // CS back high
  iowrite(BOTTOMDATA, 255); // DBus = 1111 1111

  // Now read the port
  // CONTROL1 is either 0 or 1 to read each of
  // the two sets of sensors
  iowrite(CONTROL1, 255-BIT2-BIT3); // ABus
  iowrite(GROUP4, 255-BIT7); // Set BIT7 (CS) = 0
  wait(1);
  ReadSensors(cnt1); // Take readings
  iowrite(CONTROL1, 255);
  iowrite(GROUP4, 255);
  iowrite(GROUP3, 255-BIT6); // reset (RS=0) LED's
  iowrite(GROUP3, 255); // Back to 255
}

// Now for port2
// CONTROL1 is either 0 or 1 to read each of
// the two sets of sensors
for(cnt1=0; cnt1<=7; cnt1++)
{
  iowrite(BOTTOMDATA, bits2[cnt1]); // D1 = 1
  // RESET=1... AND ABus = 000
  iowrite(GROUP3, 255-A1-A2); // LED Set '0'
  iowrite(GROUP4, 255-BIT6); // CS low
  iowrite(GROUP4, 255); // CS back high
  iowrite(BOTTOMDATA, 255); // DBus = 1111 1111

  // Now read the port
  // CONTROL1 is either 0 or 1 to read each of
  // the two sets of sensors
  iowrite(CONTROL1, 255-BIT1-BIT2-BIT3); // ABus
  iowrite(GROUP4, 255-BIT7); // Set BIT7 (CS) = 0
  wait(1);
  ReadSensors(cnt1+8); // Take readings
  iowrite(CONTROL1, 255);
  iowrite(GROUP4, 255);
  iowrite(GROUP3, 255-BIT6); // reset (RS=0) LED's
  iowrite(GROUP3, 255); // Back to 255
}

```

```

iowrite(BOTTOMDATA, 255); // Dbus = 1111 1111
InvalidateRect(hwnd, NULL, TRUE);

// Now set the correct Variables
for(cnt2=0; cnt2<=7; cnt2++)
{
    optreadings[0][cnt2]=OPTDATA[cnt2][cnt2];
    optreadings[1][cnt2]=OPTDATA[cnt2+8][cnt2];
}

OptDifference();
OptAverage();
InvalidateRect(hwnd, NULL, TRUE);
///  
Repaint Workspace ///  
return 0;

case IDM_SAVE_IMAGE: ///  
Copy presently displayed image to Clipboard ///  
CMUFileSaveImg(hwnd);
break;

case IDM_SAVE_DUAL_DATA: ///  
Copy presently displayed image to Clipboard ///  
CMUFileSaveDualDat(hwnd);
break;

case IDM_SAVE_EIT_DATA: ///  
Copy presently displayed image to Clipboard ///  
CMUFileSaveEitDat(hwnd);
break;

case IDM_SAVE_OPTICAL_DATA: ///  
Copy presently displayed image to Clipboard ///  
CMUFileSaveOptDat(hwnd);
break;
case IDM_COPY_IMAGE: ///  
Copy presently displayed image to Clipboard ///  
hGMem=GlobalAlloc(GHND, (DWORD)sizeof(METAFILEPICT));
lpMFP=(LPMETAFILEPICT)GlobalLock(hGMem); ///  
Allocate memory and set ///  
lpMFP->mm = MM_ISOTROPIC;          ///  
size constants etc.. ///  
lpMFP->xExt=600;
lpMFP->yExt=450;
lpMFP->hMF=hmf;
GlobalUnlock(hGMem);
OpenClipboard(hwnd); ///  
Open and clear Clipboard ///  
EmptyClipboard();
SetClipboardData(CF_METAFILEPICT, hGMem);
CloseClipboard();    ///  
Save memory to Clipboard ///  
return 0;

case IDM_EXIT: // User wants to exit
DestroyWindow(hwnd);
break;

}
return 0;

case WM_PAINT: ///  
Now we paint the screen in response to an ///  
combine();    ///  
invalidaterect command ///  
hDC=BeginPaint(hwnd, &ps);
SetMapMode(hDC, MM_ISOTROPIC);
SetWindowExt(hDC, 750, 475);
SetViewportExt(hDC, 600, 400); ///  
Set size of screen viewport ///  
SetWindowOrg(hDC, -20, -35); ///  
Set the Play Position, middle= 0,0 ///  
PlayMetaFile(hDC, hmf);    ///  
Play the Metafile on screen ///  
EndPaint(hwnd, &ps);    ///  
This removes the DC and rounds things off ///  


```

```

return 0;

case WM_DESTROY:  /// When finished delete all new handles ##
DeleteObject(hFont1);
DeleteObject(hPen0);
DeleteObject(hBrush0);
DeleteObject(hBrush1);
DeleteObject(hBrush2);
DeleteObject(hBrush3);
DeleteObject(hBrush4);
DeleteObject(hBrush5);
DeleteObject(hBrush6);
DeleteObject(hBrush7);
DeleteObject(hBrush8);
DeleteObject(hBrush9);
DeleteObject(hBrush10);
DeleteObject(hWidePen);
MessageBeep(MB_ICONHAND);
PostQuitMessage(0);
return (0);
}
return DefWindowProc(hwnd, message, wParam, lParam);
}

// This routine takes the individual 'Metafile' routines for both
// Optical and EIT and combines them to produce a dual modality image.
// This 'Control' routine can be refined or completely rewritten in
// order to provide a more scientific method of data combination.
// It uses 'equip' and 'optequip', storing the final values in equip
// for the time being:
void combine(void)
{
int cnt1, cnt2;
for(cnt1=0; cnt1<=31; cnt1++)
{
for(cnt2=0; cnt2<=31; cnt2++)
{
equip[cnt1][cnt2]=(equip[cnt1][cnt2]+optequip[cnt1][cnt2])/2;
}
}
}
SetUpMeta();
}

// These are the paint instructions that set up the Metafiles hmf1 and hmf2
// They are only updated when the readings are updated and therefore switching
// between images on screen doesn't waste processor time
void SetUpMeta(void)
{
HDC hDCMeta;
int cnt1, cnt2, x, y;
char buffer[40];
float var1, var2;
int d1, d2, d3, d4, d5;
hDCMeta=CreateMetaFile(NULL); /// Can only have one Metafile open at once ##
x=15;
y=15;
hOldPen=SelectObject(hDCMeta, hPen0);
hOldBrush=SelectObject(hDCMeta, hBrush0); /// Select our own pen/brush ##
SelectObject(hDCMeta, hFont1);

```

```

for(cnt1=0; cnt1<=31; cnt1++)
{
  for(cnt2=0; cnt2<=31; cnt2++)
  {
    if(equip[cnt1][cnt2]==0)  ///# Equip = 0 means leave blanc (white) ##
      goto nodraw;
    if(equip[cnt1][cnt2]==1)  ///# Equip = 1 means paint that square with brush0 ##
    {
      SelectObject(hDCMeta, hPen0);
      SelectObject(hDCMeta, hBrush1);
    }
    if(equip[cnt1][cnt2]==2)  ///# etc..... ##
    {
      SelectObject(hDCMeta, hPen0);
      SelectObject(hDCMeta, hBrush2);
    }
    if(equip[cnt1][cnt2]==3)  ///# N.B. hDCMeta = handle to present Metafiles Displaycontext
    ##
    {
      SelectObject(hDCMeta, hPen0);
      SelectObject(hDCMeta, hBrush3);
    }
    if(equip[cnt1][cnt2]==4)
    {
      SelectObject(hDCMeta, hPen0);
      SelectObject(hDCMeta, hBrush4);
    }
    if(equip[cnt1][cnt2]==5)
    {
      SelectObject(hDCMeta, hPen0);
      SelectObject(hDCMeta, hBrush5);
    }
    if(equip[cnt1][cnt2]==6)
    {
      SelectObject(hDCMeta, hPen0);
      SelectObject(hDCMeta, hBrush6);
    }
    if(equip[cnt1][cnt2]==7)
    {
      SelectObject(hDCMeta, hPen0);
      SelectObject(hDCMeta, hBrush7);
    }
    if(equip[cnt1][cnt2]==8)
    {
      SelectObject(hDCMeta, hPen0);
      SelectObject(hDCMeta, hBrush8);
    }
    if(equip[cnt1][cnt2]==9)
    {
      SelectObject(hDCMeta, hPen0);
      SelectObject(hDCMeta, hBrush9);
    }
    if(equip[cnt1][cnt2]==10)
    {
      SelectObject(hDCMeta, hPen0);
      SelectObject(hDCMeta, hBrush10);
    }

    SetBkMode(hDCMeta, OPAQUE);
    Rectangle(hDCMeta, x, y, x+15, y+15);
    nodraw:   x+=13;
  }
}

```

```

    }
    y+=13;
    x=15;
    }

SelectObject(hDCMeta, hWidePen);
SelectObject(hDCMeta, GetStockObject(HOLLOW_BRUSH));
Ellipse(hDCMeta, 15, 15, 431, 431);///  
 Draw circular boundary ##
SetBkMode(hDCMeta, OPAQUE);
TextOut(hDCMeta, 480, 70, "INJECTION: OPPOSITE", 19);
TextOut(hDCMeta, 480, 100, "MODALITY: EIT", 13);
x=0;    ///  
 Add text ##
y=0;
SelectObject(hDCMeta, hOldPen);
SelectObject(hDCMeta, hOldBrush); ///  
 Restore old pen/brush to DC ##
hmf=CloseMetaFile(hDCMeta); ///  
 hmf1 now points to the details/info for this Metafile ##
}

///  
 Merely sets Finalnet to ZERO ##
void ClearReadings(void)
{
int cnt1,cnt2;
for(cnt1=0; cnt1 <=31; cnt1++)
    {
    for(cnt2=0; cnt2 <=31; cnt2++)
        {
        finalnet[cnt1][cnt2]=0.00;
        }
    }
}

///  
 This converts 'float' numbers to 'int' numbers ##
///  
 as long as there values are less than 10, which they are ##
///  
 in the routine that calls this ##
int mag(float val)
{
int cnt1, ret;

for(cnt1=0; cnt1<=9; cnt1++)
    {
    if(cnt1 <= val)
        ret=cnt1;
    }
return(ret);
}

///  
 This routine sets up the I/O port ##
int InitialiseIOPort(HWND hwnd)
{
if (ioread(IDREG) == 0) /* Check I/O boards' ID code */
    iowrite(OPENABLE,0xFF); ///  
 Enable buffers - VERY IMPORTANT ##
else
    {
    MessageBox(hwnd, "No PCIB40 Port Found", NULL, MB_OK | MB_ICONEXCLAMATION);
    return(FALSE);
    }
}

///  
 Now set all the ZERO control bits to their correct values ##
iowrite(CONTROL1, 0);
iowrite(GROUP4, NOT_CS1+NOT_CS2);
iowrite(TOPDATA_CONTROL2, 0);

```

```

iowrite(BOTTOMDATA, 0); /// Set everything to zero ##
iowrite(GROUP3, 255-BIT6); // Reset the logic chips at setup
/// Now set all the Readable BITS to '1' to enable them for reading ##
iowrite(BOTTOMDATA, 255); /// Enable reading of D0 - D7 ##
iowrite(TOPDATA_CONTROL2, D8 + D9 + D10 + D11 + MODE + NOT_BUSY_EIT);
/// Rest of data bus plus MODE=HIGH (i/o port mode)
iowrite(CONTROL1, NOT_WR + NOT_RD); /// Unipolar ##
/// Other control bits that must start in a high state ##
return(TRUE);
}

```

```

#####
##### This resets all the LED's #####
#####
void Resetleds(HWND hwnd)
{
iowrite(GROUP3, 0); /// GROUP3 includes the DG526 reset bit ##
InvalidateRect(hwnd, NULL, TRUE);
return; /// Easy or what !!! ##
}

#####
void ReadSensors(int where) /// The HWND is for MessageBox calls ##
{
int inc, oldval, newval;

// Find state of CONTROL1
oldval=ioread(CONTROL1);
// Set NOT_WR low
newval=oldval-NOT_WR;
// Keeping N_CS(OPT2) LOW take N_CS(MAX) LOW also
iowrite(GROUP4, 255-N_CS_OPT2-N_CS_MAX);
// Send new value of CONTROL1 to port
iowrite(CONTROL1, newval);
// Now, keeping N_CS(OPT2) LOW send N_CS(MAX) back HIGH
iowrite(GROUP4, 255-N_CS_OPT2);
// Send NOT_WR back HIGH as well
iowrite(CONTROL1, oldval);
// Conversion is now instigated therefore loop round until
// BUSY goes back high
loop: oldval=ioread(GROUP4);
if(oldval==255-NOT_BUSY_OPT-N_CS_OPT2)
goto loop;

for(inc=0; inc<=7; inc++)
{
// Find state of CONTROL1
oldval=ioread(CONTROL1);
// Set NOT_RD low
newval=oldval-NOT_RD;
iowrite(CONTROL1, newval);
// Keeping N_CS(OPT2) LOW take N_CS(MAX) LOW also
iowrite(GROUP4, 255-N_CS_OPT2-N_CS_MAX);
// Read bottom 8 bits
OPTDATA[where][inc]=ioread(BOTTOMDATA);
// Restore RD, CS bit to HIGH
iowrite(CONTROL1, oldval);
// Now, keeping N_CS(OPT2) LOW send N_CS(MAX) back HIGH
iowrite(GROUP4, 255-N_CS_OPT2);
}
}

```

```
return;
}
```

A.4.2 HEADER FILE: TOMOG_E.H

```
### Define Bit Values ##
#define BIT1 1      ### Bit/s 1----- ##
#define BIT2 2      ### Bit/s -1----- ##
#define BIT3 4      ### Bit/s --1---- ##
#define BIT4 8      ### Bit/s ---1--- ##
#define BIT5 16     ### Bit/s ----1-- ##
#define BIT6 32     ### Bit/s -----1- ##
#define BIT7 64     ### Bit/s -----1- ##
#define BIT8 128    ### Bit/s -----1 ##
#define ALLPLUS 255 ### Bit/s 11111111 ##
### STE addresses ##
#define OFFSET 0x180    ### Address of PCIB40 offset register ##
#define DATA OFFSET + 1  ### " " " " data registers ##
#define BOTTOMDATA 0x00  ### GROUP0 offset ##
#define TOPDATA_CONTROL2 0x01  ### GROUP1 offset ##
#define CONTROL1 0x02    ### GROUP2 offset ##
#define GROUP3 0x03     ### " " " ##
#define GROUP4 0x04     ### GROUP4 offset ##
#define TOP4 BIT5+BIT6+BIT7+BIT8
### Multiplexed I/O addresses ##
#define TIMER0 0x10    ### Timer0 in timer IC ##
#define CWREG 0x13    ### Timer command word reg ##
#define INJECT 0x03    ### Group 3 offset ##
#define OPENABLE 0x90  ### O/P buffer enable register, standard address. ##
#define USRLED 0x80    ### User LED standard address ##
#define IDREG 0x81    ### Board type identification code address ##
### Define Bits of Port 0: all used for Analogue Mult' ##
#define AM0 1      ### Bit/s 1----- ##
#define AM1 2      ### Bit/s -1----- ##
#define AM2 4      ### Bit/s --1---- ##
#define AM3 8      ### Bit/s ---1--- ##
#define Write1 16   ### Bit/s ----1-- ##
#define Reset 32    ### Bit/s -----1- ##
#define Enable 64   ### Bit/s -----1- ##
#define Write2 128  ### Bit/s -----1 ##
#define ReadReady 255 ### Bit/s 11111111 ##
#define A2 BIT3
#define A1 BIT2
#define A0 BIT1
#define D0 BIT1
#define D1 BIT2
#define D2 BIT3
#define D3 BIT4
#define D4 BIT5
#define D5 BIT6
#define D6 BIT7
#define D7 BIT8    ### All port 0 #
#define D8 BIT1
#define D9 BIT2
#define D10 BIT3
#define D11 BIT4

### The 8-bit words to identify the electrode position ##
### for the analogue switches ##
#define eElectrode1 0
```



```

// Optical Constants:
int optreadings[2][8];
int OPTDATA[16][8];
float optfinalnet[32][32];
int optfinalnet1[32][32];
int optequip[32][32]={0};
int oppzero[16][16]= {{1,1,0,0,0,0,0,0,1,1,0,0,0,0,0,0},
                      {0,1,1,0,0,0,0,0,0,1,1,0,0,0,0,0},
                      {0,0,1,1,0,0,0,0,0,0,1,1,0,0,0,0},
                      {0,0,0,1,1,0,0,0,0,0,0,1,1,0,0,0},
                      {0,0,0,0,1,1,0,0,0,0,0,0,1,1,0,0},
                      {0,0,0,0,0,1,1,0,0,0,0,0,0,1,1,0},
                      {0,0,0,0,0,0,1,1,0,0,0,0,0,0,1,1},
                      {0,0,0,0,0,0,1,1,0,0,0,0,0,0,1,1},
                      {1,0,0,0,0,0,0,1,1,0,0,0,0,0,0,1},
                      {1,1,0,0,0,0,0,0,1,1,0,0,0,0,0,0},
                      {0,1,1,0,0,0,0,0,0,1,1,0,0,0,0,0},
                      {0,0,1,1,0,0,0,0,0,0,1,1,0,0,0,0},
                      {0,0,0,1,1,0,0,0,0,0,0,1,1,0,0,0},
                      {0,0,0,0,1,1,0,0,0,0,0,0,1,1,0,0},
                      {0,0,0,0,0,1,1,0,0,0,0,0,0,1,1,0},
                      {0,0,0,0,0,0,1,1,0,0,0,0,0,0,1,1},
                      {1,0,0,0,0,0,0,1,1,0,0,0,0,0,0,1}};

int bits2[8]={BIT8, BIT7, BIT6, BIT5, BIT4, BIT3, BIT2, BIT1};
int bits[8]={BIT1, BIT2, BIT3, BIT4, BIT5, BIT6, BIT7, BIT8};

// General Constants:
int hX, hY;
int bitmapX, bitmapY, cxClient, cyClient;
char *blanc="xDB";
HBITMAP hBitmap;
HPEN hPen0, hWidePen, hOldPen;
HBRUSH hBrush0, hBrush1, hBrush2, hOldBrush;
HBRUSH hBrush3, hBrush4, hBrush5, hBrush6, hBrush7;
HBRUSH hBrush8, hBrush9, hBrush10;
static HANDLE hmf = NULL;
GLOBALHANDLE hGMem;
LPMETAFILEPICT lpMFP;
HANDLE hPr, hAccTable;
HFONT hFont1, hFont2;

// EIT Subroutines:
void FillMats(void);
void Rotate16_2(void);
void FirstClock(int eit1[32][32], int eit2[32][32]);
void Difference(void);
void Average(void);
int ReadElectrodes(HWND, int);
void CalcFinalNet(int array[32][32], int);
int InitialiseIOPort(HWND);      /// Check the I/O port and set it up ##
void SetupSwitches(HWND, int, int);  /// Set the groups up with their values ##
void ResetElectrodes(void);        /// Reset the electrodes to o/c ##
void ClearReadings(void);
void SetUpMeta(void);

// Optical Subroutines:
void OptDifference(void);
void OptAverage(void);
void OptCalcFinalNet(int array[32][32], int);
void ReadSensors(int);

```

```
void FAR SetupInjection(HWND, int, int);
void ResetLeds(HWND);
```

```
// File Save Subroutines:
```

```
void CMUFileSaveImg(HWND);
void CMUFileSaveDualData(HWND);
void CMUFileSaveEitData(HWND);
void CMUFileSaveOptData(HWND);
```

```
// General Subroutines:
```

```
long FAR PASCAL WndProc(HWND, WORD,WORD, LONG);
int mag(float);
void wait(int);      /// Rather complicated delay procedure ##
void iowrite( int, int ); /// I/O Port write procedure ##
int ioread( int );   /// I/O Port read procedure ##
void combine(void);
```

A.4.3 HEADER FILE: OPTREC_L.H

```
// Optrec.h: The code for Optical Reconstruction of Data
///# This routine calculates the difference between the ##
///# hardware readings stored in thw global variable readings[][] ##
///# and the homogenous values stored in homog[][] ##
void OptDifference(void)
{
  int indx1, indx2;
  for(indx1=0; indx1<=1; indx1++)
  {
    for(indx2=0; indx2<=7; indx2++)
    {
      optreadings[indx1][indx2]=255-optreadings[indx1][indx2];
    }
  }
  for(indx1=0; indx1<=31; indx1++)
  {
    for(indx2=0; indx2<=31; indx2++)
    {
      optfinalnet[indx1][indx2]=0;
    }
  }
  OptCalcFinalNet(light1, 0);
  for(indx1=0; indx1<=31; indx1++)
  {
    for(indx2=0; indx2<=31; indx2++)
    {
      optfinalnet1[indx1][indx2]=optfinalnet[indx1][indx2];
    }
  }
  OptCalcFinalNet(light2, 1);
  for(indx1=0; indx1<=31; indx1++)
  {
    for(indx2=0; indx2<=31; indx2++)
    {
      optfinalnet[indx1][indx2]*=optfinalnet1[indx1][indx2];
    }
  }
}

///# This routine calculates the value of the final array ##
///# finalnet[][] before the color array associated with these ##
///# values is calculated ##
```

```

void OptCalcFinalNet(int array[32][32], int row)
{
int indx1, indx2;
for(indx1=0; indx1<=31; indx1++)
{
for(indx2=0; indx2<=31; indx2++)
{
// if it's == 1 then this means it wants readings for
// electrode2 - electrode1. These are stored in row 0-15,
// but in column 1 - NOT 0!!!
if(array[indx1][indx2]==1)
{
optfinalnet[indx1][indx2]=optreadings[row][0];
goto finish;
}
if(array[indx1][indx2]==2)
{
optfinalnet[indx1][indx2]=optreadings[row][1];
goto finish;
}
if(array[indx1][indx2]==3)
{
optfinalnet[indx1][indx2]=optreadings[row][2];
goto finish;
}
if(array[indx1][indx2]==4)
{
optfinalnet[indx1][indx2]=optreadings[row][3];
goto finish;
}
if(array[indx1][indx2]==5)
{
optfinalnet[indx1][indx2]=optreadings[row][4];
goto finish;
}
if(array[indx1][indx2]==6)
{
optfinalnet[indx1][indx2]=optreadings[row][5];
goto finish;
}
if(array[indx1][indx2]==7)
{
optfinalnet[indx1][indx2]=optreadings[row][6];
goto finish;
}
if(array[indx1][indx2]==8)
{
optfinalnet[indx1][indx2]=optreadings[row][7];
goto finish;
}
finish: ;
}
}
}

```

```

### This routine calculates the average values of those in ##
### finalnet[][] with respect to the maximum value therein ##
void OptAverage(void)
{
int indx1, indx2;
for(indx1=0; indx1<=31; indx1++)

```

```
{
for(indx2=0; indx2<=31; indx2++)
{
// Max Value for 2 Projections = 2*255=510:
optfinalnet[indx1][indx2]=((optfinalnet[indx1][indx2]
/65025)*100);
if(optfinalnet[indx1][indx2]==0)
{
optequip[indx1][indx2]=0;
goto finish;
}
if(optfinalnet[indx1][indx2]>=90)
{
optequip[indx1][indx2]=10;//## 1 = Most significant, darkest ##
goto finish;
}
if((optfinalnet[indx1][indx2]<=90)&
(optfinalnet[indx1][indx2]>=80))
{
optequip[indx1][indx2]=9;
goto finish;
}
if((optfinalnet[indx1][indx2]<=80)&
(optfinalnet[indx1][indx2]>=70))
{
optequip[indx1][indx2]=8;
goto finish;
}
if((optfinalnet[indx1][indx2]<=70)&
(optfinalnet[indx1][indx2]>=60))
{
optequip[indx1][indx2]=7;
goto finish;
}
if((optfinalnet[indx1][indx2]<=60)&
(optfinalnet[indx1][indx2]>=50))
{
optequip[indx1][indx2]=6;
goto finish;
}
if((optfinalnet[indx1][indx2]<=50)&
(optfinalnet[indx1][indx2]>=40))
{
optequip[indx1][indx2]=5;
goto finish;
}
if((optfinalnet[indx1][indx2]<=40)&
(optfinalnet[indx1][indx2]>=30))
{
optequip[indx1][indx2]=4;
goto finish;
}
if((optfinalnet[indx1][indx2]<=30)&
(optfinalnet[indx1][indx2]>=20))
{
optequip[indx1][indx2]=3;
goto finish;
}
if((optfinalnet[indx1][indx2]<=20)&
(optfinalnet[indx1][indx2]>=10))
{

```

```

    optequip[indx1][indx2]=2;
    goto finish;
  }
  if((optfinalnet[indx1][indx2]<=10)&
    (optfinalnet[indx1][indx2]>=9))
  {
    optequip[indx1][indx2]=1;
    goto finish;
  }
  optequip[indx1][indx2]=0;
  finish: ;
}
}
}

```

A.4.4 HEADER FILE: EITREC_E.H

```

### This rotates eit1 by 90 degrees to produce eit2 ##
void FirstClock(int eit1[32][32], int eit2[32][32])
{
  float buff;
  int slowplus, fastplus, slowminus;
### Rotate by 90 degrees an renumber to maintain there##
### correct positions in the colour scheme ##
  for(slowplus=0; slowplus<=31; slowplus++)
  {
    for(fastplus=0; fastplus<=31; fastplus++)
    {
      slowminus=31-slowplus;
      eit2[fastplus][slowminus]=eit1[slowplus][fastplus];
      if(eit2[fastplus][slowminus]==0)
        buff=0;
      if(eit2[fastplus][slowminus]>4)
        buff=eit2[fastplus][slowminus]-4;
      if((eit2[fastplus][slowminus]<=4)&(eit2[fastplus][slowminus]>0))
        buff=eit2[fastplus][slowminus]+12;
      eit2[fastplus][slowminus]=buff;
    }
  }
}

### This creates the other 13 matrices using FirstClock ##
### by rotating the three defined matrices through 90 ##
### degrees, and the using the result to produce the next ##
### etc.. It also uses another routine to produce inject2 ##
### before it can be rotated as it doesn't exist and can ##
### easilly be formed from inject16 by flipping through ##
### 180 degrees. ##
void FillMats(void)
{
  int indx1, indx2;

  FirstClock(inject1, inject5);
  FirstClock(inject5, inject9);
  FirstClock(inject9, inject13);
  FirstClock(inject16, inject4);
  FirstClock(inject4, inject8);
  FirstClock(inject8, inject12);
  FirstClock(inject15, inject3);
  FirstClock(inject3, inject7);
  FirstClock(inject7, inject11);
}

```

```
Rotate16_20); /// Produce Inject2 from inject16 ##  
FirstClock(inject2, inject6);  
FirstClock(inject6, inject10);  
FirstClock(inject10, inject14);  
}
```

```
void Rotate16_2(void)  
{  
int indx1, indx2, val;  
for(indx1=0; indx1<=31; indx1++)  
{  
for(indx2=0; indx2<=31; indx2++)  
{  
val=31-indx2;  
inject2[indx1][val]=inject16[indx1][indx2];  
if(inject2[indx1][val]==1)  
{  
inject2[indx1][val]=16;  
goto finish;  
}  
if(inject2[indx1][val]==2)  
{  
inject2[indx1][val]=15;  
goto finish;  
}  
if(inject2[indx1][val]==3)  
{  
inject2[indx1][val]=14;  
goto finish;  
}  
if(inject2[indx1][val]==4)  
{  
inject2[indx1][val]=13;  
goto finish;  
}  
if(inject2[indx1][val]==5)  
{  
inject2[indx1][val]=12;  
goto finish;  
}  
if(inject2[indx1][val]==6)  
{  
inject2[indx1][val]=11;  
goto finish;  
}  
if(inject2[indx1][val]==7)  
{  
inject2[indx1][val]=10;  
goto finish;  
}  
if(inject2[indx1][val]==8)  
{  
inject2[indx1][val]=9;  
goto finish;  
}  
if(inject2[indx1][val]==9)  
{  
inject2[indx1][val]=8;  
goto finish;  
}  
if(inject2[indx1][val]==10)
```

```

    {
        inject2[indx1][val]=7;
        goto finish;
    }
    if(inject2[indx1][val]==11)
    {
        inject2[indx1][val]=6;
        goto finish;
    }
    if(inject2[indx1][val]==12)
    {
        inject2[indx1][val]=5;
        goto finish;
    }
    if(inject2[indx1][val]==13)
    {
        inject2[indx1][val]=4;
        goto finish;
    }
    if(inject2[indx1][val]==14)
    {
        inject2[indx1][val]=3;
        goto finish;
    }
    if(inject2[indx1][val]==15)
    {
        inject2[indx1][val]=2;
        goto finish;
    }
    if(inject2[indx1][val]==16)
    {
        inject2[indx1][val]=1;
        goto finish;
    }
    finish: ;
}
}
}

```

```

### This routine calculates the difference between the ##
### hardware readings stored in thw global variable readings[][] ##
### and the homogenous values stored in homog[][] ##
void Difference(void)
{
    int indx1, indx2;
    for(indx1=0; indx1<=15; indx1++)
    {
        for(indx2=0; indx2<=15; indx2++)
        {
            if((readings[indx1][indx2]!=0)&&(homog[indx1][indx2]!=0))
            {
                readings[indx1][indx2]=(readings[indx1][indx2]-homog[indx1][indx2]);//
                (readings[indx1][indx2]+homog[indx1][indx2]);
            }
            else
            {
                readings[indx1][indx2]=0;
            }
        }
    }
}
for(indx1=0; indx1<=31; indx1++)

```

```

{
  for(indx2=0; indx2<=31; indx2++)
  {
    finalnet[indx1][indx2]=0;
  }
}
CalcFinalNet(inject1, 0);
CalcFinalNet(inject2, 1);
CalcFinalNet(inject3, 2);
CalcFinalNet(inject4, 3);
CalcFinalNet(inject5, 4);
CalcFinalNet(inject6, 5);
CalcFinalNet(inject7, 6);
CalcFinalNet(inject8, 7);
CalcFinalNet(inject9, 8);
CalcFinalNet(inject10, 9);
CalcFinalNet(inject11, 10);
CalcFinalNet(inject12, 11);
CalcFinalNet(inject13, 12);
CalcFinalNet(inject14, 13);
CalcFinalNet(inject15, 14);
CalcFinalNet(inject16, 15);
}

```

```

### This routine calculates the value of the final array ##
### finalnet[][] before the color array associated with these ##
### values is calculated ##
void CalcFinalNet(int array[32][32],int row)
{
  int indx1, indx2;
  for(indx1=0; indx1<=31; indx1++)
  {
    for(indx2=0; indx2<=31; indx2++)
    {
      // if it's == 1 then this means it wants readings for
      // electrode2 - electrode1. These are stored in row 0-15,
      // but in colum 1 - NOT 0!!!
      if(array[indx1][indx2]==1)
      {
        finalnet[indx1][indx2]=finalnet[indx1][indx2]+readings[row][1];
        goto finish;
      }
      if(array[indx1][indx2]==2)
      {
        finalnet[indx1][indx2]=finalnet[indx1][indx2]+readings[row][2];
        goto finish;
      }
      if(array[indx1][indx2]==3)
      {
        finalnet[indx1][indx2]=finalnet[indx1][indx2]+readings[row][3];
        goto finish;
      }
      if(array[indx1][indx2]==4)
      {
        finalnet[indx1][indx2]=finalnet[indx1][indx2]+readings[row][4];
        goto finish;
      }
      if(array[indx1][indx2]==5)
      {
        finalnet[indx1][indx2]=finalnet[indx1][indx2]+readings[row][5];
        goto finish;
      }
    }
  }
}

```

```

    }
    if(array[indx1][indx2]==6)
    {
        finalnet[indx1][indx2]=finalnet[indx1][indx2]+readings[row][6];
        goto finish;
    }
    if(array[indx1][indx2]==7)
    {
        finalnet[indx1][indx2]=finalnet[indx1][indx2]+readings[row][7];
        goto finish;
    }
    if(array[indx1][indx2]==8)
    {
        finalnet[indx1][indx2]=finalnet[indx1][indx2]+readings[row][8];
        goto finish;
    }
    if(array[indx1][indx2]==9)
    {
        finalnet[indx1][indx2]=finalnet[indx1][indx2]+readings[row][9];
        goto finish;
    }
    if(array[indx1][indx2]==10)
    {
        finalnet[indx1][indx2]=finalnet[indx1][indx2]+readings[row][10];
        goto finish;
    }
    if(array[indx1][indx2]==11)
    {
        finalnet[indx1][indx2]=finalnet[indx1][indx2]+readings[row][11];
        goto finish;
    }
    if(array[indx1][indx2]==12)
    {
        finalnet[indx1][indx2]=finalnet[indx1][indx2]+readings[row][12];
        goto finish;
    }
    if(array[indx1][indx2]==13)
    {
        finalnet[indx1][indx2]=finalnet[indx1][indx2]+readings[row][13];
        goto finish;
    }
    if(array[indx1][indx2]==14)
    {
        finalnet[indx1][indx2]=finalnet[indx1][indx2]+readings[row][14];
        goto finish;
    }
    if(array[indx1][indx2]==15)
    {
        finalnet[indx1][indx2]=finalnet[indx1][indx2]+readings[row][15];
        goto finish;
    }
    if(array[indx1][indx2]==16)
    {
        finalnet[indx1][indx2]=finalnet[indx1][indx2]+readings[row][0];
    }
    finish: ;
}
}
}

```

This routine calculates the average values of those in

```

### finalnet[][] with respect to the maximum value therein ##
void Average(void)
{
int indx1, indx2;
float bufferh, bufferl;
bufferl=0.0;
bufferh=0.0;
for(indx1=0; indx1<=31; indx1++)
{
for(indx2=0; indx2<=31; indx2++)
{
if(finalnet[indx1][indx2]>=bufferh)
{
bufferh=finalnet[indx1][indx2];
}
if(finalnet[indx1][indx2]<=bufferl)
{
bufferl=finalnet[indx1][indx2];
}
}
}
}
if(bufferl<=0) // Find value of largest magnitude
bufferl=bufferl*-1; // If bufferl=-ve then make +ve
if(bufferl>=bufferh)
bufferh=bufferl; // Only keep largest value for '%' calculations
for(indx1=0; indx1<=31; indx1++)
{
for(indx2=0; indx2<=31; indx2++)
{
finalnet[indx1][indx2]=((finalnet[indx1][indx2]/bufferh)*100);
if(finalnet[indx1][indx2]==0)
{
equip[indx1][indx2]=0;
goto finish;
}
if((finalnet[indx1][indx2]<=100)&
(finalnet[indx1][indx2]>=90))
{
equip[indx1][indx2]=10; /// 1 = Most significant, darkest ##
goto finish;
}
if((finalnet[indx1][indx2]<=90)&
(finalnet[indx1][indx2]>=80))
{
equip[indx1][indx2]=9;
goto finish;
}
if((finalnet[indx1][indx2]<=80)&
(finalnet[indx1][indx2]>=70))
{
equip[indx1][indx2]=8;
goto finish;
}
if((finalnet[indx1][indx2]<=70)&
(finalnet[indx1][indx2]>=60))
{
equip[indx1][indx2]=7;
goto finish;
}
if((finalnet[indx1][indx2]<=60)&
(finalnet[indx1][indx2]>=50))
{

```

```

    equip[indx1][indx2]=6;
    goto finish;
  }
  if((finalnet[indx1][indx2]<=50)&
    (finalnet[indx1][indx2]>=40))
  {
    equip[indx1][indx2]=5;
    goto finish;
  }
  if((finalnet[indx1][indx2]<=40)&
    (finalnet[indx1][indx2]>=30))
  {
    equip[indx1][indx2]=4;
    goto finish;
  }
  if((finalnet[indx1][indx2]<=30)&
    (finalnet[indx1][indx2]>=20))
  {
    equip[indx1][indx2]=3;
    goto finish;
  }
  if((finalnet[indx1][indx2]<=20)&
    (finalnet[indx1][indx2]>=10))
  {
    equip[indx1][indx2]=2;
    goto finish;
  }
  if((finalnet[indx1][indx2]<=10)&
    (finalnet[indx1][indx2]>=0))
  {
    equip[indx1][indx2]=1;
    goto finish;
  }
  equip[indx1][indx2]=0;
  finish: ;
}
}
}

```

A.4.5 HEADER FILE: EITINJ_E.H

```

### This Sets up both the '+' and '-' Electrodes and ##
### then pulses (NOT)Write HIGH ##
void SetupSwitches(HWND hwnd, int eElectrodeP, int eElectrodeN)
{
  if(eElectrodeP == eElectrodeN)
  {
    MessageBox(hwnd, "This Would Connect '+' to '-', Cancel??.", NULL, MB_OK |
      MB_ICONEXCLAMATION);
    return;
  }
  // Note: INJECT == GROUP3;
  iowrite(INJECT, eElectrodeP + Enable + Reset);
  iowrite(INJECT, eElectrodeP + Enable + Reset + Write1);
  iowrite(INJECT, eElectrodeP + Reset + Write1);
  iowrite(INJECT, eElectrodeN + Enable + Reset + Write1); ### Keep Write1 HIGH ##
  iowrite(INJECT, eElectrodeN + Enable + Reset + Write1 + Write2);
  iowrite(INJECT, eElectrodeN + Reset + Write1 + Write2);
  iowrite(GROUP3, 255-BIT6); // Reset the logic chips as a precaution
  wait(12);
}

```

```

#####
##### This resets all the electrodes to open cct #####
#####
void ResetElectrodes(void)
{
iowrite(INJECT, 0);
return;
}

```

```

#####
### This is a wait procedure that came with the io port ##
#####
void wait(int period) /* A rather over-complicated delay routine that*/
/* demonstrates the timer of the PCIB40.*/
{
int ctr = 0xFF;
iowrite(CWREG,0x26); /* Timer 0, mode 3, decimal, load MSB only */
iowrite(TIMER0,0); /* MSB of count, counter starts */
while(period--)
{
/* 2 x 'WHILE' loops wait for counter MSB transition 0-$FF */
while(ctr != 0) /* Wait for counter = 0 */
{
iowrite(CWREG,0x00); /* Latch count */
ctr = ioread(TIMER0);
}
while(ctr != 10) /* Wait for counter = 10 */
{
iowrite(CWREG,0x00); /* Latch count */
ctr = ioread(TIMER0);
}
}
}
}

```

```

#####
##### This converts the single line command into the ####
##### format required by the C compiler #####
#####
void iowrite( int ioaddr, int value)
{
outportb(OFFSET,ioaddr); /* Set up I/O address */
outportb((DATA),value); /* Write value to I/O address */
}

```

```

#####
##### This converts the single line command into the ####
##### format required by the C compiler #####
#####
int ioread( int ioaddr )
{
outportb(OFFSET,ioaddr); /* Set up I/O address */
return (inportb(DATA)); /* Read back value */
}

```

A.4.6 HEADER FILE: EITCAP_E.H

```

int ReadElectrodes(HWND hwnd, int where)
{
int inc, oldval, newval, incaverage;
hwnd+=0;

```

```

for(incaverage=1; incaverage<=ave; incaverage++)
{
  for(inc=0; inc<=7; inc++)
  {
    /// First job = set up Control logic, ie which input ? ##
    oldval=ioread(CONTROL1);/// Find state of CONTROL1 ##
    newval=oldval-NOT_WR+inc; /// Set WRITE bit low and choose an ##
    /// analogue input ##
    iowrite(GROUP4, 0+NOT_CS1);
    iowrite(CONTROL1, newval);    /// Send new value to port ##
    iowrite(CONTROL1, newval+NOT_WR); /// Now set write high.. ##
    iowrite(CONTROL1, oldval); /// ..and then restore most of old value ##
    loop: oldval=ioread(TOPDATA_CONTROL2);
    if(oldval<128)
      goto loop; /// Loop until BUSY goes HIGH ##
    oldval=ioread(CONTROL1);/// Find state of CONTROL1 ##
    newval=oldval-NOT_RD;    /// Set READ bit low ##
    iowrite(CONTROL1, newval);    /// Send new value to port ##
    /// Read top 4 bits ##
    readings[where][inc]+=ioread(BOTTOMDATA);    /// Read bottom 8 bits ##
    readings[where][inc]+=(ioread(TOPDATA_CONTROL2)-MODE-NOT_BUSY_EIT)*255;
    iowrite(CONTROL1, oldval); /// Restore RD, CS bit to HIGH ##
    iowrite(GROUP4, NOT_CS1+NOT_CS2);
  }
  for(inc=0; inc<=7; inc++)
  {
    /// First job = set up Control logic, ie which input ? ##
    oldval=ioread(CONTROL1);/// Find state of CONTROL1 ##
    newval=oldval-NOT_WR+inc; /// Set WRITE bit low and choose an ##
    /// analogue input ##
    iowrite(GROUP4, 0+NOT_CS2);
    iowrite(CONTROL1, newval);    /// Send new value to port ##
    iowrite(CONTROL1, newval+NOT_WR); /// Now set write high.. ##
    iowrite(CONTROL1, oldval); /// ..and then restore most of old value ##
    loop2: oldval=ioread(TOPDATA_CONTROL2);
    if(oldval<128)
      goto loop2; /// Loop until BUSY goes HIGH ##
    oldval=ioread(CONTROL1);/// Find state of CONTROL1 ##
    newval=oldval-NOT_RD;    /// Set READ bit low ##
    iowrite(CONTROL1, newval);    /// Send new value to port ##
    /// Read top 4 bits ##
    readings[where][inc+8]+=ioread(BOTTOMDATA);    /// Read bottom 8 bits ##
    readings[where][inc+8]+=(ioread(TOPDATA_CONTROL2)-MODE-NOT_BUSY_EIT)*255;
    iowrite(CONTROL1, oldval); /// Restore RD, CS bit to HIGH ##
    iowrite(GROUP4, NOT_CS1+NOT_CS2);
  }    /// And then do until all 8 ports are read ##
}
}
for(inc=0; inc<=15; inc++)
{
  if(oppzero[where][inc]==1)
  {
    readings[where][inc]=0;
  }
}
return(TRUE);
}

```

A.4.7 HEADER FILE: EIT_E.H

```

/** Global Variables */
char szName[256];

```

```

### Save the image to disk ##
void CMUFileSaveImg( HWND hWnd )
{
    OPENFILENAME ofnTemp;
    DWORD Errval; // Error value
    char buf[5]; // Error buffer
    char Errstr[50]="GetOpenFileName returned Error #";
    char szTemp[] = "Image Files (*.img)\0*.img\0All Files (*.*)\0*.*\0";
    FILE *stream;
    int cnt1,cnt2;
    ofnTemp.lStructSize = sizeof( OPENFILENAME );
    ofnTemp.hwndOwner = hWnd; // An invalid hWnd causes non-modality
    ofnTemp.hInstance = 0;
    ofnTemp.lpstrFilter = (LPSTR)szTemp; // See previous note concerning string
    ofnTemp.lpstrCustomFilter = NULL;
    ofnTemp.nMaxCustFilter = 0;
    ofnTemp.nFilterIndex = 1;
    ofnTemp.lpstrFile = (LPSTR)szName; // Stores the result in this variable
    ofnTemp.nMaxFile = sizeof( szName );
    ofnTemp.lpstrFileTitle = NULL;
    ofnTemp.nMaxFileTitle = 0;
    ofnTemp.lpstrInitialDir = NULL;
    ofnTemp.lpstrTitle = "Save Dual Modality Image..."; // Title for dialog
    ofnTemp.Flags = OFN_FILEMUSTEXIST | OFN_HIDEREADONLY | OFN_PATHMUSTEXIST;
    ofnTemp.nFileOffset = 0;
    ofnTemp.nFileExtension = 0;
    ofnTemp.lpstrDefExt = "";
    ofnTemp.lCustData = NULL;
    ofnTemp.lpfHook = NULL;
    ofnTemp.lpTemplateName = NULL;
}
/*
If the call to GetOpenFileName() fails you can call CommDlgExtendedError()
to retrieve the type of error that occurred.
*/
if(GetSaveFileName( &ofnTemp ) != TRUE)
{
    Errval=CommDlgExtendedError();
    if(Errval!=0) // 0 value means user selected Cancel
    {
        sprintf(buf,"%ld",Errval);
        strcat(Errstr,buf);
        MessageBox(hWnd,Errstr,"WARNING",MB_OK|MB_ICONSTOP);
    }
}
if ((stream = fopen(ofnTemp.lpstrFile, "wt")) == NULL) /* open file TEST.$$$ */
{
    //fprintf(stderr, "Cannot open output file.\n");
    MessageBeep(MB_ICONASTERISK);
    return;
}
fprintf(stream, "Dual Modality Image Data:\n\n");
for(cnt1=0; cnt1<=31; cnt1++)
{
    for(cnt2=0; cnt2<=31; cnt2++)
    {
        fprintf(stream, "%d\t", equip[cnt1][cnt2]); /* write struct s to file */
    }
    fprintf(stream, "\n");
}
fclose(stream); /* close file */

```

```

return;
}

### Save dual modality data ###
void CMUFileSaveDualDat( HWND hWnd )
{
OPENFILENAME ofnTemp;
DWORD Errval; // Error value
char buf[5]; // Error buffer
char Errstr[50]="GetOpenFileName returned Error #";
char szTemp[] = "Dual' Data Files (*.dal)\0*.dal\0All Files (*.*)\0*.*\0";
FILE *stream;
int cnt1,cnt2;
ofnTemp.lStructSize = sizeof( OPENFILENAME );
ofnTemp.hwndOwner = hWnd; // An invalid hWnd causes non-modality
ofnTemp.hInstance = 0;
ofnTemp.lpstrFilter = (LPSTR)szTemp; // See previous note concerning string
ofnTemp.lpstrCustomFilter = NULL;
ofnTemp.nMaxCustFilter = 0;
ofnTemp.nFilterIndex = 1;
ofnTemp.lpstrFile = (LPSTR)szName; // Stores the result in this variable
ofnTemp.nMaxFile = sizeof( szName );
ofnTemp.lpstrFileTitle = NULL;
ofnTemp.nMaxFileTitle = 0;
ofnTemp.lpstrInitialDir = NULL;
ofnTemp.lpstrTitle = "Save Dual Modality Data..."; // Title for dialog
ofnTemp.Flags = OFN_FILEMUSTEXIST | OFN_HIDEREADONLY | OFN_PATHMUSTEXIST;
ofnTemp.nFileOffset = 0;
ofnTemp.nFileExtension = 0;
ofnTemp.lpstrDefExt = "";
ofnTemp.lCustData = NULL;
ofnTemp.lpfHook = NULL;
ofnTemp.lpTemplateName = NULL;
/*
If the call to GetOpenFileName() fails you can call CommDlgExtendedError()
to retrieve the type of error that occurred.
*/
if(GetSaveFileName( &ofnTemp ) != TRUE)
{
Errval=CommDlgExtendedError();
if(Errval!=0) // 0 value means user selected Cancel
printf(buf,"%ld",Errval);
strcat(Errstr,buf);
MessageBox(hWnd,Errstr,"WARNING",MB_OK|MB_ICONSTOP);
}
}
if ((stream = fopen(ofnTemp.lpstrFile, "wt")) == NULL) /* open file TEST.$$$ */
{
fprintf(stderr, "Cannot open output file.\n");
return;
}
fprintf(stream, "EIT Readings:\n\n");
for(cnt1=0; cnt1<=15; cnt1++)
{
for(cnt2=0; cnt2<=15; cnt2++)
{
fprintf(stream, "%5.2f\t", readings[cnt1][cnt2]); /* write struct s to file */
}
fprintf(stream, "\n");
}
fprintf(stream, "\n\n");

```

```

fprintf(stream, "Optical Readings:\n\n");
for(cnt1=0; cnt1<=1; cnt1++)
{
    for(cnt2=0; cnt2<=7; cnt2++)
    {
        fprintf(stream, "%d\t", optreadings[cnt1][cnt2]); /* write struct s to file */
    }
    fprintf(stream, "\n");
}
fclose(stream); /* close file */
return;
}

### Save EIT data to disk ###
void CMUFileSaveEitDat( HWND hWnd )
{
    OPENFILENAME ofnTemp;
    DWORD Errval; // Error value
    char buf[5]; // Error buffer
    char Errstr[50]="GetOpenFileName returned Error #";
    char szTemp[] = "EIT Data Files (*.dae)\0*.dae\0All Files (*.*)\0*.*\0";
    FILE *stream;
    int cnt1,cnt2;
    ofnTemp.lStructSize = sizeof( OPENFILENAME );
    ofnTemp.hwndOwner = hWnd; // An invalid hWnd causes non-modality
    ofnTemp.hInstance = 0;
    ofnTemp.lpstrFilter = (LPSTR)szTemp; // See previous note concerning string
    ofnTemp.lpstrCustomFilter = NULL;
    ofnTemp.nMaxCustFilter = 0;
    ofnTemp.nFilterIndex = 1;
    ofnTemp.lpstrFile = (LPSTR)szName; // Stores the result in this variable
    ofnTemp.nMaxFile = sizeof( szName );
    ofnTemp.lpstrFileTitle = NULL;
    ofnTemp.nMaxFileTitle = 0;
    ofnTemp.lpstrInitialDir = NULL;
    ofnTemp.lpstrTitle = "Save EIT Data..."; // Title for dialog
    ofnTemp.Flags = OFN_FILEMUSTEXIST | OFN_HIDEREADONLY | OFN_PATHMUSTEXIST;
    ofnTemp.nFileOffset = 0;
    ofnTemp.nFileExtension = 0;
    ofnTemp.lpstrDefExt = "";
    ofnTemp.lCustData = NULL;
    ofnTemp.lpfnHook = NULL;
    ofnTemp.lpTemplateName = NULL;
    /*
    If the call to GetOpenFileName() fails you can call CommDlgExtendedError()
    to retrieve the type of error that occurred.
    */
    if(GetSaveFileName( &ofnTemp ) != TRUE)
    {
        Errval=CommDlgExtendedError();
        if(Errval!=0) // 0 value means user selected Cancel
        {
            sprintf(buf,"%ld",Errval);
            strcat(Errstr,buf);
            MessageBox(hWnd,Errstr,"WARNING",MB_OK|MB_ICONSTOP);
        }
    }
    if ((stream = fopen(ofnTemp.lpstrFile, "wt")) == NULL) /* open file TEST.$$$ */
    {
        fprintf(stderr, "Cannot open output file.\n");
        return;
    }
}

```

```

    }
    fprintf(stream, "EIT Readings:\n\n");
    for(cnt1=0; cnt1<=15; cnt1++)
    {
        for(cnt2=0; cnt2<=15; cnt2++)
        {
            fprintf(stream, "%5.2ft", readings[cnt1][cnt2]); /* write struct s to file */
        }
        fprintf(stream, "\n");
    }
    fclose(stream); /* close file */
    return;
}
### Save optical data to disk ###
void CMUFileSaveOptDat( HWND hWnd )
{
    OPENFILENAME ofnTemp;
    DWORD Errval; // Error value
    char buf[5]; // Error buffer
    char Errstr[50]="GetOpenFileName returned Error #";
    char szTemp[] = "Optical Data Files (*.dao)\0*\0All Files (*.*)\0*\0";
    FILE *stream;
    int cnt1,cnt2;
    ofnTemp.lStructSize = sizeof( OPENFILENAME );
    ofnTemp.hwndOwner = hWnd; // An invalid hWnd causes non-modality
    ofnTemp.hInstance = 0;
    ofnTemp.lpstrFilter = (LPSTR)szTemp; // See previous note concerning string
    ofnTemp.lpstrCustomFilter = NULL;
    ofnTemp.nMaxCustFilter = 0;
    ofnTemp.nFilterIndex = 1;
    ofnTemp.lpstrFile = (LPSTR)szName; // Stores the result in this variable
    ofnTemp.nMaxFile = sizeof( szName );
    ofnTemp.lpstrFileTitle = NULL;
    ofnTemp.nMaxFileTitle = 0;
    ofnTemp.lpstrInitialDir = NULL;
    ofnTemp.lpstrTitle = "Save Optical Data As..."; // Title for dialog
    ofnTemp.Flags = OFN_FILEMUSTEXIST | OFN_HIDEREADONLY | OFN_PATHMUSTEXIST;
    ofnTemp.nFileOffset = 0;
    ofnTemp.nFileExtension = 0;
    ofnTemp.lpstrDefExt = "";
    ofnTemp.lCustData = NULL;
    ofnTemp.lpfnHook = NULL;
    ofnTemp.lpTemplateName = NULL;
    /*
    If the call to GetOpenFileName() fails you can call CommDlgExtendedError()
    to retrieve the type of error that occurred.
    */
    if(GetSaveFileName( &ofnTemp ) != TRUE)
    {
        Errval=CommDlgExtendedError();
        if(Errval!=0) // 0 value means user selected Cancel
        {
            sprintf(buf,"%ld",Errval);
            strcat(Errstr,buf);
            MessageBox(hWnd,Errstr,"WARNING",MB_OK|MB_ICONSTOP);
        }
    }
    if ((stream = fopen(ofnTemp.lpstrFile, "wt")) == NULL) /* open file TEST.$$$ */
    {
        fprintf(stderr, "Cannot open output file.\n");
        return;
    }

```

```
    }  
    fprintf(stream, "Optical Readings:\n\n");  
    for(cnt1=0; cnt1<=1; cnt1++)  
    {  
        for(cnt2=0; cnt2<=7; cnt2++)  
        {  
            fprintf(stream, "%d\t", optreadings[cnt1][cnt2]); /* write struct s to file */  
        }  
        fprintf(stream, "\n");  
    }  
    fclose(stream); /* close file */  
  
    return; }  
}
```

APPENDIX 5

PUBLICATIONS

Publications, to date, resulting from this work are:

1. Daniels A R, Basarab-Horwath I, Dickin F and Green R G, "A proposed measurement system using dual modality tomography."
ECAPT 92: First Meeting of BRITE-EURAM Concerted Action on Process Tomography, 26-29 March, 1992, Manchester.
2. Daniels A R, Basarab-Horwath I, Dickin F and Green R G, "Initial Findings on an EIT Imaging System for Sewers."
ECAPT 93: Second Meeting of BRITE-EURAM Concerted Action on Process Tomography, Karlesruhe, 25-27 March, 1993.
3. Daniels A R, Green R G and Basarab-Horwath I, "Modelling of three dimensional resistive discontinuities using 'HSPICE'",
IOP, Measurement Science and Technology, March 1996.
4. Daniels A R, Green R G and Basarab-Horwath I, "Dual-Modality Image Reconstruction from 'Optical' and 'Electric Resistance' Data", Currently Under Consideration by the journal 'Electronic Letters'